TECHNISCHE UNIVERSITÄT DRESDEN

Fakultät Mathematik und Naturwissenschaften

LEIBNITZ INSTITUT FÜR FESTKÖRPER- UND WERKSTOFFFORSCHUNG

Interplay of Strong Correlation, Spin-Orbit Coupling and Electron-Phonon Interactions in Quasi-2D Iridium Oxides

Ekaterina Pärschke

Born on: 22.07.1990 in Moscow

Dissertation

First referee

Prof. Dr. Jeroen van den Brink

Second referee

Dr. Krzysztof Wohlfeld

Submitted on: 04.10.2017

Erklärung

Die vorliegende Dissertation wurde am Institut für Theoretische Physik der Technischen Universität Dresden unter Leitung von Prof. Dr. Jeroen van den Brink angefertigt.
Hiermit versichere ich, dass ich die vorliegende Arbeit ohne unzulässige Hilfe Dritter und ohne Benutzung anderer als der angegebenen Hilfsmittel angefertigt habe; die aus fremden Quellen direkt oder indirekt übernommenen Gedanken sind als solche kenntlich gemacht.Die Arbeit wurde bisher weder im Inland noch im Ausland in gleicher oder ähnlicher Form einer anderen Prüfungsbehörde vorgelegt.

Bis zum jetzigen Zeitpunkt habe ich keinerlei erfolglose Promotionsverfahren absolviert.

Ich erkenne hiermit die Promotionsordnung der Fakultät Mathematik und Naturwissenschaften der Technischen Universität Dresden vom 23.02.2011 an.

Ekaterina Pärschke

Contents

CHAPTER 1

Introduction

1.1. Preface

In the last decade a large number of studies have been devoted to the peculiarities of correlated physics found in the quasi-two-dimensional square lattice iridium oxides, such as Sr_2IrO_4 or Ba_2IrO_4 [46, 54, 118]. It was shown that this $5d$ family of transition metal oxides (TMO) has strong structural and electronic similarities to the famous $3d$ family of copper oxides, the quasi-two-dimensional square-lattice undoped copper oxides as exemplified by La_2CuO_4 or $Sr_2CuO_2Cl_2$ [24, 54, 59]. The $5d$ ions such as Ir have three active d-orbitals, that lie in t_{2g} manifold and make relevant models to describe physics in the system in general orbital-dependent and rather complicated. Although electron-electron Coulomb repulsion U is much smaller in $5d$ TMO than in $3d$ TMO, it was shown by B. J. Kim *et al.* in 2008 [54] that due to strong on-site spin-orbit coupling (SOC) the effective width of the conductance band can get significantly reduced and a Mott gap can open upon even moderate U, and insulating behavior can be observed. Then in 2009 G. Jackeli and G. Khaliullin [46] proposed that upon strong on-site spin-orbit coupling the superexchange model projected onto the proper basis of total J_{eff} momenta transforms into a simple Heisenberg model. It turned out that just as for the cuprates, the ground state of these square-lattice iridates is a 2D antiferromagnet and a Mott insulator [16, 54, 59, 117] – albeit formed by the $j = 1/2$ spin-orbital (SO) isospins instead of the $s = 1/2$ spins [46, 54, 59]. This observation has stimulated a lot of research on these iridates.

Naturally, such a delicate interplay of on-site spin-orbit coupling, Coulomb repulsion and crystalline electric field interactions is expected to drive various exotic quantum states. Many theoretical proposals were made in the last decade including the prediction of possible superconductivity in square-lattice iridates emerging as a sister system to high-T_c cuprates [54, 58–61, 76, 111, 116, 124, 125, 127]. The combination of electron-electron interaction and spin-orbit coupling was also discovered as a promising route to alternative topologically nontrivial states, from topological Mott [88, 118] over fractional Chern [8] insulators to a potential realization [19, 46] of the Kitaev's celebrated spin-liquid phase with its anyonic excitations [7, 62]. Honeycomb iridates were predicted to be topological band insulators [100], hyper-kagome iridates were predicted to host a spin-liquid state [66, 67, 84, 130].

Whereas a number of predicted phenomena were soon discovered in iridates indeed [15], many of the theoretical predictions have met very limited experimental confirmation. For instance, despite many experimental indications of possible superconductivity in doped Sr_2IrO_4 – including observation of Fermi arcs and a d-wave gap in electron-doped Sr_2IrO_4 [60, 61, 112] - there is still no superconductivity with zero electrical resistance and/or Meissner effect revealed in these systems. Interestingly, another compound with a similar structure, Sr_2RuO_4, was indeed reported to be superconducting at temperature lower than $T_c = 0.93$ K [71]. Moreover, a plethora of puzzling features were observed in iridates experimentally, such as the emergence of an odd-parity hidden order in Rh-doped Sr_2IrO_4 [47, 129] and the absence of conventional correlations between magnetic and insulating states [35, 41, 131] including the nonappearance of any anomaly in the resistivity corresponding to the Néel temperature and the avoidance of metalization at high pressures [29, 41, 63, 68, 131]. To name one, why does Sr_2IrO_4 remain insulating in high pressures up to 48 GPa [41, 131] whereas long-range magnetic order is already gone at 20 GPa [41, 131]?

Considering all these features, one can raise a general question: To what extend is the low-energy physics of the quasi-two-dimensional square-lattice iridium oxides different from other TMO with the same K_2NiF_4 type crystal structure such as La_2CuO_4 or Sr_2RuO_4?

In this thesis we investigate some of the effects which are usually neglected in studies on iridates, focusing on quasi-two-dimensional square-lattice iridates such as Sr_2IrO_4 or Ba_2IrO_4. In particular, we discuss the role of the electron-phonon coupling in the form of Jahn-Teller interaction in chapter 2, electron-hole asymmetry introduced by the strong correlations in chapters 3 – 4 and some effects of coupling scheme chosen to calculate multiplet structure for

materials with strong on-site spin-orbit coupling in chapter 5.

1.2. Structure of this thesis

In chapter 1, we briefly introduce the concepts that are vital to understand present challenges in the field of Iridates. In section 1.3, we introduce a single-band Hubbard model and its relation to the t-J model and superexchange model as well as discuss shortly the metal-insulator transition. In section 1.4, we consider multiorbital Hubbard and superexchange models and introduce the compound we focus on in this manuscript – Sr_2IrO_4. In section 1.5, we are going to discuss in detail how the two-dimensional antiferromagnetic (AF) Mott insulator is stabilized as the ground state of Sr_2IrO_4 due to strong on-site spin-orbit coupling. In the last part of the introduction, section 1.6, we talk about the polaronic approach and self-consistent Born approximation (SCBA) that we are going to use throughout the whole thesis.

In chapter 2, we study the role of phonons, which is almost always neglected in Sr_2IrO_4, and discuss the manifestation of Jahn-Teller effect in the recent data obtained on Sr_2IrO_4 with the help of resonant inelastic x-ray scattering. When strong spin-orbit coupling removes orbital degeneracy, it would at the same time appear to render the Jahn-Teller mechanism ineffective. We discuss such a situation, the t_{2g} manifold of iridates, and show that, while the Jahn-Teller effect does indeed not affect the $j_{\text{eff}} = 1/2$ antiferromagnetically ordered ground state, it leads to distinctive signatures in the $j_{\text{eff}} = 3/2$ spin-orbit exciton. It allows for a hopping of the spin-orbit exciton between the nearest neighbor sites without producing defects in the $j_{\text{eff}} = 1/2$ antiferromagnet. This arises because the lattice-driven Jahn-Teller mechanism only couples to the orbital degree of freedom, but is not sensitive to the phase of the wave function that defines the isospin j_z. This contrasts sharply with purely electronic propagation, which conserves isospin, and the presence of Jahn-Teller coupling can explain some of the peculiar features of measured resonant inelastic x-ray scattering spectra of Sr_2IrO_4.

In chapter 3, we determine the motion of a charge (hole or electron) added to the Mott insulating, antiferromagnetic ground-state of square-lattice iridates such as Ba_2IrO_4 or Sr_2IrO_4. We show that correlation effects, calculated within the self-consistent Born approximation, render the hole and electron case very different. An added electron forms a spin-polaron, which closely resembles the well-known cuprates, but the situation of a removed electron is far more complex. Many-body $5d^4$ configurations form that can be either singlets and triplets of total angular momentum J, which strongly affects the hole motion between AF sublattices. This not only has important ramifications for the interpretation of angle-resolved photoemission spectroscopy (ARPES) and inverse photoemission spectroscopy (IPES) experiments of square-lattice iridates, but also demonstrates that the correlation physics in electron- and hole-doped iridates is fundamentally different.

In chapter 4 we discuss the application of the model developed in chapter 3 to the calculation of STS spectra. We show that using STS one can directly probe the quasiparticle excitations in Sr_2IrO_4: ladder spectrum on the positive bias side and multiplet structure of the polaron on the negative bias side. We discuss in detail the ladder spectrum and show its relevance for Sr_2IrO_4 which is in general described by more complicated extended t-J-like model. Theoretical calculation reveals that on the negative bias side the internal degree of freedom of the charge excitation introduces strong dispersive hopping channels encaving ladder-like features which is in a perfect agreement with STS experimental data.

Finally, in chapter 5, we discuss how the choice of the coupling scheme to calculate multiplet structure can affect the theoretical calculation of ARPES and scanning tunneling spectroscopy (STS) spectral functions. There are two distinct coupling schemes that can be used to calculate the singlet and triplet states formed by the $5d^4$ configuration in the case of strong on-site spin-orbit coupling. One of them assumes spin-orbit coupling to be larger than

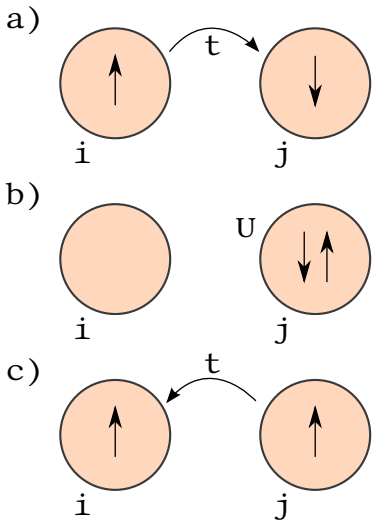

Figure 1.1.: Example of a virtual hopping process creating a virtual charge excitation (double occupancy) in a Mott insulator with half filling: (a) initial, (b) intermediate and (c) final states on two sites.

Hund's coupling and is addressed as *jj* coupling scheme, the other one approaches spin-orbit coupling as a perturbation to the Hund's coupling and is called *LS* coupling scheme. We discuss the applicability of each of the two schemes and show how one or the other of them shall be introduced analytically. We find certain (although not dramatic) effects of using either coupling scheme on the spectral functions for a particular case of Sr_2IrO_4.

1.3. Single-band superexchange model

Written in the early 1960's, the Hubbard model has proven itself to be a relatively simple though effective way to get insight into strongly correlated materials. Despite its simplicity, it is able to capture many of subtle and beautiful effects arising from electrons' interactions including insulating, magnetic, and even novel superconducting behavior. The (single-band fermionic) Hubbard model is given by

$$\mathcal{H}_{\text{Hubbard}} = -\sum_{i,j\neq i,\sigma} t_{ij\sigma} a^{\dagger}_{i\sigma} a_{j\sigma} + U \sum_{i} n_{i\uparrow} n_{i\downarrow} \,, \tag{1.1}$$

where $a^{\dagger}_{i\sigma}$ denotes an operator creating an electron on site i carrying spin $s = 1/2$ with projection $s_z = \sigma$ and $n_{i\sigma} = a^{\dagger}_{i\sigma} a_{i\sigma}$ is the on-site number of particles operator, t_{ij} is a hopping element that can in principle be direction-dependent and U called "Hubbard U" is the energy cost of double occupancy on a single site.

One of the fundamental features of the Hubbard model is that as the value of U increases, the electronic eigenfunctions closer to the atomic representation of electronic states rather than the non-interacting Bloch states. This fact expresses the so-called Mott-Hubbard or metal-insulator transition. In the strong coupling limit, i.e. when $U \gg t$, one can treat the hopping part of Hamiltonian 1.1 as a perturbation and in the second order of the perturbation theory arrive at the t-J model, first derived by J. Spałek *et al.* [20, 104]:

$$\mathcal{H}_{t\text{-}J} = -\sum_{\langle i,j\rangle,\sigma} \left(t_{ij\sigma} \left(1 - n_{i-\sigma}\right) c^{\dagger}_{i\sigma} c_{j\sigma} \left(1 - n_{j-\sigma}\right) + \text{h.c.} \right) + J \sum_{\langle i,j\rangle} \left(\mathbf{S}_i \cdot \mathbf{S}_j - \frac{n_i n_j}{4} \right). \tag{1.2}$$

In the limiting case of a Mott-Hubbard insulator at half-filling, i.e. when the number of particles per cite is conserved and is equal to one (for single-band case), the t-J model (1.2) reduces to well-known antiferromagnetic Heisenberg model (also sometimes referred to as Anderson superexchange Hamiltonian [103]):

$$\mathcal{H}_{\mathrm{AFM}} = J \sum_{\langle i,j \rangle} \mathbf{S}_i \cdot \mathbf{S}_j \,. \tag{1.3}$$

Here the exchange integral $J = \frac{4t^2}{U}$ is positive (nearest neighbor hopping integrals $t_{ij\sigma} = t_{i'j'\sigma'} = t$ are all equal in the simplest case of a single orbital, no magnetic field or any other induced translation symmetry breaking).

Let me briefly discuss the derivation of the superexchange model (1.3) from Hubbard model (1.1) at half-filling by integrating out the double occupancies in the second order of the perturbation theory in the strong U coupling limit. In Fig. 1.1 one of the virtual hopping processes taken into account in the second order of the perturbation theory is shown. One can see, that if the hopping process has amplitude t and an intermediate state costs energy U, compared to the initial state, then for the half filling the effective Hamiltonian in second order perturbation theory would be given by

$$\begin{aligned} \langle m|\mathcal{H}_{\mathrm{eff}}|n\rangle &= \sum_{|k\rangle} \frac{\langle m|\mathcal{H}_{\mathrm{kin}}|k\rangle\langle k|\mathcal{H}_{\mathrm{kin}}|n\rangle}{E_0 - E_k} \\ &= -\frac{1}{U} \sum_{|k\rangle} \langle m|\mathcal{H}_{\mathrm{kin}}|k\rangle\langle k|\mathcal{H}_{\mathrm{kin}}|n\rangle, \end{aligned} \tag{1.4}$$

where $\mathcal{H}_{\mathrm{kin}}$ is the kinetic part of Hubbard model (1.1), $|n\rangle$ and $|m\rangle$ are initial and final states (example shown in Fig. 1.1 on panels (a) and (c)), and $|k\rangle \neq |m\rangle$ is an intermediate state (for example the one shown on the Fig. 1.1 (b)). Making use of

$$\sum_{|k\rangle} |k\rangle\langle k| = \sum_j n_{j\sigma} n_{j-\sigma} \,, \tag{1.5}$$

we get

$$\mathcal{H}_{\mathrm{eff}} = -\frac{t^2}{U} \sum_{i(j)\sigma\sigma'\sigma''} c^\dagger_{i\sigma'} c_{j\sigma'} n_{j\sigma} n_{j-\sigma} c^\dagger_{j\sigma''} c_{i\sigma''} \,. \tag{1.6}$$

Taking into account the no double occupancy constraint

$$n_{j\sigma} + n_{j-\sigma} = 1 \,, \tag{1.7}$$

and summing over σ', σ'' one arrives at

$$\mathcal{H}_{\mathrm{eff}} = \frac{2t^2}{U} \sum_{\langle ij \rangle \sigma} \left(-n_{i\sigma} n_{j-\sigma} + c^\dagger_{i-\sigma} c_{i\sigma} c^\dagger_{j\sigma} c_{j-\sigma} \right). \tag{1.8}$$

To get the Heisenberg equation (1.3), one then needs to write the spin operators in the second quantization form:

$$S^z_i = \frac{1}{2} \left(n_{i\uparrow} - n_{i\downarrow} \right) , \tag{1.9}$$

$$S^+_i = c^\dagger_{i\uparrow} c_{i\downarrow} \,, \tag{1.10}$$

$$S^-_i = c^\dagger_{i\downarrow} c_{i\uparrow} \,, \tag{1.11}$$

where the particle number operator $n_i = n_{i\uparrow} + n_{i\downarrow}$. By writing the following relations:

$$\begin{aligned} S_i^z S_j^z - \frac{1}{4} n_i n_j &= (n_{i\uparrow} n_{j\downarrow} + n_{i\downarrow} n_{j\uparrow}) \ , \\ S_i^+ S_j^- + S_i^- S_j^+ &= c_{i\uparrow}^\dagger c_{i\downarrow} c_{j\downarrow}^\dagger c_{j\uparrow} + c_{i\downarrow}^\dagger c_{i\uparrow} c_{j\uparrow}^\dagger c_{j\downarrow} \, , \end{aligned} \tag{1.12}$$

we can transform Eq. (1.8) into

$$\mathcal{H}_{\text{eff}} = \frac{4t^2}{U} \sum_{\langle ij \rangle} \left(S_i^z S_j^z - \frac{n_i n_j}{4} + \frac{1}{2} \left(S_i^+ S_j^- + S_i^- S_i^+ \right) \right) , \tag{1.13}$$

which at half filling ($n_i = n_j = 1$) and upon neglecting the constant is Heisenberg model (1.3).

The same way superexchange model for a multiorbital system can be derived by considering virtual orbital-dependent exchange of electrons (i.e. hopping processes in the second order of the perturbation theory) in the strong coupling limit, see section 1.4.

Note that formally two types of interactions are distinguished: *direct* exchange, which originates from direct virtual hoppings from one magnetic ion to another, and *superexchange*, which arises as a result of virtual hoppings via neighboring ligand atoms, for instance oxygens.

1.4. Superexchange for a system with an orbital degree of freedom: iridates

To derive the superexchange model for multiorbital systems, we consider all possible virtual hoppings between different orbitals d_{xy}, d_{yz}, d_{xz} (which from now one we would refer to as xy, yz, xz) of the t_{2g} subshell starting from a multiorbital Hubbard band:

$$\begin{aligned} \mathcal{H}_{\text{Hubbard}} = &\sum_{i,j \neq i, \sigma \epsilon \epsilon'} t_{ij\epsilon\epsilon'} a_{i\sigma\epsilon}^\dagger a_{j\sigma\epsilon'} + U \sum_{i,\epsilon} n_{i\epsilon\uparrow} n_{i\epsilon\downarrow} + \left(U - \frac{5}{2} J_{\text{H}} \right) \sum_{i,\epsilon<\epsilon'} n_{i\epsilon} n_{i\epsilon'} \\ &+ J_{\text{H}} \sum_{i,\epsilon<\epsilon'} \left(d_{i\epsilon\uparrow}^\dagger d_{i\epsilon\downarrow}^\dagger d_{i\epsilon'\downarrow} d_{i\epsilon'\uparrow} + d_{i\epsilon'\uparrow}^\dagger d_{i\epsilon'\downarrow}^\dagger d_{i\epsilon\downarrow} d_{i\epsilon\uparrow} \right) - 2J_{\text{H}} \sum_{i,\epsilon<\epsilon'} \mathbf{S}_{i\epsilon} \cdot \mathbf{S}_{i\epsilon'} \, , \end{aligned} \tag{1.14}$$

where a creation operator $a_{i\sigma\epsilon}^\dagger$ now has an orbital index ϵ, and the hopping elements $t_{ij\epsilon\epsilon'}$ can depend on the orbital degree of freedom of the initial and final state, and J_H stands for Hund's exchange. We consider only spin-conserving hopping processes, hence we use everywhere only one spin index σ. Superexchange model can be derived from a multiorbital Hubbard model using the second order perturbation theory in a way similar to how t-J model was derived from the single-band Hubbard model in section 1.3.

Since deriving the superexchange model requires a defined set of orbital-dependent hopping parameters, in the following we focus on one particular case of quasi-two-dimensional square-lattice multiorbital compounds – iridates and namely Sr_2IrO_4 (see Fig. 1.2).

Distrontium iridium(IV) oxide Sr_2IrO_4 was long considered to crystallize in a layered perovskitelike structure with tetragonal $I4_1/acd$ space group [24, 43, 55]. It was shown experimentally already in 1990's that due to the rotation of IrO_6 octahedra around the tetragonal c axis, the Ir-O-Ir bond forms 157° angle instead of 180° and the Ir-O bonding length is larger than one-half of the tetragonal a axis [99]. However, recent single-crystal neutron diffraction studies also observed additional nuclear Bragg peaks that violate this space group [28, 126]. A symmetry lowering from the $I4_1/acd$ to $I4_1/a$ space group that arises [108] from a staggered tetragonal distortion of the oxygen octahedra was revealed using nonlinear optical harmonic generation (not shown on Fig. 1.2). In particular, the authors of [108] have shown that c- and d-glide planes previously thought to exist in the $I4_1/acd$

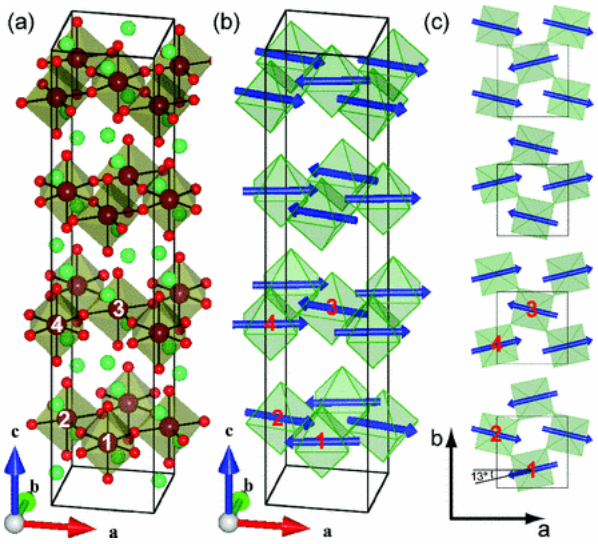

Figure 1.2.: (a) The crystal structure of Sr_2IrO_4 with space group $I4_1/acd$. Each IrO_6 octahedron is rotated by 11.8° around the c-axis. The iridium atoms of the non-primitive unit cell are labeled 1,2,3,4. (b) The magnetic ordering of $J_{\text{eff}} = 1/2$ moments, also shown in the basal plane (c). Figure adopted from Ref. [126]

description are absent, which indicates that the tetragonal distortions of the oxygen octahedra on the two sublattices are inequivalent.

In fact, there has been a long on-going discussion [15] that the octahedra rotations are to a large extent responsible for the puzzling behavior of iridates since one of the defining features of Sr_2IrO_4 and other Ir-based compounds is that the on-site spin-orbit interaction (SOI) couples physical properties to the lattice degrees of freedom strongly [35, 110, 126]. The main effect of the octahedra rotations for the polaronic kind of models which we discuss here would be an asymmetrical renormalization of hopping parameters $t_{ij\epsilon\epsilon'}$ entering the multiorbital Hubbard model (1.14), which has proved itself to be important as shown in chapter 3 and chapter 4. In our model approach we do not account for the tetragonal distortion since it will only renormalize the ground state moderately [46] and hence cannot significantly affect the low-energy effective model presented in the following. It can however be taken into account by using Clebsch-Gordan coefficients (CGC) adapted to a symmetry lower than spherical (for a model discussed here CGC for a cubic and spherical point group symmetry coincide).

Taking into account that the overlap of wave functions between two iridium atoms along $z \parallel c$-axis is greatly reduced due to the layer of Sr atoms separating the layers of iridium atoms (see Fig. 1.2), Sr_2IrO_4 can be viewed as an effectively 2D material, where iridium ions in corner-sharing oxygen octahedra are forming a square lattice. The electronic configuration of Ir^{+4} atom is $[Xe]4f^{14}5d^5$, i.e. there are five electrons in the valence d-shell. Strong tetragonal crystal-field splitting present due to the octahedral environment splits those d levels into lower t_{2g} and higher e_g subsets, i.e. one is effectively left with five electrons (or one hole) per site in the lowest t_{2g} configuration. Such a system with one hole per site is well described by the multiorbital Hubbard model (1.14), where the orbital index ϵ is indicating whether the hole is placed onto xy, yz or xz orbital.

In general, the hopping elements are orbital- and direction-dependent and can be defined from either symmetric considerations or more elaborately by fitting the dispersion calculated within a tight-binding model with corresponding hopping integrals to the band structure obtained with, for example, density functional theory (DFT). Such an approach is advantageous when a material-specific model is required – provided a sufficient number of parameters

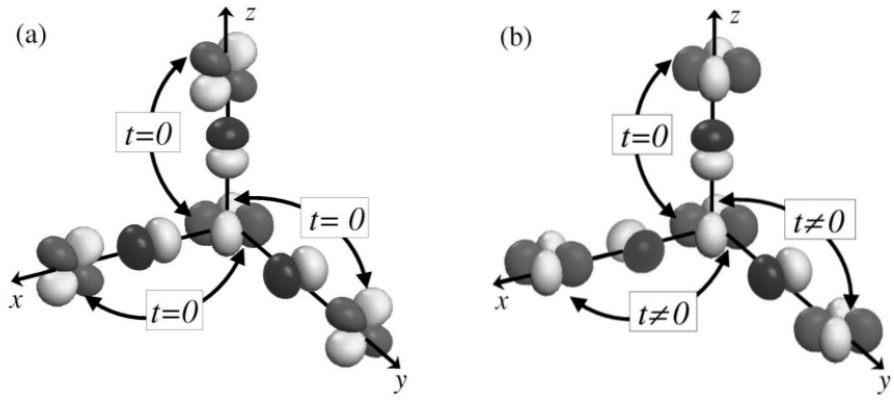

Figure 1.3.: Symmetry of the hopping matrix element for cubic site symmetry: (a) overlap between wave functions of different orbital flavors is zero provided that only the hopping between the nearest neighbor transition metal ion and the oxygen orbital is taken into account, (b) overlap between wave functions of xy character is zero along z axis. Figure adopted from Ref. [40].

were used, one can effectively account for distortions, hybridization and other effects very well. When particular structural distortions are not very important (for example, they are known to not alter the physics of the effect in focus), one can keep the amount of parameters small and define them from simple geometric considerations. Defining the hopping elements from the comparison with DFT calculations is covered in section 3.3, and here we provide a derivation from symmetricy considerations.

As seen in the cartoon 1.3, already simple geometrical considerations suggest that along the z axis, for example, a significant overlap of the wave functions of xz with xz and yz with yz orbitals would define the largest hopping parameter in the system, whereas overlap of xy wave functions is quite small, and the hopping of the electron (hole in case of Sr_2IrO_4) with xy orbital character along the z axis can be approximately set to zero. Of course, there still can be an electron (hole) on the xy orbital in a virtual two-electron intermediate state, but on an inactive orbital, i.e. it is not allowed to hop.

Virtual high-energy excitations determine the superexchange energy J and together with spin correlations decide for a spectral weight of the upper Hubbard band at half-filling. In Fig. 1.4 as an example one of such possible virtual hopping processes is shown. Here a denotes $|yz\rangle$ orbital, b – $|xz\rangle$ orbital and c – $|xy\rangle$ orbital. In a simple picture, hole with a particular spin (here up) and orbital character (here xz) hops from site i to the next neighboring site j and then back. Depending on the spin and orbital of hopping hole as well as those of the hole already residing on the site j, such virtual charge excitations can lead to one of four intermediate excited states [85]: high-spin $^3T_1$ state at energy $(U - 3J_{\rm H})$ and three low-spin states: $^1T_2$ and ^1E at energy $(U - J_{\rm H})$ and $^1A_1$ state at energy $(U + 2J_{\rm H})$. In Fig. 1.4 the triplet $^3T_1$ ($|1, 1\rangle$) is shown schematically, but please note that eigenfunctions of the d^2 configuration describing the virtual hole excitation are in general more complicated and shall be presented as linear combinations of different wave functions with certain orbital character. For detailed discussion of functions of t_{2g} see Refs. [1, 85]. Since double occupancy would cost an energy U, hopping processes in the strong coupling limit are only happening "virtually", i.e. the intermediate state has a very short actual lifetime. Each of such virtual hopping processes is described by the following Hamiltonian:

$$\hat{H}_i = T_{ij}^{\dagger} P_j T_{ij} \,, \tag{1.15}$$

where T_{ij} describes the hopping of one electron, and P_j is a projection operator:

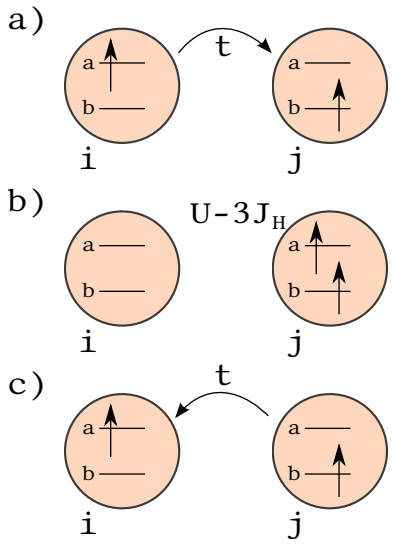

Figure 1.4.: Example of a virtual hopping process along z or y-axis creating ${}^3T_1$ virtual charge excitation (in particular, ${}^3T_1$ $1z$, see [1]) in half filled Mott insulator: (a) initial, (b) intermediate and (c) final states on two sites. Here a denotes yz orbital, b - xz orbital and c - xy orbital.

$$T_{ij} = c^\dagger_{j,a,\uparrow} c_{i,a,\uparrow} + c^\dagger_{j,b,\uparrow} c_{i,b,\uparrow}\,, \tag{1.16}$$

$$P_j = |\phi_j\rangle\langle\phi_j|\,, \tag{1.17}$$

where $|\phi_j\rangle$ is the wave function of the intermediate doubly occupied state, for the hopping process considered here as an example $|\phi_j\rangle = c^\dagger_{j,b,\uparrow} c_{j,a,\uparrow}$ describes one of the ${}^3T_1$ intermediate states.

Note that this description employs none of the simplifications used in the effective one-electron description. For a system consisting of two sites with one electron on each this is still an exact expression derived from Hubbard model provided that the set of hopping elements $t_{ij\epsilon\epsilon'}$ is extensive. For a crystal, a system of infinitely many sites, this is not exact anymore, however still a very good approximation when short-range hopping elements are much larger than long range ones, i.e. wave functions are rather localized. However, even for systems with more extended wave functions this approach can give good agreement with experiment if the set of hopping integrals is extended. For instance, it was suggested recently [2] that Sr_2IrO_4 and iridates in general are negative charge transfer systems with large covalency and interactions longer than first neighbor have to be taken into account – indeed as it will be shown in chapters 2 – 3 we had to extend the set of hopping parameters as well as superexchange parameters for Sr_2IrO_4 up to the third neighbor in order to capture all the details observed experimentally.

The same way as before one can consider all possible hopping processes for a particular system with one charge carrier per cite (for two and more electrons/holes Eqs. (1.15 – 1.17) shall be generalized.) For our system of interest, one hole in t_{2g} shell, there are 15 intermediate virtual states: three triplets of ${}^3T_1$ character, one triplet ${}^1T_2$, two singlets ${}^1E$ and one singlet ${}^1A_1$ [38] to be considered. After straightforward but tedious calculations, including summing up all possible hopping processes, substituting $\tilde{c}^\dagger_{i\sigma} = (1 - n_{i-\sigma})\, c^\dagger_{i\sigma}$ which takes care of projecting out the double occupancies and then introducing spin- and *pseudospin-*

(i.e. orbital) operators (S and τ correspondingly) given by

$$S_i^+ = \tilde{c}_{i\uparrow}^\dagger \tilde{c}_{i\downarrow}\,, \tag{1.18}$$

$$S_i^- = \tilde{c}_{i\downarrow}^\dagger \tilde{c}_{i\uparrow}\,, \tag{1.19}$$

$$S_i^z = \frac{\tilde{n}_{i\uparrow} - \tilde{n}_{i\downarrow}}{2} \tag{1.20}$$

and

$$\tau_{i,\|c}^+ = \tilde{c}_{i,a}^\dagger \tilde{c}_{i,b}\,, \tag{1.21}$$

$$\tau_{i,c}^- = \tilde{c}_{i,b}^\dagger \tilde{c}_{i,a}\,, \tag{1.22}$$

$$\tau_{i,c}^z = \frac{\tilde{n}_{i,a} - \tilde{n}_{i,b}}{2}\,, \tag{1.23}$$

we obtain the *superexchange spin-orbital model* for an ideal perovskite structure of the t_{2g}^1 configuration [85], which is also referred to as Kugel-Khomskii model ([64]):

$$\mathcal{H} = \mathcal{H}_1 + \mathcal{H}_2 + \mathcal{H}_3\,, \tag{1.24}$$

$$\begin{aligned} \mathcal{H}_1 &= \frac{1}{2} J r_1 \left(\mathbf{S}_i \cdot \mathbf{S}_j + \frac{3}{4}\right)\left(A_{ij}^{(\gamma)} - \frac{1}{2} n_{ij}^{(\gamma)}\right), \\ \mathcal{H}_2 &= \frac{1}{2} J r_2 \left(\mathbf{S}_i \cdot \mathbf{S}_j - \frac{1}{4}\right)\left(A_{ij}^{(\gamma)} - \frac{2}{3} B_{ij}^{(\gamma)} + \frac{1}{2} n_{ij}^{(\gamma)}\right), \\ \mathcal{H}_3 &= \frac{1}{3} J r_3 \left(\mathbf{S}_i \cdot \mathbf{S}_j - \frac{1}{4}\right) B_{ij}^{(\gamma)}\,. \end{aligned} \tag{1.25}$$

Here orbital operators $A_{ij}^{(\gamma)}$, $B_{ij}^{(\gamma)}$ describe the interactions between active orbitals along a particular bond γ:

$$A_{ij}^{(\gamma)} = 2\left(\boldsymbol{\tau}_i \cdot \boldsymbol{\tau}_j + \frac{1}{4} n_i n_j\right)^{(\gamma)}, \tag{1.26}$$

$$B_{ij}^{(\gamma)} = 2\left(\boldsymbol{\tau}_i \otimes \boldsymbol{\tau}_j + \frac{1}{4} n_i n_j\right)^{(\gamma)},$$

$$n_{ij}^{(\gamma)} = n_i^{(\gamma)} + n_j^{(\gamma)}, \tag{1.27}$$

$$\boldsymbol{\tau}_i \otimes \boldsymbol{\tau}_j = \tau_i^x \tau_j^x - \tau_i^y \tau_j^y + \tau_i^z \tau_j^z\,, \tag{1.28}$$

and coefficients r_i characterize the multiplet structure of excited states and depend solely on the $\eta = J_H/U$ ratio between Hund's coupling and Hubbard U:

$$r_1 = \frac{1}{1-3\eta}\,, \tag{1.29}$$

$$r_2 = \frac{1}{1-\eta}\,, \tag{1.30}$$

$$r_3 = \frac{1}{1+2\eta}\,. \tag{1.31}$$

1.5. On-site spin-orbit coupling

Strong Coulomb repulsion could localize the electrons of a partly filled d-shell of a transition metal (TM) compound in Mott-Hubbard regime as discussed in section 1.3.

If then the symmetry of the local surrounding of the atom is low enough to lift the orbital degeneracy (i.e. the system is effectively single-band), it can be described by the single-band Hubbard model and spin-only superexchange Hamiltonian (see section 1.3). However, often the orbital degeneracy is present in a TM ion, and the orbitals can form a long-range ordered pattern. In strongly correlated materials such an orbital ordering can be driven by exchange or Jahn-Teller interactions, which is to be discussed in chapter 2. In these cases corresponding superexchange model shall of course include both spin and orbital degrees of freedom.

Such superexchange spin-orbital models derived from the multiorbital Hubbard model already introduce some entanglement between spin and orbital degrees of freedom, so the latter cannot be treated independently anymore, however, both spin and orbital momenta are still conserved and hence are good quantum numbers. This is however not the case anymore when on-site spin-orbit coupling is present, where the total momentum **J** shall be considered instead (for here on we will refer to **j** for a one-particle state and to **J** for a state with more than one electron). On-site spin-orbit coupling Hamiltonian can be written as

$$\mathcal{H}_{\mathrm{SOC}} = \lambda \sum_i \mathbf{l}_i \cdot \mathbf{s}_i \,, \tag{1.32}$$

where for the case of one particle per site $\lambda = \xi_i$ is the one particle spin-orbit coupling. In the so called *strong SOC regime*, i.e. when $\lambda \gg J$ (where $J = 4t^2/U$ is the Heisenberg spin exchange defined in Eq.1.3), it is convenient to work in the basis of total **j** momentum, in which the largest contribution to the total Hamiltonian of the system, i.e. the on-site SOC Hamiltonian is diagonal.

For this reason we make a basis transformation from the basis set of $\mathrm{t_{2g}}$ orbitals

$$\hat{t} = (|yz,\uparrow\rangle, |yz,\downarrow\rangle, |xz,\uparrow\rangle, |xz,\downarrow\rangle\,, |xy,\uparrow\rangle, |xy,\downarrow\rangle)\,, \tag{1.33}$$

which is connected to "$\mathbf{l}\cdot\mathbf{s}$-basis" as

$$\begin{aligned} |l_z = 0\rangle &= |xy\rangle, \\ |l_z = \pm 1\rangle &= -\frac{1}{\sqrt{2}}(\pm|yz\rangle + i|xz\rangle) \end{aligned} \tag{1.34}$$

into the **j**-basis (also called *isospin* or sometimes *pseudospin* in the literature, see e.g. [46])

$$\hat{j} = \left(|\tfrac{1}{2},\tfrac{1}{2}\rangle, |\tfrac{1}{2},\tfrac{-1}{2}\rangle, |\tfrac{3}{2},\tfrac{3}{2}\rangle, |\tfrac{3}{2},\tfrac{1}{2}\rangle, |\tfrac{3}{2},\tfrac{-1}{2}\rangle, |\tfrac{3}{2},\tfrac{-3}{2}\rangle\right)\,. \tag{1.35}$$

Using tables with Clebsch-Gordan coefficients (see appendix B) or the high-weight decomposition method (see section 5.2 for details) one can express this basis transformation as

$$\hat{j} = \begin{pmatrix} 0 & -\frac{1}{\sqrt{3}} & 0 & -\frac{i}{\sqrt{3}} & -\frac{1}{\sqrt{3}} & 0 \\ -\frac{1}{\sqrt{3}} & 0 & \frac{i}{\sqrt{3}} & 0 & 0 & \frac{1}{\sqrt{3}} \\ -\frac{1}{\sqrt{2}} & 0 & -\frac{i}{\sqrt{2}} & 0 & 0 & 0 \\ 0 & -\frac{1}{\sqrt{6}} & 0 & -\frac{i}{\sqrt{6}} & \sqrt{\frac{2}{3}} & 0 \\ \frac{1}{\sqrt{6}} & 0 & -\frac{i}{\sqrt{6}} & 0 & 0 & \sqrt{\frac{2}{3}} \\ 0 & \frac{1}{\sqrt{2}} & 0 & -\frac{i}{\sqrt{2}} & 0 & 0 \end{pmatrix} \hat{t}\,. \tag{1.36}$$

Due to large on-site spin-orbit coupling, three $\mathrm{t_{2g}}$ levels split into lower $\mathbf{j} = 3/2$ quartet and higher $\mathbf{j} = 1/2$ doublet, which are then filled by five electrons present in the *d*-shell, leaving one hole on the $\mathbf{j} = 1/2$ doublet. Thus adding strong on-site SOC reduces the effective low-energy model from three-band to $\mathbf{j} = 1/2$ single-band problem. Such $\mathbf{j} = 1/2$ state is schematically shown in Fig. 1.5.

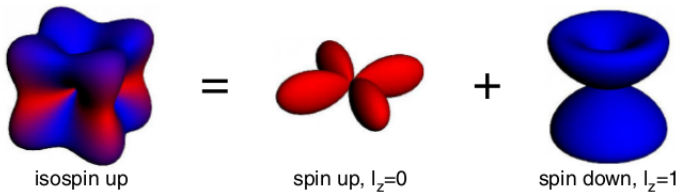

Figure 1.5.: Schematic picture of the isospin up state $\mathbf{j} = |1/2, 1/2\rangle$ which is a superposition of a spin up electron with $l_z = 0$ (i.e. placed onto $|xy\rangle$ orbital) and spin down electron with $l_z = 1$ (i.e. with orbital character $|yz\rangle + i|xz\rangle$). Figure adopted from Ref. [46]

When projected onto spin-orbit coupled basis (1.36) the spin-orbital exchange Hamiltonian (1.24) in the lowest doublet takes the form

$$\mathcal{H}_{i,j} = J_1 \mathbf{S}_i \cdot \mathbf{S}_j + J_2 \left(\mathbf{S}_i \cdot \mathbf{r}_{ij}\right)\left(\mathbf{r}_{ij} \cdot \mathbf{S}_j\right) , \tag{1.37}$$

where $\mathbf{S}_i$ is now the operator for isospin, i.e. effective total moment, $\mathbf{r}_{ij}$ is the unit vector along ij bond, and $J_{1(2)} = \frac{4}{9}\nu_{1(2)}$ where parameters $\nu_{1(2)}$ governing isotropic (anisotropic) couplings are defined as [46] $\nu_1 = (3r_1 + r_2 + 2r_3)/6$ and $\nu_2 = (r_1 - r_2)/4$ with r_i given in Eq. (1.29). Assuming Hund's coupling is relatively small and substituting $J_H = 0$ in Eq. (1.24) we see that J_2 turns to zero too and Hamiltonian (1.37) reduced to the Heisenberg model

$$\mathcal{H}_{i,j} = J_1 \mathbf{S}_i \cdot \mathbf{S}_j. \tag{1.38}$$

This unexpected reduction of multi-band Hubbard model to the simple Heisenberg model in the strong on-site spin-orbit coupling limit was first demonstrated by G. Jackeli and G. Khaliullin [46] on an example of square-lattice iridates and brought a lot of attention to the latter, since it suggests that this class of materials can resemble famous cuprates not only structurally (remember similarities between Sr_2IrO_4 and La_2CuO_4) but also on the level of effective low-energy models.

1.6. Magnetic polarons

As was shown in section 1.4, a complicated Hamiltonian (1.24) describing superexchange in Sr_2IrO_4 in the limit of strong spin-orbit coupling reduces to the simple Heisenberg Hamiltonian. Later experiments have shown that the wave functions of iridium atoms are rather extended and, in fact, one has to also include up to third neighbor interactions to the Heisenberg model (see chapter 2 for detailed discussion), however, the key point is that the AF $j_{\text{eff}} = \frac{1}{2}$ ground state of Sr_2IrO_4 can be described by an effective low-energy Heisenberg spin model. In such a case any kind of excitation introduced into this ground state, be it a charge, or orbital, or of any other nature, can be described by a model resembling the t-J model, which can then be mapped on a polaronic model as done in Ref. [74] and then solved semianalytically. This in few words covers what we will be doing in following chapters.

Throughout this thesis we construct magnetic polaronic models and solving them using self-consistent Born approximation to address the effects we are interested in. Thus, we first transform the low-energy effective model in focus (e.g. t-J model) into the polaronic language by separating degrees of freedom (e.g. spinless fermions (holons) and spin-wave operators (magnons)) and secondly we calculate the Green's function of the excitation we are interested in to get spectral function as its imaginary part. In this section we present main ideas of this

approach mostly focusing on the simple case of "single-hole problem", more elaborate cases shall be discussed in chapters 2 through 4

The approach is in general analytical, which gives control and transparency to understand certain phenomena, but consequently it also has its limitations. First of all, the presence of polaronic physics in the system of interest is vital, i.e. the method is suitable for describing an excitation introduced to the ground state of the system which then propagates interacting with the low-energy bosonic excitations of the ground state. For example, in the famous work by S. Schmitt-Rink *et al.* [97], a single hole introduced into an antiferromagnet gets "dressed" by magnons while it propagates in the AF background. This being said, the ground state has to be known in advance and introduced in the model by hand, the set of bosonic excitations to be considered is also limited. Following original works [50, 74, 97] we use SCBA to calculate the Green's function of the excitation, in which bosons are assumed to be (i) not renormalized back by the fermionic excitation and (ii) not interacting with each other (so called *non-crossing* or *rainbow* approximation). We will discuss SCBA in some more details in section 1.7.

However, notwithstanding all the limitations the method is very powerful since it provides an almost exact solution of the one nontrivial limit of the 2D doped Hubbardlike problems, so-called "single-hole problem", which relates to the motion of a single charge added to the AF and insulating ground state of the undoped 2D Hubbardlike model.

Consequently, polaronic approach being extended from simple toy model to realistic representation can also describe many of the experiments on strongly correlated materials that can in the first approximation be seen as a creation of some sort of excitation (charge, spin, etc.) using for instance light or neutrons in the ground state of the material and then measuring the energy and/or momenta of the outgoing light (or neutron) after the excitation has relaxed. we will cover experimental applications in chapter 3 where, for instance, an electron is kicked out in the photoemission process, in chapter 4 where an on-site occupation is changed due to the bias shift in scanning tunneling spectroscopy and in chapter 2 where a *d-d* excitation is created in resonant inelastic x-ray scattering (RIXS).

To start with, let me present the main idea of the magnetic polaronic approach on the well-studied example of the *t-J* model following the derivation in Ref. [74]. Isotropic *t-J* model was already given in Eq. (1.2):

$$\mathcal{H}_{t\text{-}J} = -\sum_{\langle i,j\rangle,\sigma}\left(t_{ij\sigma}\left(1-n_{i-\sigma}\right)c^{\dagger}_{i\sigma}c_{j\sigma}\left(1-n_{j-\sigma}\right)+\text{h.c.}\right)+J\sum_{\langle i,j\rangle}\left(\mathbf{S}_i\cdot\mathbf{S}_j-\frac{n_i n_j}{4}\right). \quad (1.39)$$

This equation describes the motion of charge carriers (a single hole in the limiting case) in the fluctuating AF background (provided $J > 0$). Let us consider first the *t*- part of the Hamiltonian (1.39)

$$\mathcal{H}_t = -t\sum_{\langle i,j\rangle,\sigma}\left[\left(1-n_{i-\sigma}\right)c^{\dagger}_{i\sigma}c_{j\sigma}\left(1-n_{j-\sigma}\right)+\left(1-n_{j-\sigma}\right)c^{\dagger}_{j\sigma}c_{i\sigma}\left(1-n_{i-\sigma}\right)\right]. \quad (1.40)$$

It is more convenient to rewrite Eq. (1.40) so that the summation is taken over individual neighbors rather than over bonds:

$$\mathcal{H}_t = -t\sum_{i,j(i),\sigma}\left[\left(1-n_{i-\sigma}\right)c^{\dagger}_{i\sigma}c_{j\sigma}\left(1-n_{j-\sigma}\right)\right]. \quad (1.41)$$

Since we are considering the AF ground state, there exist two distinct magnetic sublattices. To account for this, we divide the Hamiltonian into two parts, A and B sublattices (and this

is where the ground state of the system is implicitly included into the model):

$$\begin{aligned}\mathcal{H}_t = &- t \sum_{i\in\mathrm{A},j(i),\sigma} \left[(1-n_{i-\sigma})\, c^\dagger_{i\sigma} c_{j\sigma}\,(1-n_{j-\sigma})\right] \\ &- t \sum_{i\in\mathrm{B},j(i),\sigma} \left[(1-n_{i-\sigma})\, c^\dagger_{i\sigma} c_{j\sigma}\,(1-n_{j-\sigma})\right].\end{aligned} \tag{1.42}$$

Next convenient step to make is to perform a rotation of the spins on the B "spin down" sublattice by 180° so that we can effectively treat the system as a ferromagnet (all the AF physics is however preserved):

$$c_{j\sigma} \to c_{j-\sigma}\,. \tag{1.43}$$

Applying spin rotation to Eq. (1.42) we get

$$\begin{aligned}\mathcal{H}_t = &- t \sum_{i\in\mathrm{A},j(i),\sigma} \left[(1-n_{i-\sigma})\, c^\dagger_{i\sigma} c_{j-\sigma}\,(1-n_{j\sigma})\right] \\ &- t \sum_{i\in\mathrm{B},j(i),\sigma} \left[(1-n_{i\sigma})\, c^\dagger_{i-\sigma} c_{j\sigma}\,(1-n_{j-\sigma})\right],\end{aligned} \tag{1.44}$$

summing up A and B sublattices:

$$\mathcal{H}_t = -t \sum_{i,j(i),\sigma} \left[(1-n_{i-\sigma})\, c^\dagger_{i\sigma} c_{j-\sigma}\,(1-n_{j\sigma})\right]. \tag{1.45}$$

The separation of charge and spin degrees of freedom shall be now performed by means of Holstein-Primakoff transformation, which for the case of spin $S_i = \frac{1}{2}$ reads

$$\begin{aligned} c_{i\uparrow} &= h^\dagger_i\,, \\ c^\dagger_{i\uparrow} &= h_i\,, \\ c_{i\downarrow} &= h^\dagger_i a_i\,, \\ c^\dagger_{i\downarrow} &= a^\dagger_i h_i\,, \end{aligned} \tag{1.46}$$

where $h^\dagger_i$ is a fermionic operator creating charge excitation (here, a hole), and boson $a^\dagger_i$ accounts for the spin degree of freedom. In this notation the basic constraint of the t-J model, namely, no double occupied configurations $|\uparrow\downarrow\rangle$

$$(1-n_{i\downarrow}) c^\dagger_{i,\uparrow} |\downarrow\rangle = 0 \tag{1.47}$$

is automatically fulfilled. Therefore we can rewrite Hamiltonian (1.45) as

$$\mathcal{H}_t = -t \sum_{i,j(i)} \left[c^\dagger_{i\sigma} c_{j-\sigma}\right], \tag{1.48}$$

and then applying (1.46) to (1.48) we get

$$\mathcal{H}_t = -t \sum_{i,j(i)} \left[h_i h^\dagger_j a_j + \mathrm{h.c.}\right]. \tag{1.49}$$

In similar way one gets the remaining part of $\mathcal{H}_{t-J}$ (for more details see [74]):

$$\begin{aligned} \mathcal{H}_{t\text{-}J} &= \mathcal{H}_t + \mathcal{H}_J - \frac{Z}{2} JN \left(s^2 + \frac{1}{4}\right)(1-\delta)^2\,, \\ \mathcal{H}_t &= -t \sum_{i,j(i)} \left[h_i h^\dagger_j a_j + \mathrm{h.c.}\right], \\ \mathcal{H}_J &= \frac{J}{4} \sum_{i,j(i)} h_i h^\dagger_i \left(a_i a_j + a^\dagger_i a^\dagger_j + a^\dagger_i a_i + a^\dagger_j a_j\right) h_j h^\dagger_j\,. \end{aligned} \tag{1.50}$$

Here Z is the coordinate number which indicates the number of nearest neighbors: for a 1D chain $Z = 2$ and for 2D square-lattice $Z = 4$, $s = \frac{1}{2}$ is the absolute value of spin and N is the total number of sites. Hole concentration δ in the limiting case of a single hole can be set to zero so that $(1-\delta)^2 = 1$.

As one can see, Eq. (1.50) has linear part $\mathcal{H}_t$ describing hole motion and quadratic part $\mathcal{H}_J$ depicting low-energy spin excitations. To treat the part $\mathcal{H}_J$ describing low-energy bosonic interactions we employ mean-field approximation and replace $h_i h_i^\dagger = \left(1 - h_i^\dagger h_i\right)$ by $(1-\delta) = 1$. Then the quadratic part can easily be diagonalized by means of Fourier and Bogoliubov transformations. In second quantization formalism Fourier transformation asserts

$$\begin{aligned} a_{\mathbf{k}}^\dagger &= \frac{1}{\sqrt{N}} \sum_i e^{i\mathbf{k}\mathbf{r}_i} a_i^\dagger \,, \\ a_{\mathbf{k}} &= \frac{1}{\sqrt{N}} \sum_i e^{-i\mathbf{k}\mathbf{r}_i} a_i \,. \end{aligned} \tag{1.51}$$

Reversed Fourier transformation then reads

$$\begin{aligned} a_i^\dagger &= \frac{1}{\sqrt{N}} \sum_{\mathbf{k}} e^{-i\mathbf{k}\mathbf{r}_i} a_{\mathbf{k}}^\dagger \,, \\ a_i &= \frac{1}{\sqrt{N}} \sum_{\mathbf{k}} e^{i\mathbf{k}\mathbf{r}_i} a_{\mathbf{k}} \,. \end{aligned} \tag{1.52}$$

After application of Fourier transformation 1.52, quadratic part of Hamiltonian (1.50) $\mathcal{H}_J$ becomes (for more details here and further see [77] and [74])

$$\begin{aligned} \mathcal{H}_J =& \frac{J}{4N} \sum_{i,\boldsymbol{\tau},\mathbf{k}_1,\mathbf{k}_2} \left[e^{i(\mathbf{k}_1+\mathbf{k}_2)\mathbf{r_i} + i\mathbf{k}_2\boldsymbol{\tau}} a_{\mathbf{k}_1} a_{\mathbf{k}_2} + e^{-i(\mathbf{k}_1+\mathbf{k}_2)\mathbf{r_i} - i\mathbf{k}_2\boldsymbol{\tau}} a_{\mathbf{k}_1}^\dagger a_{\mathbf{k}_2}^\dagger \right] + \\ &+ \frac{J}{4N} \sum_{i,\boldsymbol{\tau},\mathbf{k}_1,\mathbf{k}_2} \left[e^{i(\mathbf{k}_2-\mathbf{k}_1)\mathbf{r_i}} a_{\mathbf{k}_1}^\dagger a_{\mathbf{k}_2} + e^{i(\mathbf{k}_2-\mathbf{k}_1)(\mathbf{r_i}+\boldsymbol{\tau})} a_{\mathbf{k}_1}^\dagger a_{\mathbf{k}_2} \right] \\ =& \frac{J}{4} (1-\delta)^2 \sum_{\boldsymbol{\tau}} \sum_{\mathbf{k}} e^{-i\mathbf{k}\boldsymbol{\tau}} a_k a_{-k} + e^{i\mathbf{k}\boldsymbol{\tau}} a_k^\dagger a_{-k}^\dagger + 2 a_k^\dagger a_k \,. \end{aligned} \tag{1.53}$$

Here we used the identity

$$\frac{1}{N} \sum_i e^{-i(\mathbf{k}_1 - \mathbf{k}_2)\mathbf{r_i}} = \delta_{\mathbf{k}_1 \mathbf{k}_2} \,. \tag{1.54}$$

Then, we apply Bogoliubov transformation

$$\begin{aligned} \alpha_{\mathbf{k}} &= u_{\mathbf{k}} a_{\mathbf{k}} - v_{\mathbf{k}} a_{-\mathbf{k}}^\dagger \,, \\ \alpha_{-\mathbf{k}}^\dagger &= u_{-\mathbf{k}} a_{-\mathbf{k}}^\dagger - v_{\mathbf{k}} a_{\mathbf{k}} \,, \end{aligned} \tag{1.55}$$

and get

$$\mathcal{H}_J = \sum_q \omega_q \alpha_q^\dagger \alpha_q + \text{const} \,, \tag{1.56}$$

where spin-wave energy $\omega_{\mathbf{k}} = zsJ\nu_{\mathbf{k}}$ and the Bogoliubov coherence factors are defined as

usually in linear spin wave theory:

$$\begin{aligned} u_{\mathbf{k}} &= \sqrt{\frac{cz+\omega_{\mathbf{k}}}{2\omega_k}}\,, \\ v_{\mathbf{k}} &= -\mathrm{sign}\,(\gamma_{\mathbf{k}})\sqrt{\frac{cz-\omega_{\mathbf{k}}}{2\omega_k}}\,, \\ \nu_{\mathbf{k}} &= \sqrt{1-\gamma_{\mathbf{k}}^2}, \\ \gamma_{\mathbf{k}} &= \frac{1}{z}\sum_{\boldsymbol{\tau}} \mathrm{cos}\mathbf{k}\cdot\boldsymbol{\tau}\,. \end{aligned} \tag{1.57}$$

(1.58)

Now we apply the same transformation to the linear part $\mathcal{H}_t$ of Eq. (1.50). First, we perform Fourier transformation (1.51) and after making use of (1.54) we get

$$\mathcal{H}_t = -\frac{t}{\sqrt{N}}\sum_{\mathbf{k},\mathbf{q}}\sum_{\boldsymbol{\tau}}\left[h_{\mathbf{k}-\mathbf{q}}h_{\mathbf{k}}^{\dagger}a_{-\mathbf{q}}^{\dagger}\mathrm{cos}\mathbf{k}\cdot\boldsymbol{\tau} + h_{\mathbf{k}-\mathbf{q}}h_{\mathbf{k}}^{\dagger}a_{\mathbf{q}}\mathrm{cos}\,(\mathbf{k}-\mathbf{q})\cdot\boldsymbol{\tau}\right]. \tag{1.59}$$

Then we apply reversed Bogoliubov transformation

$$\begin{aligned} a_{\mathbf{k}} &= u_{\mathbf{k}}\alpha_{\mathbf{k}} + v_{\mathbf{k}}\alpha_{-\mathbf{k}}^{\dagger}\,, \\ a_{-\mathbf{k}}^{\dagger} &= v_{\mathbf{k}}\alpha_{\mathbf{k}} + u_{\mathbf{k}}\alpha_{-\mathbf{k}}^{\dagger} \end{aligned} \tag{1.60}$$

and get

$$\mathcal{H}_t = -\frac{zt}{\sqrt{N}}\sum_{\mathbf{k},\mathbf{q}} M\,(\mathbf{k},\mathbf{q})\,h_{\mathbf{k}}^{\dagger}h_{\mathbf{k}-\mathbf{q}}\alpha_{\mathbf{q}} + \mathrm{h.c.}\,, \tag{1.61}$$

where the vertex is defined as

$$M\,(\mathbf{k},\mathbf{q}) = \left(\gamma_{\mathbf{k}}v_{\mathbf{q}} + \gamma_{\mathbf{k}-\mathbf{q}}u_{\mathbf{q}}\right)\,. \tag{1.62}$$

Thus, we have obtained the t-J model in the form of polaronic Hamiltonian (1.56) – (1.61):

$$\mathcal{H} = \mathcal{H}_J + \mathcal{H}_t, \tag{1.63}$$

which describes the motion of a charge excitation (often referred to as holon) strongly coupled to the bosonic spin-wave excitations.

1.7. Self-consistent Born approximation

Having obtained t-J model in the polaronic form, one can calculate the Green's function of the holon with momentum $\mathbf{k}$ and energy ω as

$$G^h(\mathbf{k},\omega) = \langle 0|h_{\mathbf{k}}\frac{1}{\omega-\mathcal{H}+i\delta}h_{\mathbf{k}}^{\dagger}|0\rangle\,, \tag{1.64}$$

where $\mathcal{H}$ is given by 1.63, the operator $h_{\mathbf{k}}^{\dagger}$ denotes creation of the spinless fermion with momentum $\mathbf{k}$. The vacuum state $|0\rangle$ with respect to the spin-wave operators $\alpha_{\mathbf{q}}$ is the quantum Néel state

$$|0\rangle = \exp(\sum_{\mathbf{q}}\frac{v_{\mathbf{q}}}{u_{\mathbf{q}}}a_{\mathbf{q}}^{\dagger}a_{-\mathbf{q}}^{\dagger})|N\rangle\,, \tag{1.65}$$

where $|N\rangle$ is the classical Néel state.

In the simple case of a t-J model, operator $h_{\mathbf{k}}^{\dagger}$ creates a spinless hole (hence the name holon), but depending on the problem it can also describe creation of a d-d excitation, an

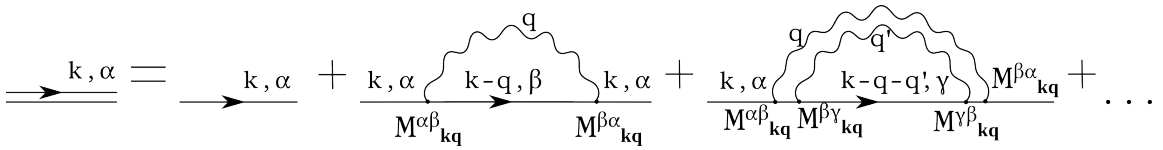

Figure 1.6.: Leading diagrams included within SCBA. The solid line represents holon propagator, curvy line – bare propagator of the spin-wave excitation. The momentum of holon and boson as well as the internal degree of freedom of the holon α,β are given for each propagator, vertces $M_{\alpha\beta}(\mathbf{k},\mathbf{q})$ describing the coupling between holon and boson are also shown. Diagrams with crossing boson propagators and double-magnon processes that would be described by four-particle vertex are not considered within SCBA.

electron, or even some more complicated spinless excitation with an internal degree of freedom – in this case $\mathbf{G}^h$ will take matrix form and the operator $h^\dagger_{\mathbf{k}}$ would acquire an index α to indicate corresponding degree of freedom

$$G^h_{\alpha\alpha}(\mathbf{k},\omega) = \langle 0|h_{\alpha\mathbf{k}}\frac{1}{\omega-\mathcal{H}+i\delta}h^\dagger_{\alpha\mathbf{k}}|0\rangle\,. \tag{1.66}$$

Such an internal degree of freedom can account for example for a singlet/triplet character of a two-hole charge excitation. This particular case of complicated charge excitation can be seen in chapter 3, where we discuss application of the polaronic formalism to the photoemission spectroscopy on iridates.

To calculate the Green's function of the holon (1.66) we use self-consistent Born approximation. The SCBA is a well-established quasi-analytical method which, in the language of Feynman diagrams, can be understood as a summation of all so-called *noncrossing* diagrams of the polaronic model as shown in Fig. 1.6. It turns out that for spin polaronic models (as e.g. those discussed here) this approximate method works very well: the contribution of the diagrams with crossed bosonic propagators to the electronic Green's function can be easily neglected [70, 98, 107]. For more details on the method itself see the pioneering works [50, 74, 97].

The Green's function(1.66) is connected to the self-energy $\mathbf{\Sigma}(\mathbf{k},\omega)$ via Dyson's equation [72]

$$\begin{aligned} G^h_{\alpha\alpha}(\mathbf{k},\omega) &= \frac{1}{\omega - E_\alpha - \epsilon^{\alpha\alpha}_{\mathbf{k}} - \Sigma_{\alpha\alpha}(\mathbf{k},\omega)+i\delta}\,,\\ G^h_{\alpha\beta}(\mathbf{k},\omega) &= \frac{1}{\epsilon^{\alpha\beta}_{\mathbf{k}} - \Sigma_{\alpha\beta}(\mathbf{k},\omega)}\,, \end{aligned} \tag{1.67}$$

where E_α is the energy onset of the holon in a state α, $\epsilon^{\alpha\beta}_{\mathbf{k}}$ describes free propagation of a holon (i.e. propagation without coupling to bosons). In the case of the classical t-J model a holon has no internal degree of freedom, $\alpha=\beta=1$, and $\epsilon_{\mathbf{k}}$ is simply the dispersion of a bare holon. A small broadening δ is added to allow for numerical treatment of Eq. (1.67) poles, analytically $\delta\to 0$. In practice, calculating Green's function (1.67) amounts to calculating the self-energy in iterative fashion

$$\Sigma_{\alpha\beta}(\mathbf{k},\omega) = \frac{z^2t^2}{N}\sum_{\mathrm{q}}\frac{M^2_{\alpha\beta}(\mathbf{k},\mathbf{q})}{\omega-\omega_{\mathrm{q}}-\epsilon^{\alpha\beta}_{\mathbf{k}}-\Sigma_{\alpha\beta}(\mathbf{k}-\mathbf{q},\omega-\omega_{\mathrm{q}})+i\delta}\,, \tag{1.68}$$

assuming that for high enough energies ω_0 there is no coupling to bosons, i.e. $\mathbf{\Sigma}(\mathbf{k},\omega_0)=0$. It is therefore important to start the iterative summation from ω_0, for which this approximation holds well. This cutoff would depend on the problem but can be estimated well from the

form of the polaronic Hamiltonian and the characteristic energy of the boson. Here $\mathbf{q}$ is the momentum and $\omega_{\mathbf{q}}$ is the energy of the boson and vertex describing coupling between holon and boson $M_{\alpha\beta}(\mathbf{k},\mathbf{q})$ acquired matrix structure to account for the holon's character.

Although the SCBA method is in principle an analytical method, the iterating SCBA equations (1.67) – (1.68) have to be solved numerically, in order to obtain results which can be compared with the experiment. Then the spectral function of a holon (or any other fermionic excitation depending on the polaronic problem considered) can be obtained as

$$A(\mathbf{k},\omega) = -\frac{1}{\pi}\mathrm{Tr}\left(\mathrm{Im}\mathbf{G}(\mathbf{k},\omega)\right) . \tag{1.69}$$

By taking particular diagonal entries of imaginary oart of the Green's function $\mathbf{G}(\mathbf{k},\omega)$ rather than the trace, one can calculate contribution of the qusiparticle $h^{\dagger}_{\alpha\mathbf{k}}$ with a particular degree of freedom α to the total dispersion. For example, this is done in section 3.5 where the holon has an internal multiplet structure and manifestation of different components of the latter in the spectral function is studied. In cases where α indicates, for instance, spin or orbital degree of freedom, it is possible to compare such theoretical spectral functions with orbital- or spin- resolved measurements, for example, orbital- and spin-resolved ARPES.

CHAPTER 2

Interplay of strong correlation, spin orbit coupling and electron-phonon interactions

and the effect of lattice degrees of freedom on resonant inelastic x-ray scattering spectra of Sr_2IrO_4

2.1. Preface

In this chapter we discuss the role of the electron-phonon coupling in the form of Jahn-Teller effect in the strongly correlated materials with severe on-site spin-orbit coupling. In section 2.2 we describe a quasiparticle recently probed in Sr_2IrO_4 by RIXS which can be seen as an excitation from $j_{\text{eff}} = 1/2$ doublet to $j_{\text{eff}} = 3/2$ quartet. We discuss how a polaronic Hamiltonian can be constructed that describes the propagation of this exciton and will show that even if it is derived from a pure superexchange (SE) model, this polaronic model gives a good agreement with the experiment [58, 59]. Then we show how electron-phonon interaction can be taken into account in the model in order to address some discrepancies between SE-based theory and experiment. First, we introduce general Jahn-Teller effect in section 2.3, in particular for systems with strong on-site SOC. Then in section 2.4 we cover in detail the derivation of the polaronic model describing the Jahn-Teller assistant motion of the spin-orbit exciton and calculation of the spectral functions. We will also describe unique features arising from this novel channel of exciton propagation and compare obtained theoretical spectra to experiment [58, 59]. Main conclusions will be highlighted in section 2.5.

Part of this chapter is published as E. M. Plotnikova, M. Daghofer, J. van den Brink and K. Wohlfeld, "Jahn-Teller effect in systems with strong on-site spin-orbit coupling", in: *Phys. Rev. Lett.* **116** (10 2016), p. 106401.

2.2. Spin-orbit exciton in Sr_2IrO_4 measured by RIXS

As we discussed in chapter 1, in the strong on-site spin-orbit coupling limit the multi-band Hubbard model reduces to the simple Heisenberg model. Indeed, as it was shown in Ref. [46], the magnon dispersion in Sr_2IrO_4 can be described by Heisenberg Hamiltonian (1.38). Experimental evidence followed, although with some delay since large enough single crystals of Sr_2IrO_4 are not easy to obtain. Moreover, inelastic neutron scattering, a commonly used technique for measuring magnon dispersion (see. e.g. [22]) is difficult to apply in the case of iridates due to the high neutron absorption cross section of iridium.

When $j_{\text{eff}} = 1/2$ spin-orbital Mott state in Sr_2IrO_4 was observed experimentally [55] and canted AF structure was confirmed by magnetic x-ray diffraction [55], magnon dispersion was measured by resonant inelastic x-ray scattering (see Fig. 2.1) [58, 59], and shown indeed to be well described by an antiferromagnetic Heisenberg model including up to third neighbor interactions

$$\mathcal{H} = \sum_{\langle ij \rangle} J_1 \mathbf{j}_i \mathbf{j}_j + \sum_{\langle\langle ij \rangle\rangle} J_2 \mathbf{j}_i \mathbf{j}_j + \sum_{\langle\langle\langle ij \rangle\rangle\rangle} J_3 \mathbf{j}_i \mathbf{j}_j, \tag{2.1}$$

where $\mathbf{j}_i$ is the total j_{eff} momentum on the site i and the first- (second-, third-) neighbor magnetic interactions are taken to be $J_1 = 60$ meV, $J_2 = -20$ meV, $J_3 = 15$ meV to fit the experimental curve for Sr_2IrO_4 [59], [58].

In Fig. 2.1, apart from magnon branch one can clearly see another dispersive feature at higher energies. The energy scale of this excitation coincides with the well-known value of the spin-orbit coupling constant for Sr_2IrO_4 ($\lambda \approx 0.5$ eV) [54], and it was attributed to the intra site excitation of a hole from the lower lying $j_{\text{eff}} = 1/2$ doublet to one of the $j_{\text{eff}} = 3/2$ quartet levels. In the literature such an excitation is often referred to as a *spin-orbit exciton*.

It was pointed out in Ref. [59] that the propagation of such a spin-orbit exciton created in Sr_2IrO_4 during RIXS process can be well described by a corresponding polaronic model. It was demonstrated that the problem of the exciton's hopping process in iridates is formally identical to the problem of hole motion in the AF ordered background of $s = 1/2$ moments: a quasiparticle introduced into the quantum Heisenberg antiferromagnet – be it a hole or a d-d excitation – would create a string of flipped spins as it propagates (see Fig.2.4 (a))

A polaronic model describing propagation of the exciton in AF background can be obtained by projecting the spin-orbit superexchange model (Eq. (1.24)) for Sr_2IrO_4 compound onto the spin-orbit coupled basis (1.36) as we discussed in section 1.4. Instead of considering the lowest doublet only as in Eq. (1.37), one would have to also include the terms describing coupling between $j_{\text{eff}} = 1/2$ doublet and $j_{\text{eff}} = 3/2$ quartet.

Although some of the rigorous calculations briefly sketched above were omitted by the authors of Refs. [59], [58] and simplified perturbation theory approach was used instead, they arrived at the polaronic model of the spin-orbit exciton, where the operator $h^{\dagger}_{\mathbf{k}\alpha}$ from Eq. (1.66) has acquired an index α indicating $j^z_{\text{eff}} = 1/2, 3/2$ character of the $j_{\text{eff}} = 3/2$ spin-orbit exciton. The overall hopping matrix scales as $2t^2/U$, and the bare dispersion of the exciton is renormalized by interaction with magnons just as in the classical t-J model.

As it was mentioned in section 1.3, iridates in general are negative charge transfer systems with large covalency and interactions longer than first neighbor have to be taken into account [2]. Indeed, to achieve a good fit to experiment, authors of Refs. [59], [58] needed to introduce 2nd and 3rd neighbor interactions to the model. As can be seen in Fig. 2.1, the spectral function calculated based on their model gave perfect agreement with the experiment leaving out the small downwards dispersing peak at the Γ point. Thus they confirmed that the exciton dynamics is essentially captured by the effective t-J model and dynamics of the

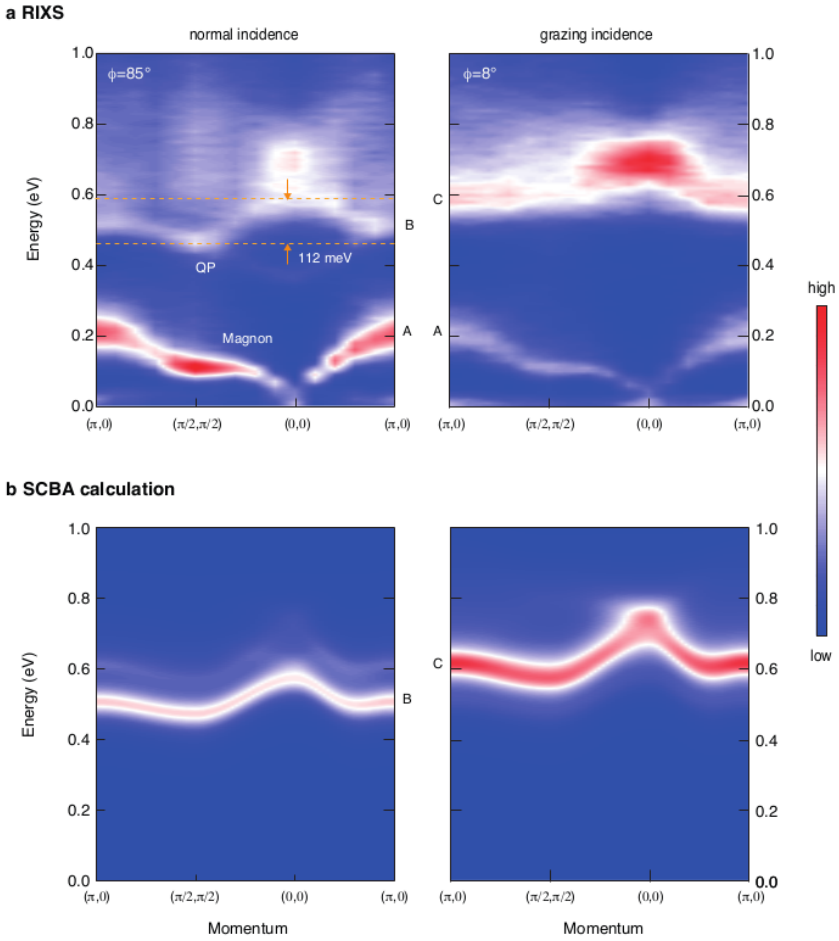

Figure 2.1.: Comparison between (a) RIXS spectra measured along high symmetry lines in normal (left) and grazing (right) geometry and (b) SCBA calculations of the higher energy feature (spin-orbit exciton) reproduced from Ref. [58].

exciton in iridates resembles so remarkably well the dynamics of the hole in cuprates.

In the following we would like to address the nature of the downwards dispersing peak at Γ point unidentified in Ref. [58] (see Fig. 2.1 and also Fig. 4 in Ref. [58] where this peak is much more visible) as well as ask a fundamental question: is a complete ignorance of the orbital-lattice coupling in iridates due the quenching of the orbital momenta for $j_{\text{eff}} = 1/2$ justified? Although similarities between cuprates and iridates were discussed a lot including also in chapter 1, the orbital phenomena which played considerable role in $3d$ compounds were usually omitted from consideration in $5d$ systems since the orbital momentum in the latter is quenched by SOC. In the following section we discuss the orbital phenomena such as electron-phonon coupling in the form of Jahn-Teller interaction applied to Sr_2IrO_4. In particular, we want to show that including Jahn-Teller interaction in the above-described polaronic scheme can naturally explain the presence of the downwards dispersing feature at the Γ point in Fig. 2.1.

2.3. Coupling to the lattice in systems with strong on-site spin-orbit interaction

As described in chapter 1, in square-lattice Sr_2IrO_4 the t_{2g} levels of the $5d$ shell are almost filled, the single hole is subject to both strong SOC and appreciable correlations. The t_{2g} manifold can be described as an effective angular momentum $l_{\text{eff}} = 1$ and SOC locally couples spin $\mathbf{s}$ and $\mathbf{l}$ to the total angular momentum $\mathbf{j}$. The threefold orbital degeneracy of the t_{2g} states is thus lifted by SOC and on-site Hubbard interaction can subsequently open a charge gap and stabilize a localized (pseudo)spin $j_{\text{eff}} = 1/2$ [46, 54]. Due to the orbital part of the $j_{\text{eff}} = 1/2$ wave function, couplings between these effective spins are sensitive to lattice geometry and support a variety of quantum states.

A striking difference to $3d$ systems with negligible [85] SOC is the lifting of the orbital degeneracy: a single hole (or electron) in a $3d$ shell has an orbital degree of freedom in addition to spin – as opposed to the single $j_{\text{eff}} = 1/2$ degree of freedom of the $5d$ hole. Such systems where orbital degeneracy is present then tend to lower their energy by forming long-range orbital pattern. In strong correlated materials such orbital ordering can be driven by exchange or Jahn-Teller interactions, and the latter we would like to discuss in this chapter.

According to Jahn-Teller theorem, any system (except some linear molecules) with a non-Kramers-degenerate electronic ground state is unstable with respect to distortions which lower the symmetry of the configuration. The entire range of effects resulting from orbital ground state degeneracy are referred to as *Jahn-Teller effect*, see [64] for extensive discussion on Jahn-Teller effect in TM compounds. In Fig 2.2(a) three sites of a 2D square-lattice of TM ions each in an octahedral oxygen cage are shown schematically – as one can see, neither of the two orbitals is beneficial for an electron to occupy, the system will therefore seek an opportunity to lower its energy by undergoing a structural deformation which lifts this twofold orbital degeneracy. And this is precisely what is shown in Fig. 2.2(b) – as the lattice has undergone cooperative distortion, the oxygens have been displaced and now one or another orbital is lower in energy on a site with a particular distortion – the system exhibits an orbital ordering.

Of course, for a two-fold degenerate system there exist two distinct ways in which a lattice can accommodate the distortion (see Fig. 2.3), so that the twofold degeneracy in the system is in general preserved but now for the new electronic-vibrational (vibron) states rather than for the electronic ground states. In other words, although the orbital degeneracy is now lifted, the phonon modes associated with the crystal deformation are degenerate too. Depending on the probability of thermal and quantum transitions between the two minima associated with the degenerate vibron states, one distinguishes a dynamic and a static Jahn-Teller effect. The dynamic Jahn-Teller effect takes place if the probability is high and the system fluctuates from

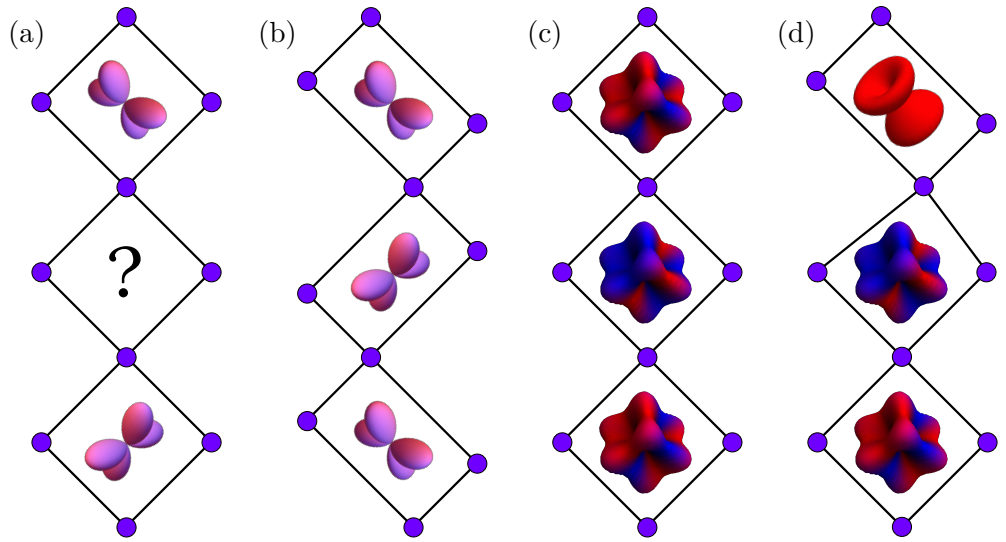

Figure 2.2.: Cartoon picture showing the Jahn-Teller effect in systems *without* and *with* strong SOC: (a) Weak SOC – orbitally degenerate ground state of the system: electrons occupying d_{xz} and d_{yz} orbital have the same energy. (b) Weak SOC – oxygen displacements following "conventional" Jahn-Teller effect for the ground state with e.g. the d_{xz}/d_{yz} alternating orbital order. (c) Strong SOC – no oxygen displacements due to the quenched Jahn-Teller effect for the ground state with e.g. $|j_{\text{eff}} = 1/2,\ j_z = 1/2\rangle/|j_{\text{eff}} = 1/2,\ j_z = -1/2\rangle$ alternating spin-orbital order (antiferromagnetic order of $j_{\text{eff}} = 1/2$ isospins). (d) Strong SOC – oxygen displacements around the $|j_{\text{eff}} = 3/2,\ j_z = -3/2\rangle$ exciton (which 'lives' in the antiferromagnetic $j_{\text{eff}} = 1/2$ ground state) showing that such a system is Jahn-Teller active.

one energy minimum to another, hence remaining on average spherically symmetric. In the static Jahn-Teller effect transitions are happening very slowly, therefore the system remains "frozen" in one of the two states, and the cooperative lattice distortion can be measured with e.g. x-ray diffraction.

So indeed, a $3d$ system can not only feature an orbital order in addition to the magnetism, but Jahn-Teller effect would moreover be expected to couple the orbital degree of freedom to the lattice [49, 64, 81, 82]. In contrast, in $5d$ systems the quenching of the orbital degree of freedom by SOC seemingly removes the possibility of orbital order and would at first sight also appear to suppress the Jahn-Teller effect and coupling to the lattice. In the next section, we are nevertheless going to discuss the impact of Jahn-Teller effect on $5d$ systems with strong SOC: while it is indeed absent for the ground state consisting of $j_{\text{eff}} = 1/2$ pseudospins, see Fig. 2.2(c), we are going to show that it leaves clear signatures in the dynamics of collective *excitations* into the $j_{\text{eff}} = 3/2$ sector (i.e. excitons). As seen in Fig. 2.2(d), the Jahn-Teller effect is here not quenched and can allow for a novel type of excitonic propagation. In particular, we propose that the experimentally observed branch of the exciton dispersion with the minimum at the Γ point [58], which can not be explained using superexchange alone, finds a natural explanation within the present Jahn-Teller model. Since the Jahn-Teller effect discussed here would only take place due to the degeneracy of the excited electronic state it would be of a local character, i.e. it would cause a local distortion of the lattice that supports propagation of the exciton.

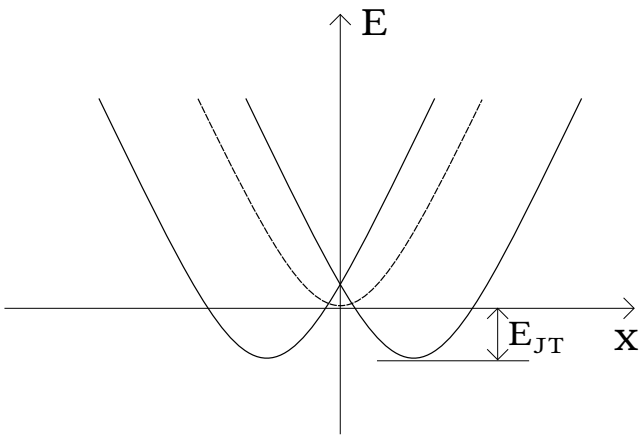

Figure 2.3.: A cartoon picture showing the energy dependence on the lattice deformation x for a twofold degenerate systems. Here E_{JT} indicates the energy lowering due to the Jahn-Teller effect.

2.4. Jahn-Teller assistant propagation of the spin-orbit exciton

Since the SOC constant $\lambda > 0$ is assumed to be the largest energy scale involved, with $\lambda = 0.382$ eV in Sr_2IrO_4 [58], we start our analysis by diagonalizing this dominant term. This is achieved by a basis change from $\mathbf{s}$ (the $s = 1/2$ spin) and $\mathbf{l}$ (the effective $l_{\mathrm{eff}} = 1$ orbital moment) to total angular momentum $\mathbf{j} = \mathbf{l} + \mathbf{s}$. For a single hole in the t_{2g} shell, SOC interaction (1.32) becomes then

$$\mathcal{H}_{\mathrm{SOC}} = \lambda/2 \sum_i (\mathbf{j}_j^2 - \mathbf{s}_j^2 - \mathbf{l}_j^2), \tag{2.2}$$

and the ground state is given by the doubly-degenerate $j_{\mathrm{eff}} = 1/2$ manifold, while the $j_{\mathrm{eff}} = 3/2$ manifold forms the excited states at energy $3\lambda/2$. (A crystal-field splitting Δ can explicitly be included into this analysis [46, 53], but is omitted here for clarity).

For t_{2g} electrons, the orbital operators $\mathbf{l}$ couple both to the tetragonal phonon modes Q_2 and Q_3 (the e_g modes) and to the trigonal phonon modes Q_4, Q_5, and Q_6 (the t_{2g} modes). After integrating out the phonons, the Jahn-Teller interaction is expressed in terms of $\mathbf{l}$ [64]:

$$\begin{aligned}\mathcal{H}_{\mathrm{JT}} = & V \sum_{\langle \mathbf{i},\mathbf{j} \rangle} \left[\left(l_{\mathbf{i}}^z\right)^2 - \frac{2}{3} \right] \left[\left(l_{\mathbf{j}}^z\right)^2 - \frac{2}{3} \right] \\ & + V \sum_{\langle \mathbf{i},\mathbf{j} \rangle} \left[\left(l_{\mathbf{i}}^x\right)^2 - \left(l_{\mathbf{i}}^y\right)^2 \right] \left[\left(l_{\mathbf{j}}^x\right)^2 - \left(l_{\mathbf{j}}^y\right)^2 \right] \\ & + \kappa V \sum_{\langle \mathbf{i},\mathbf{j} \rangle} \left[\left(l_{\mathbf{i}}^x l_{\mathbf{i}}^y + l_{\mathbf{i}}^y l_{\mathbf{i}}^x\right) \left(l_{\mathbf{j}}^x l_{\mathbf{j}}^y + l_{\mathbf{j}}^y l_{\mathbf{j}}^x\right) + \ldots \right]. \end{aligned} \tag{2.3}$$

The two classes of phonon modes lead to two *a priori* independent Jahn-Teller coupling constants $V_{e_g} \equiv V$ and $V_{t_{2g}} \equiv \kappa V$, i.e. V describes the Jahn-Teller interaction due to the coupling to the tetragonal modes, while κV stands for the coupling between the trigonal modes. As $V_{t_{2g}}$ is typically much smaller than V_{e_g}, we set $\kappa = 0.1$. The Jahn-Teller interaction scale V can from experiment [37] be inferred to be non-negligible, but as its strength is at present unclear, we leave it as a free parameter.

The $j_{\mathrm{eff}} = 3/2$ excitation, an exciton, that can be created in resonant inelastic x-ray

scattering is described by the Green's function

$$G(\mathbf{k},\omega) = \mathrm{Tr}\langle 0|\hat{\chi}_{\mathbf{k}} \frac{1}{\omega - H + i\delta} \hat{\chi}^{\dagger}_{\mathbf{k}}|0\rangle, \tag{2.4}$$

where the $\hat{\chi}^{\dagger}_{\mathbf{k}}$ is a vector of four creation operators that create an exciton with momentum $\mathbf{k}$ and isospin quantum number $j_z = \pm 1/2, \pm 3/2$. The Hamiltonian H describes the dynamics of the exciton coupling to a background of $j_{\mathrm{eff}} = 1/2$ isospins, a minimal Hamiltonian is

$$H = H^{\mathrm{mag}}_{\mathrm{SE}} + H^{\mathrm{exc}}_{\mathrm{SE}} + H^{\mathrm{exc}}_{\mathrm{JT}} \ . \tag{2.5}$$

The first term $H^{\mathrm{mag}}_{\mathrm{SE}}$ is the superexchange interaction between $j_{\mathrm{eff}} = 1/2$ isospins, given by Eq. (2.1) where we include up to third-neighbor processes $\propto \{J_1, J_2, J_3\}$ as discussed in sections 2.2 and 2.3. The terms $H^{\mathrm{exc}}_{\mathrm{SE}}$ and $H^{\mathrm{exc}}_{\mathrm{JT}} = \mathcal{H}_{\mathrm{JT}}(3/2, 1/2)$ describe superexchange and Jahn-Teller interaction between one $j_{\mathrm{eff}} = 1/2$ and one $j_{\mathrm{eff}} = 3/2$ site, these terms allow the exciton to move.

Without the Jahn-Teller-mediated motion, i.e. for $H = H^{\mathrm{mag}}_{\mathrm{SE}} + H^{\mathrm{exc}}_{\mathrm{SE}}$, the problem is analogous to the one discussed in Refs. [58, 59] (see section 2.3). Exciton propagation due to superexchange is analogous to the mechanism governing orbital excitations in cuprates [96, 120] and is strongly coupled to the magnonlike $j_{\mathrm{eff}} = 1/2$ excitations. We are going to show here that the Jahn-Teller coupling $\mathcal{H}_{\mathrm{JT}}(3/2, 1/2)$ provides an additional channel for delocalization whose signatures can be clearly distinguished from the pure superexchange scenario.

Following Refs. [58, 59], we extend a scheme that was widely used to describe motion in an antiferromagnetic background (see chapter 1 and [6, 50, 74, 119]) in order to include Jahn-Teller-mediated exciton motion.

2.4.1. Derivation of the model

Firstly, since we are interested here in the effective interaction between the $\mathbf{j} = \mathbf{l}+\mathbf{s}$ spin-orbital angular momenta (as induced by the Jahn-Teller effect), we rewrite the above Jahn-Teller Hamiltonian in the basis spanned by eigenvectors of $\mathbf{j}^2$ and j_z (the $\mathbf{j}$-basis). For this reason, we make a basis transformation from the "$\mathbf{l}\cdot\mathbf{s}$"-basis (with the effective $l_{\mathrm{eff}} = 1$ and $s = 1/2$)

$$\hat{A} = (|yz,\uparrow\rangle, |yz,\downarrow\rangle, |xz,\uparrow\rangle, |xz,\downarrow\rangle, |xy,\uparrow\rangle, |xy,\downarrow\rangle)\,, \tag{2.6}$$

in which the above Jahn-Teller Hamiltonian is written into the $\mathbf{j}$-basis (with the effective $j_{\mathrm{eff}} = 1/2$ or $j_{\mathrm{eff}} = 3/2$ and appropriate j_z quantum numbers)

$$\hat{j} = \left(|\tfrac{1}{2},\tfrac{1}{2}\rangle, |\tfrac{1}{2},\tfrac{-1}{2}\rangle, |\tfrac{3}{2},\tfrac{3}{2}\rangle, |\tfrac{3}{2},\tfrac{1}{2}\rangle, |\tfrac{3}{2},\tfrac{-1}{2}\rangle, |\tfrac{3}{2},\tfrac{-3}{2}\rangle\right). \tag{2.7}$$

using the Clebsch-Gordon coefficients as written in Eq. (1.36). As a result we obtain the Jahn-Teller Hamiltonian which *a priori* consists of three distinct terms:

$$\mathcal{H}_{\mathrm{JT}} = \mathcal{H}_{\mathrm{JT}}(1/2, 1/2) + \mathcal{H}_{\mathrm{JT}}(3/2, 1/2) + \mathcal{H}_{\mathrm{JT}}(3/2, 3/2). \tag{2.8}$$

The first term $\mathcal{H}_{\mathrm{JT}}(1/2, 1/2)$ denotes the Jahn-Teller interaction between two $j_{\mathrm{eff}} = 1/2$ states – it vanishes as expected, reflecting the quenching of orbital physics within the $j_{\mathrm{eff}} = 1/2$ subshell. The last term $\mathcal{H}_{\mathrm{JT}}(3/2, 3/2)$ between two $j_{\mathrm{eff}} = 3/2$ states can only contribute if a large number of $j_{\mathrm{eff}} = 3/2$ states are present and is thus strongly suppressed at large λ. The term $\mathcal{H}_{\mathrm{JT}}(3/2, 1/2)$ describes the interaction between one $j_{\mathrm{eff}} = 1/2$ and one $j_{\mathrm{eff}} = 3/2$ site: Even at strong SOC, this term becomes relevant when an (iso)orbital excitation raises a single hole into a $j_{\mathrm{eff}} = 3/2$ state [58, 59].

$$\mathcal{H}_{\mathrm{JT}}(3/2, 1/2) \equiv \mathcal{H}^{\mathrm{exc}}_{\mathrm{JT}} = \mathcal{H}_1 + \mathcal{H}_2 + \mathcal{H}_3, \tag{2.9}$$

where

$$\mathcal{H}_1 = \frac{2V}{9}\sum_{\langle \mathbf{i},\mathbf{j}\rangle}\left(c^\dagger_{i\uparrow}a_{i\uparrow}a^\dagger_{j\uparrow}c_{j\uparrow} + c^\dagger_{i\downarrow}a_{i\downarrow}a^\dagger_{j\downarrow}c_{j\downarrow} + \text{h.c.}\right)$$
$$- \frac{2V}{9}\sum_{\langle \mathbf{i},\mathbf{j}\rangle}\left(c^\dagger_{i\downarrow}a_{i\downarrow}a^\dagger_{j\uparrow}c_{j\uparrow} + c^\dagger_{i\uparrow}a_{i\uparrow}a^\dagger_{j\downarrow}c_{j\downarrow} + \text{h.c.}\right)$$
$$+ \kappa V\sum_{\langle \mathbf{i},\mathbf{j}\rangle}\left(c^\dagger_{i\uparrow}a_{i\downarrow}a^\dagger_{j\downarrow}c_{j\uparrow} + c^\dagger_{i\downarrow}a_{i\uparrow}a^\dagger_{j\uparrow}c_{j\downarrow} + \text{h.c.}\right), \tag{2.10}$$

$$\mathcal{H}_2 = \frac{\kappa V}{3}\sum_{\langle \mathbf{i},\mathbf{j}\rangle}\left(f^\dagger_{i\uparrow}a_{i\uparrow}a^\dagger_{j\uparrow}f_{j\uparrow} + f^\dagger_{i\downarrow}a_{i\downarrow}a^\dagger_{j\downarrow}f_{j\downarrow} + \text{h.c.}\right)$$
$$+ \frac{2V(1+\kappa)}{3}\sum_{\langle \mathbf{i},\mathbf{j}\rangle}\left(f^\dagger_{i\downarrow}a_{i\uparrow}a^\dagger_{j\uparrow}f_{j\downarrow} + f^\dagger_{i\uparrow}a_{i\downarrow}a^\dagger_{j\downarrow}f_{j\uparrow} + \text{h.c.}\right)$$
$$+ \frac{2V(\kappa-1)}{3}\sum_{\langle \mathbf{i},\mathbf{j}\rangle}\left(f^\dagger_{i\downarrow}a_{i\uparrow}a^\dagger_{j\downarrow}f_{j\uparrow} + f^\dagger_{i\uparrow}a_{i\downarrow}a^\dagger_{j\uparrow}f_{j\downarrow} + \text{h.c.}\right), \tag{2.11}$$

$$\mathcal{H}_3 = -\frac{\kappa V}{\sqrt{3}}\sum_{\langle \mathbf{i},\mathbf{j}\rangle}\left(f^\dagger_{i\uparrow}a_{i\uparrow}a^\dagger_{j\downarrow}c_{j\uparrow} + c^\dagger_{i\uparrow}a_{i\downarrow}a^\dagger_{j\uparrow}f_{j\uparrow} + \text{h.c.}\right)$$
$$- \frac{\kappa V}{\sqrt{3}}\sum_{\langle \mathbf{i},\mathbf{j}\rangle}\left(c^\dagger_{i\downarrow}a_{i\uparrow}a^\dagger_{j\downarrow}f_{j\downarrow} + f^\dagger_{i\downarrow}a_{i\downarrow}a^\dagger_{j\uparrow}c_{j\downarrow} + \text{h.c.}\right). \tag{2.12}$$

Here $a^\dagger_{i\sigma}$ denotes an operator creating a hole on site $\mathbf{i}$ in the doublet carrying effective total momentum $j_{\text{eff}} = 1/2$ and $\sigma \equiv j_z = \pm 1/2$, while $c^\dagger_{i\sigma}$ ($f^\dagger_{i\sigma}$) are operators creating a hole on site $\mathbf{i}$ in the $j_{\text{eff}} = 3/2$ quartet with $\sigma \equiv j_z = \pm 1/2, \pm 1/2$.

Secondly, we map the above Hamiltonian $\mathcal{H}^{exc}_{\text{JT}}$ onto a polaronic model. We follow an algorithm described in section 1.6 and perform the transformations:

(i) Since we assume that the ground state has antiferromagnetic order, we are allowed to rotate all isospins on one of the two antiferromagnetic sublattices:

$$a_{j\sigma} \to a_{j-\sigma} \quad c_{j\sigma} \to c_{j-\sigma} \quad f_{j\sigma} \to f_{j-\sigma}. \tag{2.13}$$

(ii) We introduce the magnon creation $\alpha^\dagger_i$ and spin-orbit exciton creation $\chi^\dagger_{i,\alpha}$ operators (which are bosons and hard-core bosons, respectively). We perform the Holstein-Primakoff transformation and substitute:

$$c^\dagger_{i\uparrow}b_{i\uparrow} \to \chi^\dagger_{i\text{B}}, c^\dagger_{i\downarrow}b_{i\uparrow} \to \chi^\dagger_{i\text{C}}, \tag{2.14}$$
$$c^\dagger_{i\uparrow}b_{i\downarrow} \to \chi^\dagger_{i\text{B}}\alpha_{\mathbf{i}}, c^\dagger_{i\downarrow}b_{i\downarrow} \to \chi^\dagger_{i\text{C}}\alpha_i, \tag{2.15}$$
$$b^\dagger_{i\uparrow}c_{i\uparrow} \to \chi_{i\text{B}}, b^\dagger_{i\uparrow}c_{i\downarrow} \to \chi_{i\text{C}}, \tag{2.16}$$
$$b^\dagger_{i\downarrow}c_{i\uparrow} \to \alpha^\dagger_i\chi_{i\text{B}}, b^\dagger_{i\downarrow}c_{i\downarrow} \to \alpha^\dagger_i\chi_{i\text{C}} \tag{2.17}$$

and

$$f^\dagger_{i\uparrow}b_{i\uparrow} \to \chi^\dagger_{i\text{D}}, f^\dagger_{i\downarrow}b_{i\uparrow} \to \chi^\dagger_{i\text{F}}, \tag{2.18}$$
$$f^\dagger_{i\uparrow}b_{i\downarrow} \to \chi^\dagger_{i\text{D}}\alpha_{\mathbf{i}}, f^\dagger_{i\downarrow}b_{i\downarrow} \to \chi^\dagger_{i\text{F}}\alpha_i, \tag{2.19}$$
$$b^\dagger_{i\uparrow}f_{i\uparrow} \to \chi_{i\text{D}}, b^\dagger_{i\uparrow}f_{i\downarrow} \to \chi_{i\text{F}}, \tag{2.20}$$
$$b^\dagger_{i\downarrow}f_{i\uparrow} \to \alpha^\dagger_i\chi_{i\text{D}}, b^\dagger_{i\downarrow}f_{i\downarrow} \to \alpha^\dagger_i\chi_{i\text{F}}. \tag{2.21}$$

Here B, C, D, F denote $j_z = 1/2$, $j_z = -1/2$, $j_z = 3/2$, $j_z = -3/2$ quantum numbers, respectively.

(iii) We perform the Fourier and Bogolyubov transformations (see e.g. Ref. [74])

$$\begin{aligned} a_{\mathbf{q}} &= u_{\mathbf{q}}\alpha_{\mathbf{q}} - v_{\mathbf{q}}\alpha^{\dagger}_{-\mathbf{q}}, \\ a^{\dagger}_{\text{-}\mathbf{q}} &= u_{\text{-}\mathbf{q}}\alpha^{\dagger}_{\text{-}\mathbf{q}} - v_{\mathbf{q}}\alpha_{\mathbf{q}}, \end{aligned} \tag{2.22}$$

where the magnon energy $\omega_{\mathbf{q}} = \sqrt{A^2_{\mathbf{q}} - B^2_{\mathbf{q}}}$ and Bogolyubov coefficients $u_{\mathbf{q}}$, $v_{\mathbf{q}}$ are given by the usual expressions in the linear spin-wave theory:

$$u_{\mathbf{q}} = \frac{1}{\sqrt{2}}\sqrt{\frac{A_{\mathbf{q}}}{\omega_{\mathbf{q}}} + 1}, v_{\mathbf{q}} = -\frac{\text{sign}(B_{\mathbf{q}})}{\sqrt{2}}\sqrt{\frac{A_{\mathbf{q}}}{\omega_{\mathbf{q}}} - 1}, \tag{2.23}$$

where the coefficients $A_{\mathbf{q}}$ and $B_{\mathbf{q}}$ are defined in a usual way, see e.g. Eq. (8) in the Supplementary Material of Ref. [58]:

$$A_{\mathbf{q}} = 2(J_1 - J_2 - J_3 + J_2\cos q_x \cos q_y) + J_3(\cos 2q_x + \cos 2q_y), \tag{2.24}$$

$$B_{\mathbf{q}} = J_1(\cos q_x + \cos q_y). \tag{2.25}$$

Here we neglected terms comprising two magnon operators, since it was shown that coupling to two magnons does not significantly change the polaronic spectrum (see for example Ref. [6]).

After applying the above transformations to Hamiltonian (2.9) we arrive at the following polaronic Hamiltonian for the propagation of the $j_{\text{eff}} = 3/2$ spin-orbit exciton:

$$H^{\text{exc}}_{\text{JT}} = \sum_{\mathbf{k},\mathbf{q}} [\hat{M}^{\text{JT}}_{\mathbf{k},\mathbf{q}} \hat{\chi}^{\dagger}_{\mathbf{k}} \hat{\chi}_{\mathbf{k}\ -\mathbf{q}} a_{\mathbf{q}} + \text{h.c.}] + \sum_{\mathbf{k}} \hat{E}^{\text{JT}}_{\mathbf{k}} \hat{\chi}^{\dagger}_{\mathbf{k}} \hat{\chi}_{\mathbf{k}} \tag{2.26}$$

with the momentum-dependent vertices

$$\begin{aligned} \hat{M}^{\text{JT}}_{\mathbf{k},\mathbf{q}} &= zV\hat{m}^{\text{JT}} \cdot |\gamma_{\mathbf{k}} v_{\mathbf{q}} + \gamma_{\mathbf{k}-\mathbf{q}} u_{\mathbf{q}}|/\sqrt{N}, \\ \hat{E}^{\text{JT}}_{\mathbf{k}} &= zV\hat{e}^{\text{JT}} \cdot |\gamma_{\mathbf{k}}|, \end{aligned} \tag{2.27}$$

where N is the total number of sites, $z = 4$ is the coordination number for a square lattice, and

$$\gamma_{\mathbf{q}} = \frac{1}{2}\sum_{\mathbf{r}} \cos \mathbf{q} \cdot \mathbf{r} \tag{2.28}$$

and the diagonal (off-diagonal) matrix $\hat{m}^{\text{JT}}$ ($\hat{e}^{\text{JT}}$) describing the polaronic (free) hopping reads

$$\hat{m}^{\text{JT}} = \frac{1}{3}\begin{pmatrix} \frac{1}{3}+\frac{\kappa}{2} & 0 & 0 & 0 \\ 0 & \frac{1}{3}+\frac{\kappa}{2} & 0 & 0 \\ 0 & 0 & 1+\frac{\kappa}{2} & 0 \\ 0 & 0 & 0 & 1+\frac{\kappa}{2} \end{pmatrix} \tag{2.29}$$

$$\tag{2.30}$$

and

$$\hat{e}^{\text{JT}} = \frac{2}{3}\begin{pmatrix} 0 & -\frac{1}{3} & -\frac{\sqrt{3}\kappa}{2} & 0 \\ -\frac{1}{3} & 0 & 0 & -\frac{\sqrt{3}\kappa}{2} \\ -\frac{\sqrt{3}\kappa}{2} & 0 & 0 & -1+\kappa \\ 0 & -\frac{\sqrt{3}\kappa}{2} & -1+\kappa & 0 \end{pmatrix}, \tag{2.31}$$

which act on the row of kets of the excited states

$$X = (|j_z = 1/2\rangle, |j_z = -1/2\rangle, |j_z = 3/2\rangle, |j_z = -3/2\rangle) \tag{2.32}$$

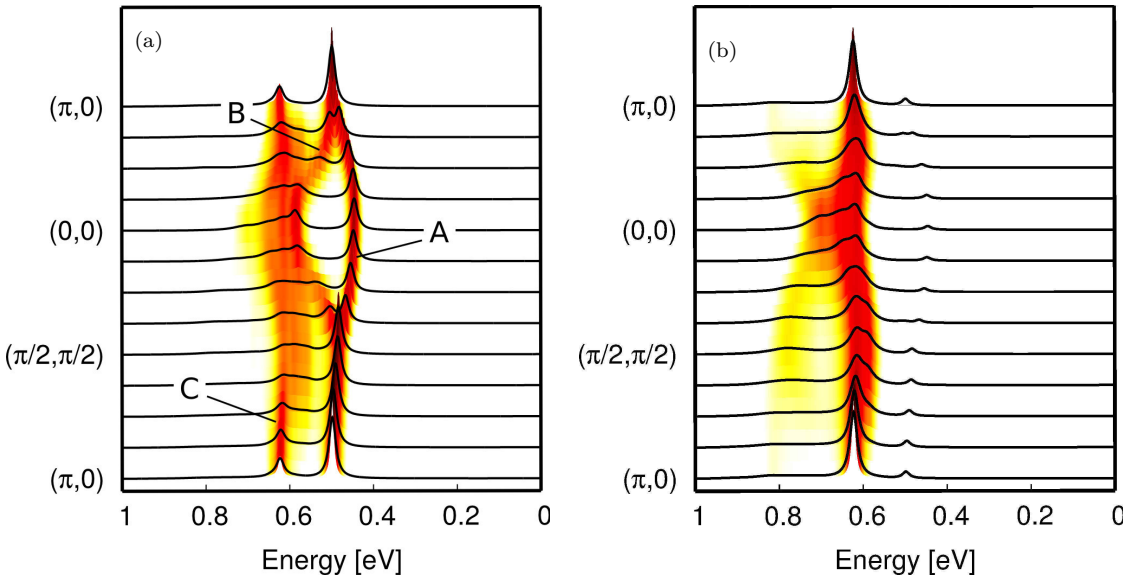

Figure 2.4.: Spin-orbit exciton with both superexchange and Jahn-Teller interaction, see (2.33) - (2.35) calculated using the SCBA. Intensities are given for two RIXS geometries: (a) normal and (b) grazing incidence [58]. 'A', 'B', 'C' in panel (a) denote three main features of the spectrum. Jahn-Teller interaction $V = 0.8\,J_1$ and broadening $\delta = 0.05\,J_1$. Superexchange parameters $J_2 = -0.33\,J_1$, $J_3 = 0.25\,J_1$, $W_1 = 0.5\,J_1$ [58], and $W_2 = W_3 = 0$. Following Ref. [58], the on-site energy of the exciton is $10J_1 \approx \frac{3}{2}\lambda$, crystal-field splitting between $|j_z| = 1/2$ and $|j_z| = 3/2$ states is $2.29\,J_1$, and $J_1 = 0.06$ eV.

with $j_{\text{eff}} = 3/2$.

Then Hamiltonian (2.5) would comprise

$$H_{\text{SE}}^{\text{mag}} = \sum_{\mathbf{k}} \omega_{\mathbf{k}} a_{\mathbf{k}}^{\dagger} a_{\mathbf{k}}, \tag{2.33}$$

$$H_{\text{SE}}^{\text{exc}} + H_{\text{JT}}^{\text{exc}} = \sum_{\mathbf{k}} (\hat{E}_{\mathbf{k}}^{\text{SE}} + \hat{E}_{\mathbf{k}}^{\text{JT}}) \hat{\chi}_{\mathbf{k}}^{\dagger} \hat{\chi}_{\mathbf{k}} \tag{2.34}$$

$$+ \sum_{\mathbf{k},\mathbf{q}} \left[(\hat{M}_{\mathbf{k},\mathbf{q}}^{\text{SE}} + \hat{M}_{\mathbf{k},\mathbf{q}}^{\text{JT}}) \hat{\chi}_{\mathbf{k}}^{\dagger} \hat{\chi}_{\mathbf{k}-\mathbf{q}} a_{\mathbf{q}} + \text{h.c.} \right]. \tag{2.35}$$

Equation (2.33) describes the isospin 'magnons' originating from $H_{\text{SE}}^{\text{mag}}$ (see section 1.6 for detailed derivation), $a_{\mathbf{k}}^{\dagger}$ creates a magnon with momentum $\mathbf{k}$ and energy $\omega_{\mathbf{k}}$. A free exciton hopping is included in Eq. (2.34), it can either be due to second- and third-neighbor superexchange [58], or originate from coupling to the lattice. It will actually turn out that the crucial new feature will come from the free dispersion $\hat{E}_{\mathbf{k}}^{\text{JT}}$, where the Jahn-Teller effect induces a nearest-neighbor contribution absent from superexchange. Finally, Eq. (2.35) captures the coupling between exciton hopping and the isospin background: Both Jahn-Teller effect and superexchange can allow the exciton to exchange place with a nearest-neighbor isospin without flipping said isospin. This creates 'faults' in the alternating order, see Fig. 2.6(a), and thus creates or annihilates magnons.

2.4.2. Manifestation of SE and JT interactions in the excitonic spectral function

We evaluate the Green's function Eq. (2.4) using the self-consistent Born approximation (see section 1.6 for detailed discussion of the method). The excitonic spectral functions are

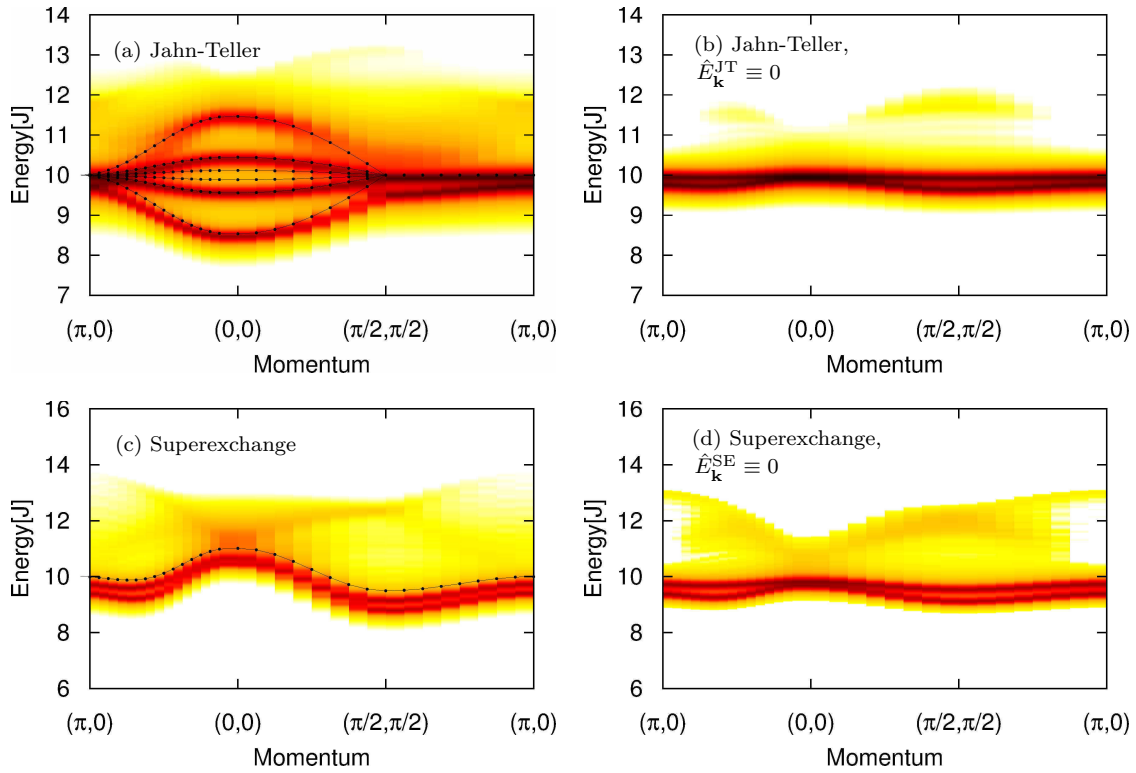

Figure 2.5.: Spin-orbit exciton spectra with propagation driven by either superexchange *or* Jahn-Teller interaction [calculated using SCBA, see text]: (a) Jahn-Teller only, (b) Jahn-Teller only *and* setting $\hat{E}^{\mathrm{JT}}_{\mathbf{k}} \equiv 0$, (c) superexchange only, (d) superexchange only *and* setting $\hat{E}^{\mathrm{SE}}_{\mathbf{k}} \equiv 0$. For clarity, parameters are chosen slightly different from those used in Fig. 2.4: $J_2 = -0.33\,J_1$, $J_3 = 0.25\,J_1$, $W_1 = 0.5\,J_1$, $W_2 = W_3 = 0.13\,J_1$ [58], Jahn-Teller interaction $V = J_1$ and broadening $\delta = 0.05\,J_1$. Spectra are offset by the exciton energy of $10J_1 \approx \frac{3}{2}\lambda$. Dotted lines in (a) and (c) follow the free dispersion relations given by $\hat{E}^{\mathrm{JT}}_{\mathbf{k}}$ and $\hat{E}^{\mathrm{SE}}_{\mathbf{k}}$, respectively.

calculated numerically for a 32×32 cluster, taking into account 'matrix elements' depending on the angle of the incident beam [58], and shown in Fig. 2.4. The most striking difference to the pure superexchange scenario becomes visible in the so-called 'normal' RIXS geometry [cf. Fig. 2.4(a)]: a dispersive feature at around 0.4 eV (denoted as A in the figure) that has its minimal energy at $\mathbf{k} = (0, 0)$ and disperses upward towards the zone boundary, where it merges with the B feature.

Similar unexplained feature with a minimum at the Γ point was observed in normal-incidence RIXS experiments on Sr_2IrO_4 [58], albeit with a weaker intensity. This discrepancy may be due to (i) contributions to the RIXS intensity of the exciton beyond the one determined in the fast core-hole approximation [4, 48] or (ii) the SCBA over-emphasizing the quasiparticle spectral weight [58]. Some fine-tuning of the unknown constant V is needed to reproduce the experimental dispersion, especially the merging with the B feature, see the appendix A for details. It is here worth noting that a similar peak was also seen in Na_2IrO_3 [36], where it does not merge with the higher-energy features, suggesting that the merging may be a detail specific to Sr_2IrO_4. In contrast and as discussed below, the minimum at the Γ point is a robust and characteristic feature of Jahn-Teller-mediated propagation, because superexchange-driven peaks invariably have a *maximum* at the Γ point.

Figure 2.5 illustrates the qualitative difference between Jahn-Teller and superexchange

mediated exciton propagation, with panels (a) and (c) showing the purely Jahn-Teller ($H_{\mathrm{SE}}^{\mathrm{exc}} \equiv 0$) and purely superexchange ($H_{\mathrm{JT}}^{\mathrm{exc}} \equiv 0$) scenarios. A striking difference is that the two quasi-particlelike branches of the superexchange case (c) become four in the Jahn-Teller case (a) – one of which has indeed a minimum at the Γ point. We continue the analysis by noting that both mechanisms allow in principle for a 'free' dispersion without disturbing the alternating isospin order, see Eq. (2.34), as well as for a 'polaronic' propagation involving magnons, see Eq. (2.35). Panels (b) and (d) include only the latter and reveal that the two mechanisms are then almost indistinguishable. This points to a dominant role for isospin fluctuations (on the scale of J in both scenarios) in the 'polaronic' part of exciton motion.

This brings us to the following question: is the difference between the free dispersion relation in the superexchange and in the Jahn-Teller generic or it is just a matter of fine-tuning of the parameters? It turns out that the difference between these two dispersion relations is of fundamental nature. The crucial aspect concerns the nearest-neighbor process, which is therefore depicted for superexchange and Jahn-Teller effect in Fig. 2.6. In superexchange, the exciton propagates by exchanging place with an isospin while both conserve their 'spin', i.e. their j_z quantum number. In an alternating isospin order, where nearest neighbors are always of opposite j_z, this necessarily creates or removes 'defects', see Fig. 2.6(a), and thus magnons. The Jahn-Teller effect, in contrast, allows the exciton and the isospin to flip their quantum numbers while exchanging places and this allows for the nearest neighbor hopping of an exciton without creating magnons, i.e., a free excitonic dispersion. The origin of the difference is that the hole hopping driving superexchange conserves the j_z quantum number, while the lattice-mediated Jahn-Teller effect is insensitive to the orbital phase. This allows j_z to change during Jahn-Teller-driven propagation and accordingly yields four quasi-particles rather than two.

2.5. Conclusions

To summarize, we have analyzed the impact of a lattice-mediated Jahn-Teller effect in the presence of strong SOC, which quenches the orbital degeneracy in the ground state. We found that the Jahn-Teller effect remains present for excited states, and in particular allows for a free nearest-neighbor hopping of the spin-orbit exciton without producing defects in the alternating $j_{\mathrm{eff}} = 1/2$ ordering of the ground state. The tell-tale spectral signature is a dispersion with a minimum at the Γ point, which was observed in experiment but cannot be explained with superexchange alone [58].

Experiments on Sr_2IrO_4 at higher temperatures moreover reveal an active orbital degree of freedom and its coupling to the lattice [37], corroborating the relevance of Jahn-Teller physics when going beyond the ground state.

We have found spin-orbit coupling to substantially affect the interplay of Jahn-Teller effect and superexchange. In $3d$ compounds with weak spin-orbit coupling and unquenched orbital degeneracy (e.g. in manganites [32, 33]) both act on the same microscopic degree of freedom (i.e. orbitals) and in general lead to similar signatures.

In the strongly spin-orbit-coupled $5d$ case, however, Jahn-Teller effect (determined purely by the orbital) and superexchange (strongly affected by spin-orbit entanglement) address different microscopic degrees of freedom. Their interplay is thus far more intricate, as is coupling between ions with and without strong spin-orbit coupling [13].

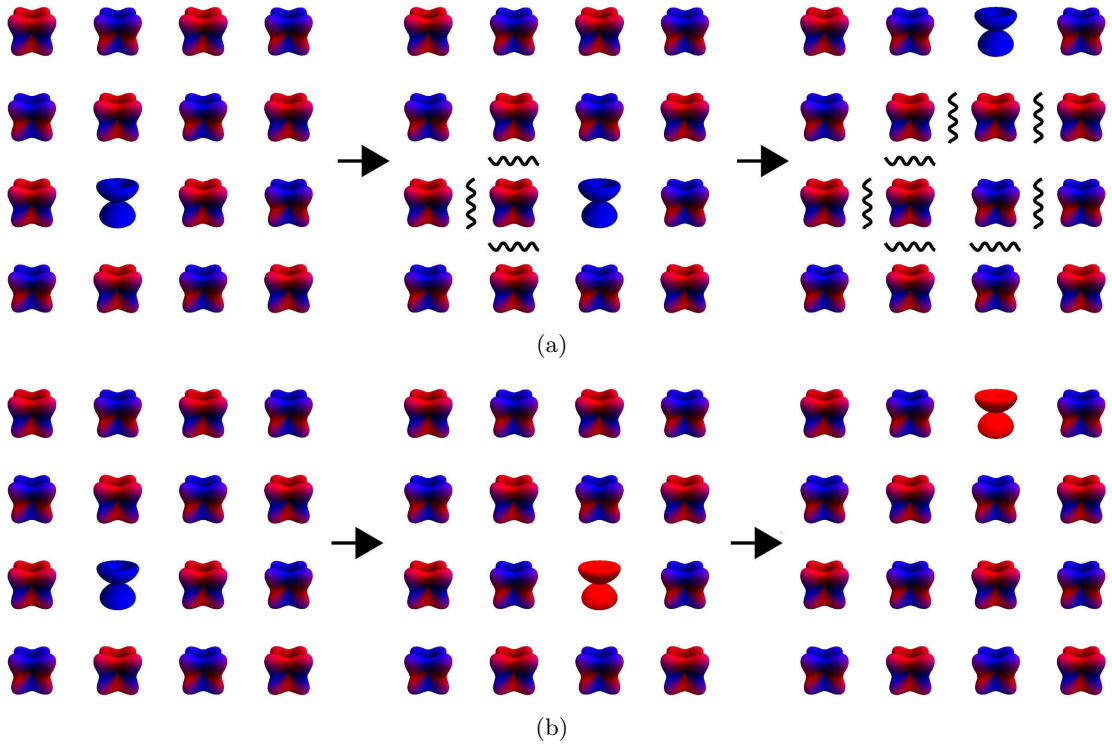

Figure 2.6.: Cartoon showing the two types of nearest neighbor hopping of a $j_{\text{eff}} = 3/2$ exciton in the antiferromagnetically-ordered background: (a) Polaronic hopping (due to Jahn-Teller effect *or* superexchange): a $j_{\text{eff}} = 3/2$ exciton with the $j_z = -3/2$ quantum number (left panel) does not change its j_z quantum number during the hopping process to the nearest neighbor sites (middle and right panels) and thus the $j_{\text{eff}} = 1/2$ magnons are created at each step of the excitonic hopping (wiggle lines on middle and right panels). (b) Free hopping (solely due to Jahn-Teller effect): a $j_{\text{eff}} = 3/2$ exciton with the $j_z = -3/2$ quantum number (left panel) hops to the nearest neighbor site and acquires $j_z = 3/2$ quantum number (middle panel). Note that in this case the $j_{\text{eff}} = 1/2$ magnons are *not* created in the system (middle and right panels).

CHAPTER 3

Correlation induced electron-hole asymmetry in quasi-2D iridates

and its manifestation in (inverse-)photoemission spectra

3.1. Preface

The resemblance of crystallographic and magnetic structures of the quasi-two-dimensional iridates Ba_2IrO_4 and Sr_2IrO_4 to La_2CuO_4 points at an analogy to cuprate high-T_c superconductors, even if spin-orbit coupling is very strong in iridates. The first step towards understanding the physics of the doped compound is to study the motion of a single charge carrier introduced to the compound. Here we examine the analogy between cuprates and iridates for the motion of an elementary charge (hole or electron) added to the antiferromagnetic ground state. First we give a short overview of current progress in the search for possible high-temperature superconductivity in iridates and discuss the motivation behind this work in section 3.2. Then in section 3.3 we derive the low-energy effective model for a single charge carrier doped into the ground state of Sr_2IrO_4, discussing the case of an electron in section 3.3.1 and a hole in section 3.3.3. As pointed out in section 1.4, hopping elements entering such a low-energy model are orbital- and direction-dependent and can be defined from either symmetric considerations (see section 1.4) or from *ab*-initio calculations. In section 3.3.2 we discuss how the the dispersion calculated within a tight-binding model with corresponding hopping integrals is fitted to the band structure calculated within DFT.

In section 3.3 we show that correlation effects render the hole and electron case in iridates very different. An added electron forms a spin-polaron, similar to the cuprates, but the situation of a removed electron is far more complex, since in this case many-body $5d^4$ configurations form. They can then be in a singlet or triplet state depending on the total angular momentum which strongly affects the hole motion. In section 3.4 we show how the theoretical spectra are calculated using models developed in section 3.3 and then in section 3.5 we discuss the ramifications of the hole and electron asymmetry for the interpretation of (inverse-)photoemission experiments. At the end of the chapter we will highlight main conclusions in section 3.6.

Part of this chapter is published as E. M. Pärschke, K. Wohlfeld, K. Foyevtsova and J. van den Brink, "Correlation induced electron-hole asymmetry in quasi-two-dimensional iridates", in: *Nat. Commun.* **8** (686 2017)

3.2. Introduction

It is a well-known fact that the quasi-two-dimensional copper oxides turn into non-BCS superconductors when a sufficient amount of extra charge is introduced into their Mott insulating ground state [44]. Based on the similarities between cuprates and iridates (discussed in detail in chapter 1) it is natural to ask the question [111] whether the quasi-two-dimensional iridates can also become superconducting upon charge doping. On the experimental side, very recently signatures of Fermi arcs and the pseudogap physics were found in the electron- and hole-doped iridates [16, 60, 61, 124] on top of the *d*-wave gap in the electron-doped iridate [61]. On the theoretical side, this requires studying a doped multiorbital two-dimensional Hubbard model supplemented by the non-negligible spin-orbit coupling [17, 39, 76, 112, 115–117]. The latter is a difficult task, since even a far simpler version of this correlated model (the one-band Hubbard model) is not easily solvable on large, thermodynamically relevant, clusters [73].

Fortunately, there exists one nontrivial limit of the two-dimensional doped Hubbardlike problems, whose solution can be obtained in a relatively exact manner. It is the so-called single-hole problem which relates to the motion of a single charge (hole or doublon) added to the AF and insulating ground state of the undoped two-dimensional Hubbardlike model [50, 97]. In the strong coupling limit at half-filling this problem reduces down to solving a *t*-*J* model which was discussed in detail in chapter 1 and in particular in sections 1.6 – 1.7. In the case of the cuprates, this problem has been intensively studied both on the theoretical as well as the experimental side and its solution (the formation of the spin polaron) is considered

a first step in understanding the motion of doped charge in the two-dimensional Hubbard model [6, 27, 74, 114].

In the case of iridates, several recent angle-resolved photoemission spectroscopy experiments unveiled the shape of the iridate spectral functions [12, 16, 54, 61, 69, 83, 109, 113, 123]. However, on the theoretical side this correlated electron problem has not been investigated using the above approach [16, 54, 57, 117] – although it was suggested that the combination of local density approximation of density-functional theory and dynamical mean field theory (LDA+DMFT) or even LDA+U band structure description might be sufficient [12, 54, 80, 83, 109, 128]. We will compare results presented in this thesis to that obtained with (LDA+DMFT) in Ref. [128] in section 3.5.

In the following we calculate the spectral function of the correlated strong coupling model describing the motion of a single charge doped into the AF and insulating ground state of the quasi-two-dimensional iridate, using the self-consistent Born approximation (SCBA) which is well suited to the problem [11, 70, 74, 98, 107, 114]. The main result is that we find a fundamental difference between the motion of a single electron or hole added to the undoped iridate. Whereas the single electron added to the Ir^{4+} ion locally forms a $5d^6$ configuration, adding a hole (i.e. removing an electron) to the Ir^{4+} ion leads to the $5d^4$ configuration. (Let me note here that in what follows we assume that the iridium oxides are in the Mott-Hubbard regime, since the on-site Hubbard U on iridium is smaller than the iridium-oxygen charge transfer gap [17, 51, 78]). Due to the strong on-site Coulomb repulsion, these differences in the local ionic physics have tremendous consequences for the propagation of the doped electrons and holes. In particular, in the electron case the lack of internal degrees of freedom of the added charge, forming a $5d^6$ configuration, makes the problem qualitatively similar to the above-discussed problem of the quasi-two-dimensional cuprates and to the formation of the spin polaron. On the contrary, the hopping of a hole to the nearest neighbor site does not necessarily lead to the coupling to the magnetic excitations from $j = 1/2$ AF, which is a result of the fact that the $5d^4$ configuration may have a nonzero total angular momentum J [18]. As discussed in the following, this result has important consequences for our understanding of recent and future experiments on the quasi-two-dimensional iridates.

3.3. Effective low-energy model of the square-lattice iridates

We begin with the low-energy description of the quasi-two-dimensional iridates. In the ionic picture (i.e. taking into account in an appropriate ionic Hamiltonain the cubic crystal field splitting [79], the spin-orbit coupling [46], and the on-site Coulomb interaction [18]) the strong on-site spin-orbit coupling λ splits the iridium ion t_{2g} levels into the $j = 1/2$ lower energy doublet (see Fig. 3.1) and the $j = 3/2$ higher energy quartet, where j is the isospin (total angular momentum) of the only hole in the $5d^5$ iridium shell [46, 54, 58, 111]. For the bulk, the strong on-site Hubbard repulsion between holes on iridium ions needs to be taken into account which leads to the localization of the iridium holes and the AF interaction between their $j = 1/2$ isospins in the two-dimensional iridium plane [46]. Consequently, this Mott insulating ground state possesses two-dimensional AF long range order with the low-energy excitations well described in the linear spin-wave approximation [56]

$$\mathcal{H}_{\mathrm{mag}} = \sum_{\mathbf{q}} \omega_{\mathbf{q}} (\alpha^{\dagger}_{\mathbf{q}} \alpha_{\mathbf{q}} + \beta^{\dagger}_{\mathbf{q}} \beta_{\mathbf{q}}), \tag{3.1}$$

where $\mathbf{q}$ is the crystal momentum and $\omega_{\mathbf{q}}$ is the dispersion of the (iso)magnons $|\alpha_{\mathbf{q}}\rangle$ and $|\beta_{\mathbf{q}}\rangle$:

$$\omega_{\mathbf{q}} = \sqrt{A^2_{\mathbf{q}} - B^2_{\mathbf{q}}} \tag{3.2}$$

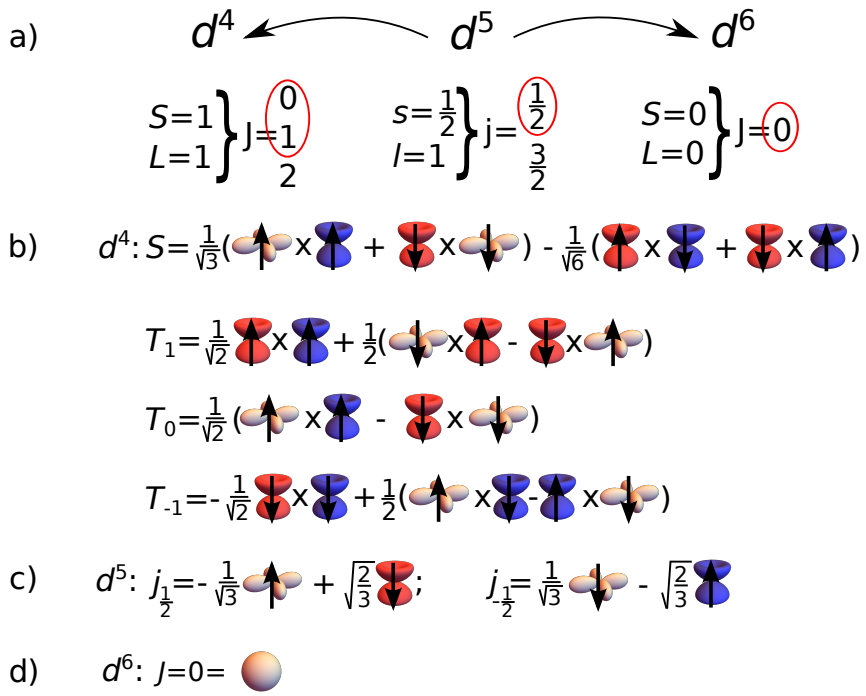

Figure 3.1.: Low-energy eigenstates of iridium ions. (a) Quantum numbers characterising certain electronic configuration, where j, l, and s (J, L, and S) stands for single-particle (multi-particle) total, orbital, and spin angular momentum. The red circles indicate the states that are explicitly taken into account in our effective low-energy theory. (b) Eigenstates for the $5d^4$ configuration (relevant for the $5d^4$ hole case) of the appropriate ionic Hamiltonian of iridium ion. (c) Same as (b) but for the $5d^5$ configuration (as relevant for the quasi-two-dimensional iridate ground state). (d) Same as (b) but for the $5d^6$ configuration (relevant for $5d^6$ doublon case). Blue, red and beige cartoon orbitals indicate the one-particle states with the effective angular momentum $l = 1$ and $l^z = 1$, $l^z = -1$ and $l^z = 0$ respectively. Round beige cartoon orbital indicates full shell with $L = 0$. Up (down) black arrows indicate $s^z = 1/2$ ($s^z = 1/2$) of spin $s = 1/2$ states. No arrow on an orbital indicates $S = 0$ state.

with

$$A_{\mathbf{q}} = 2(J_1 - J_2 + J_2 \cos q_x \cos q_y - J_3(1 - \frac{1}{2}(\cos 2q_x + \cos 2q_y))), \tag{3.3}$$

$$B_{\mathbf{q}} = J_1(\cos q_x + \cos q_y). \tag{3.4}$$

Here J_1, J_2 and J_3 are the nearest, next nearest and third neighbor isospin exchange interactions, respectively.

The parameters of the Bogoliubov transformation, the so-called Bogoliubov coefficients $u_{\mathbf{q}}$, $v_{\mathbf{q}}$, are given by the following expressions:

$$\begin{aligned} u_{\mathbf{q}} &= \frac{1}{\sqrt{2}}\sqrt{\frac{A_{\mathbf{q}}}{\omega_{\mathbf{q}}} + 1}, \\ v_{\mathbf{q}} &= -\frac{\mathrm{sign}(B_{\mathbf{q}})}{\sqrt{2}}\sqrt{\frac{A_{\mathbf{q}}}{\omega_{\mathbf{q}}} - 1} \end{aligned} \tag{3.5}$$

see also section 1.6 where derivation of eq. (3.1) (although for one type of magnons) is described in greater detail.

We note here that, although the size of the experimentally observed optical gap is not large (around 500 meV [78]), it is still more than twice larger than the top of the magnon band in the resonant inelastic x-ray scattering spectra (around 200 meV) [58, 59]. This, together with the fact that the linear spin wave theory very well describes the experimental RIXS spectra of the quasi-two-dimensional iridates [58, 59], justifies using the strong coupling approach.

3.3.1. Motion of electron in the ground state of Sr_2IrO_4: IPES

Introducing a single electron into the quasi-two-dimensional iridates, as experimentally realized in an inverse photoemission (IPES) experiment, leads to the creation of a single $5d^6$ doublon in the bulk, leaving the nominal $5d^5$ configuration on all other iridium sites. Since the t_{2g} shell is for the $5d^6$ configuration completely filled, the only eigenstate of the appropriate ionic Hamiltonian is the one carrying $J = 0$ total angular momentum. Therefore, just as in the cuprates, the $5d^6$ doublon formed in IPES has no internal degrees of freedom, i.e. $|d\rangle \equiv |J = 0\rangle$, see Fig. 3.1.

Turning on the hybridization between iridium ions leads to the hopping of the $5d^6$ doublon between iridium sites $\mathbf{i}$ and $\mathbf{j}$: $|5d^5_{\mathbf{i}}5d^6_{\mathbf{j}}\rangle\langle 5d^6_{\mathbf{i}}5d^5_{\mathbf{j}}|$. To derive the Hamiltonian which would describe the motion of the $5d^6$ doublon added to the Mott insulating ground state formed by the $5d^5$ iridium ions of the (undoped) square-lattice iridates due to the nonzero hopping elements we need to calculate the following matrix elements of the tight-binding Hamiltonian describing the hybridization between iridium sites $\langle 5d^6_{\mathbf{i}}5d^5_{\mathbf{j}}|\mathcal{H}_{\mathrm{TB}}|5d^5_{\mathbf{i}}5d^6_{\mathbf{j}}\rangle$. The exact form of the tight-binding Hamiltonian depends on the fine details of the structure like distortions and is given in details in section 3.3.2. It is important to realise at this point that, although such hopping is restricted to the lowest Hubbard subband of the problem, it may change the AF configuration and excite magnons. In fact, magnons are excited during all nearest neighbor hopping processes, since the kinetic energy conserves the total angular momentum.

Firstly, we calculate the above matrix elements in the appropriate eigenstates of ionic Hamiltonian of the $5d^5$ and $5d^6$ configurations (these states are listed in Fig. 3.1). We note that these matrix elements do not explicitly depend on the strong on-site spin-orbit coupling λ, though the form of the appropriate eigenstates of the ionic Hamiltonian (Fig. 1 of the main text) is of course due to the onset of strong on-site spin-orbit coupling λ. Secondly, we assume the so-called no double occupancy constraint, which follows from the implicitly assumed here limit of strong on-site Coulomb repulsion – which prohibits the creation of unnecessary $5d^6$ doublons once the electron added to the quasi-two-dimensional iridate $5d^5$ ground state hops between sites. Technically this amounts to the introduction of the projection operator which takes care of this constraint. Finally, following the path described for example in Refs. [74, 90] and introducing the slave-fermion formalism followed by Fourier and Bogoliubov transformations, we arrive at the following polaronic Hamiltonian which describes the motion of the $5d^6$ doublon:

$$\mathcal{H}_{\mathrm{IPES}} = \mathcal{H}_{\mathrm{mag}} + \mathcal{H}^{\mathbf{d}}_{\mathrm{t}}, \tag{3.6}$$

where $\mathcal{H}_{\mathrm{mag}}$ is defined above and the hopping of the single $5d^6$ doublon in the bulk follows from the spin-polaronic [6, 50, 74, 119] Hamiltonian

$$\mathcal{H}^{\mathbf{d}}_{\mathrm{t}} = \sum_{\mathbf{k}} V^0_{\mathbf{k}} \left(d^\dagger_{\mathbf{k}\mathrm{A}} d_{\mathbf{k}\mathrm{A}} + d^\dagger_{\mathbf{k}\mathrm{B}} d_{\mathbf{k}\mathrm{B}} \right) + \sum_{\mathbf{k},\mathbf{q}} V_{\mathbf{k},\mathbf{q}} \left(d^\dagger_{\mathbf{k}\text{-}\mathbf{q}\mathrm{B}} d_{\mathbf{k}\mathrm{A}} \alpha^\dagger_{\mathbf{q}} + d^\dagger_{\mathbf{k}\text{-}\mathbf{q}\mathrm{A}} d_{\mathbf{k}\mathrm{B}} \beta^\dagger_{\mathbf{q}} + \mathrm{h.c.} \right), \tag{3.7}$$

where A, B are two AF sublattices, the term $V^0_{\mathbf{k}}$ describes the next nearest and third neighbor hopping which does not excite magnons (free hopping), and the term $V_{\mathbf{k},\mathbf{q}}$ describes the nearest neighbor coupling between the $5d^6$ doublon and the magnons as a result of the nearest neighbor electronic hopping (polaronic hopping, see above). We note that the exact expressions for V's depend on the five hopping elements of the minimal tight binding model:

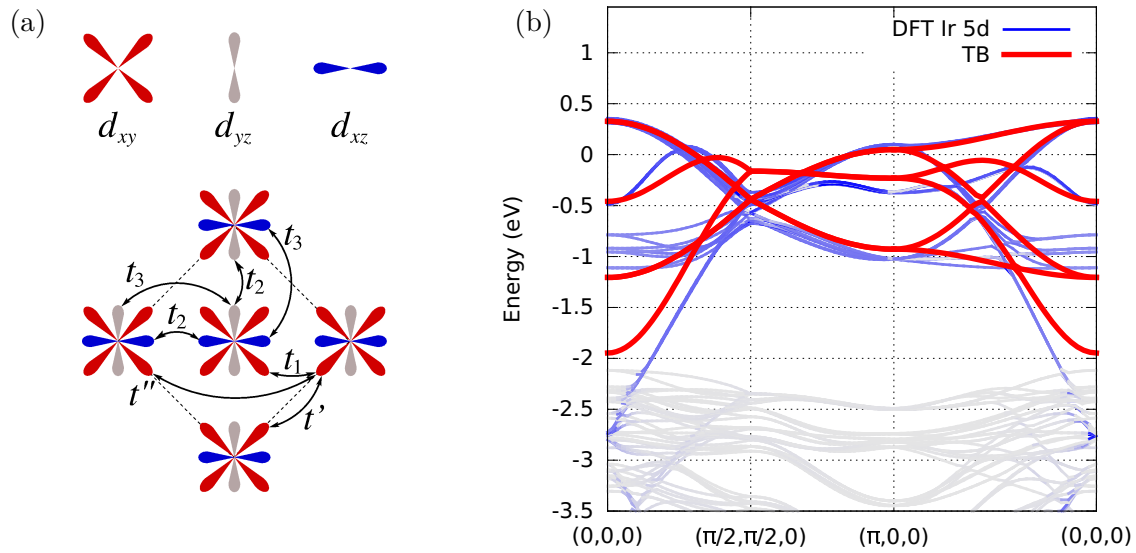

Figure 3.2.: Tight-binding model. (a) A cartoon illustrating the t_1, t_2, t_3, t' and t'' hopping paths between the Ir-5d-t$_{2g}$ orbitals taken into account in the tight-binding model. (b) Comparison between the density functional theory (DFT) band structure as calculated for Sr_2IrO_4 (blue and grey lines) and the tight-binding (TB) model written in the Ir-5d-t$_{2g}$ orbital basis (red lines). The intensity of the blue shade of the DFT bands represents the amount of the Ir-5d-t$_{2g}$ character in a given band at a particular momentum (darkest blue – largest overlap with the Ir-5d-t$_{2g}$ orbitals; grey – lowest overlap with the Ir-5d-t$_{2g}$ orbitals). The Fermi energy is set to zero. Figure courtesy by K. Foyevtsova [86].

t_1 (t', t'') describing nearest (next-nearest, third-) neighbor hopping between the d_{xy} orbitals in the xy plane, t_2 – the nearest neighbor in-plane hopping between the other two active orbitals, $d_{xz}(d_{yz})$, along the $x(y)$ direction, and t_3 – the nearest neighbor hopping between d_{xz} (d_{yz}) orbitals along the $y(x)$ direction.

3.3.2. Determining the tight-binding Hamiltonian from the DFT calculations

The values of the parameters ($t_1 = -0.2239$ eV, $t_2 = -0.373$ eV, $t' = -0.1154$ eV, $t'' = -0.0595$ eV, $t_3 = -0.0592$ eV) in the tight-binding Hamiltonian are found as a best fit of this restricted tight-binding model to the LDA band structure. The TB model band structure based on the parameter values is shown in red in Fig. 3.2 (b).

The electronic band structure of Sr_2IrO_4 was calculated using DFT in the local density approximation [87] and within the linearized augmented plane wave approach using the WIEN2k code [9] by K. Foyevtsova [86]. The 10 K crystal structure of Sr_2IrO_4 was considered, with the space group $I41/acd$, as reported in Ref. [43]. The calculated band structure of Sr_2IrO_4 is shown in Fig. 3.2 (a) along a path in the Brillouin zone of the $I41/acd$ unit cell. The bands with the predominant Ir-5d-t$_{2g}$ character are highlighted in blue.

Then the calculated dispersion of the Ir-5d-t$_{2g}$ bands were used to parameterized the

tight-binding (TB) model

$$\mathcal{H}_{\rm TB} = -t_1 \sum_{\langle \mathbf{i},\mathbf{j}\rangle||\hat{x},\hat{y},\sigma} c^\dagger_{\mathbf{i}\sigma} c_{\mathbf{j}\sigma} - t_2 \sum_{\langle \mathbf{i},\mathbf{j}\rangle||\hat{y},\sigma} a^\dagger_{\mathbf{i}\sigma} a_{\mathbf{j}\sigma} - t_2 \sum_{\langle \mathbf{i},\mathbf{j}\rangle||\hat{x},\sigma} b^\dagger_{\mathbf{i}\sigma} b_{\mathbf{j}\sigma} - t_3 \sum_{\langle \mathbf{i},\mathbf{j}\rangle||\hat{y},\sigma} b^\dagger_{\mathbf{i}\sigma} b_{\mathbf{j}\sigma}$$
$$- t_3 \sum_{\langle \mathbf{i},\mathbf{j}\rangle||\hat{x},\sigma} a^\dagger_{\mathbf{i}\sigma} a_{\mathbf{j}\sigma} - t' \sum_{\langle\langle \mathbf{i},\mathbf{j}\rangle\rangle||\hat{x}',\hat{y}',\sigma} c^\dagger_{\mathbf{i}\sigma} c_{\mathbf{j}\sigma} - t'' \sum_{\langle\langle\langle \mathbf{i},\mathbf{j}\rangle\rangle\rangle||\hat{x}'',\hat{y}'',\sigma} c^\dagger_{\mathbf{i}\sigma} c_{\mathbf{j}\sigma} + \text{h.c.}, \qquad (3.8)$$

where $a^\dagger$, $b^\dagger$, and $c^\dagger$ operator create an electron in the d_{yz}, d_{xz}, d_{xy} orbitals (respectively) with spin $\sigma = \pm\frac{1}{2}$, $\hat{x}$ and $\hat{y}$ indicate the directions of the nearest neighbor bonds in the xy plane of the quasi-two-dimensional iridate, and $\hat{x}' = \hat{x} - \hat{y}$ and $\hat{y}' = \hat{x} + \hat{y}$ ($\hat{x}'' = 2\hat{x}$ and $\hat{y}' = 2\hat{y}$) indicate the directions of the next nearest (third) neighbor bonds in the xy plane of the quasi-two-dimensional iridate. The TB model includes the nearest neighbor hopping integrals t_1, t_2 and t_3 as well as the next nearest and third neighbor integral t' and t'' between the Ir-5d-t_{2g} orbitals, with their meaning explained in Fig. 3.2 (a). Let us note that the generic structure of the TB Hamiltonian follows from the well-known symmetries of an effective TB Hamiltonian for the transition metal oxide with the t_{2g} orbital degrees of freedom: the electrons located in the d_{ab} orbital can solely hop in the ab plane. While in what follows we use the above set of tight-binding parameters in the polaronic model, we stress that the final results are not critically sensitive to this particular choice of the model parameters. The obtained PES / IPES spectra are quite robust w.r.t. small changes in the TB parameters: in particular, as long as the TB parameters provide a relatively good fit to the LDA spectra, they lead to the SCBA spectra with all of the reported features.

3.3.3. Motion of a hole in the ground state of Sr_2IrO_4: ARPES

Next, following similar logic we derive the microscopic model for a single hole introduced into the iridate, which resembles the case encountered in the photoemission (PES) experiment. In this case a single $5d^4$ hole is created in the bulk. Due to the strong Hund's coupling the lowest eigenstate of the appropriate ionic Hamiltonian for four t_{2g} electrons has the total (effective) orbital momentum $L = 1$ and the total spin momentum $S = 1$ [52]. Moreover, in the strong spin-orbit coupled regime the $L = 1$ and $S = 1$ moments the eigenstates of such an ionic Hamiltonian are the lowest lying $J = 0$ singlet S, and the higher lying $J = 1$ triplets T_σ ($\sigma = -1, 0, 1$, split by energy λ from the singlet state) and $J = 2$ quintets. For a detailed discussion of the multiplet structure of $5d^4$ configuration see chapter 5. Since the high energy quintets are only marginally relevant to the low-energy description in strong on-site spin-orbit coupling λ [58] limit, one obtains [18] that, unlike e.g. in the cuprates, the $5d^4$ hole formed in PES is effectively left with four internal degrees of freedom, i.e. $|\mathbf{h}\rangle \equiv \{|S\rangle, |T_1\rangle, |T_0\rangle, |T_{-1}\rangle\}$, see Fig. 3.1.

Once the hybridization between the iridium ions is turned on, the hopping of the $5d^4$ hole between iridium sites $\mathbf{i}$ and $\mathbf{j}$ is possible: $|5d^5_{\mathbf{i}} 5d^4_{\mathbf{j}}\rangle\langle 5d^4_{\mathbf{i}} 5d^5_{\mathbf{j}}| = |5d^5_{\mathbf{i}}\rangle\langle 5d^5_{\mathbf{j}}||\mathbf{h}_{\mathbf{j}}\rangle\langle\mathbf{h}_{\mathbf{i}}|$. Similarly to the IPES case described above, in principle such hopping of the $5d^4$ hole may or may not couple to magnons. However, there is one crucial difference w.r.t. IPES: the $5d^4$ hole can carry finite angular momentum and thus the $5d^4$ doublon may move between the nearest neighbor sites without coupling to magnons. Altogether, the PES Hamiltonian reads

$$\mathcal{H}_{\rm PES} = \mathcal{H}_{\rm mag} + \mathcal{H}_{\rm SOC} + \mathcal{H}^{\mathbf{h}}_{\rm t}, \qquad (3.9)$$

where

$$\mathcal{H}_{\rm SOC} = \lambda \sum_{\mathbf{k},\sigma=-1,0,1} T^\dagger_{\mathbf{k}\sigma} T_{\mathbf{k}\sigma} \qquad (3.10)$$

describes the on-site energy of the triplet states $\lambda = \xi/2$ where $\xi = 0.382$ [58] is a one particle on-site spin-orbit coupling and the hopping of the single $5d^4$ hole in the bulk is described by

the following spin-polaronic [50, 74, 97] Hamiltonian

$$\mathcal{H}_{\mathrm{t}}^{\mathbf{h}} = \sum_{\mathbf{k}} \left(\mathbf{h}_{\mathbf{k}\mathrm{A}}^{\dagger} \hat{V}_{\mathbf{k}}^{0} \mathbf{h}_{\mathbf{k}\mathrm{A}} + \mathbf{h}_{\mathbf{k}\mathrm{B}}^{\dagger} \hat{V}_{\mathbf{k}}^{0} \mathbf{h}_{\mathbf{k}\mathrm{B}} \right) + \sum_{\mathbf{k},\mathbf{q}} \left(\mathbf{h}_{\mathbf{k}\text{-}\mathbf{q}\mathrm{B}}^{\dagger} \hat{V}_{\mathbf{k},\mathbf{q}}^{\alpha} \mathbf{h}_{\mathbf{k}\mathrm{B}} \alpha_{\mathbf{q}}^{\dagger} + \mathbf{h}_{\mathbf{k}\text{-}\mathbf{q}\mathrm{A}}^{\dagger} \hat{V}_{\mathbf{k},\mathbf{q}}^{\beta} \mathbf{h}_{\mathbf{k}\mathrm{B}} \beta_{\mathbf{q}}^{\dagger} + \mathrm{h.c.} \right) \tag{3.11}$$

where (as above) A, B are two AF sublattices, the term $\hat{V}_{\mathbf{k}}^{0}$ describes the nearest, next nearest, and third neighbor free hopping, and the terms $\hat{V}_{\mathbf{k},\mathbf{q}}^{\alpha}$ and $\hat{V}_{\mathbf{k},\mathbf{q}}^{\beta}$ describe the polaronic hopping.

The free hopping matrix is

$$\hat{V}_{\mathbf{k}}^{0} = \begin{pmatrix} F_1 & 0 & -F_2 & 0 & 0 & P_2 & 0 & -P_1 \\ 0 & F_4 & 0 & 0 & P_1 & 0 & Q_1 & 0 \\ -F_2 & 0 & F_3 & 0 & 0 & Q_2 & 0 & Q_1 \\ 0 & 0 & 0 & 0 & -P_2 & 0 & Q_2 & 0 \\ 0 & P_1 & 0 & -P_2 & F_1 & 0 & F_2 & 0 \\ P_2 & 0 & Q_2 & 0 & 0 & 0 & 0 & 0 \\ 0 & Q_1 & 0 & Q_2 & F_2 & 0 & F_3 & 0 \\ -P_1 & 0 & Q_1 & 0 & 0 & 0 & 0 & F_4 \end{pmatrix}, \tag{3.12}$$

while the matrices containing vertices are

$$\hat{V}_{\mathbf{k},\mathbf{q}}^{\alpha} = \begin{pmatrix} 0 & L_3 & 0 & -L_3 & Y_1 & 0 & -W_2 & 0 \\ L_3 & 0 & L_1 & 0 & 0 & Y_4 & 0 & W_1 \\ 0 & L_1 & 0 & L_1 & -W_2 & 0 & Y_2 & 0 \\ -L_3 & 0 & L_1 & 0 & 0 & W_1 & 0 & Y_3 \\ 0 & 0 & 0 & 0 & 0 & L_4 & 0 & -L_4 \\ 0 & 0 & 0 & 0 & L_4 & 0 & L_2 & 0 \\ 0 & 0 & 0 & 0 & 0 & L_2 & 0 & L_2 \\ 0 & 0 & 0 & 0 & -L_4 & 0 & L_2 & 0 \end{pmatrix}, \tag{3.13}$$

$$\hat{V}_{\mathbf{k},\mathbf{q}}^{\beta} = \begin{pmatrix} 0 & L_4 & 0 & -L_4 & 0 & 0 & 0 & 0 \\ L_4 & 0 & L_2 & 0 & 0 & 0 & 0 & 0 \\ 0 & L_2 & 0 & L_2 & 0 & 0 & 0 & 0 \\ -L_4 & 0 & L_2 & 0 & 0 & 0 & 0 & 0 \\ Y_1 & 0 & W_2 & 0 & 0 & L_3 & 0 & -L_3 \\ 0 & Y_3 & 0 & W_1 & L_3 & 0 & L_1 & 0 \\ W_2 & 0 & Y_2 & 0 & 0 & L_1 & 0 & L_1 \\ 0 & W_1 & 0 & Y_4 & -L_3 & 0 & L_1 & 0 \end{pmatrix}, \tag{3.14}$$

The nearest neighbor free hopping $P(\mathbf{k})$, $Q(\mathbf{k})$ and the polaronic diagonal $Y(\mathbf{k},\mathbf{q})$ and

non-diagonal $W(\mathbf{k},\mathbf{q})$ vertex elements are

$$P_1(\mathbf{k}) = \frac{2\,(2t_1 - t_2)}{3\sqrt{3}}\gamma_{\mathbf{k}} - \frac{2t_3}{3\sqrt{3}}\gamma_{\mathbf{k}}, \tag{3.15}$$

$$P_2(\mathbf{k}) = \frac{2t_2}{\sqrt{3}}\tilde{\gamma}_{\mathbf{k}} - \frac{2t_3}{\sqrt{3}}\tilde{\gamma}_{\mathbf{k}}, \tag{3.16}$$

$$Q_1(\mathbf{k}) = \frac{(4t_1 + t_2)}{3\sqrt{2}}\gamma_{\mathbf{k}} + \frac{t_3}{3\sqrt{2}}\gamma_{\mathbf{k}}, \tag{3.17}$$

$$Q_2(\mathbf{k}) = \frac{t_2}{\sqrt{2}}\tilde{\gamma}_{\mathbf{k}} - \frac{t_3}{\sqrt{2}}\tilde{\gamma}_{\mathbf{k}}, \tag{3.18}$$

$$W_1(\mathbf{k},\mathbf{q}) = \frac{t_3 - t_2}{\sqrt{2N}}\left(\tilde{\gamma}_{\mathbf{k-q}}u_{\mathbf{q}} + \tilde{\gamma}_{\mathbf{k}}v_{\mathbf{q}}\right), \tag{3.19}$$

$$W_2(\mathbf{k},\mathbf{q}) = -\frac{4\,(2t_1 - t_2 - t_3)}{3\sqrt{3N}}\left(\gamma_{\mathbf{k-q}}u_{\mathbf{q}} - \gamma_{\mathbf{k}}v_{\mathbf{q}}\right), \tag{3.20}$$

$$Y_1(\mathbf{k},\mathbf{q}) = -\frac{16\,(t_1 + t_2 + t_3)}{9\sqrt{2N}}\left(\gamma_{\mathbf{k-q}}u_{\mathbf{q}} + \gamma_{\mathbf{k}}v_{\mathbf{q}}\right), \tag{3.21}$$

$$Y_2(\mathbf{k},\mathbf{q}) = -\frac{2\,(4t_1 + t_2 + t_3)}{3\sqrt{2N}}\left(\gamma_{\mathbf{k-q}}u_{\mathbf{q}} + \gamma_{\mathbf{k}}v_{\mathbf{q}}\right), \tag{3.22}$$

$$Y_3(\mathbf{k},\mathbf{q}) = -\frac{4t_1 + t_2 + t_3}{3\sqrt{2N}}\gamma_{\mathbf{k}}v_{\mathbf{q}} - \frac{3\,(t_2 + t_3)}{\sqrt{2N}}\gamma_{\mathbf{k-q}}u_{\mathbf{q}}, \tag{3.23}$$

$$Y_4(\mathbf{k},\mathbf{q}) = -\frac{4t_1 + t_2 + t_3}{3\sqrt{2N}}\gamma_{\mathbf{k-q}}u_{\mathbf{q}} - \frac{3\,(t_2 + t_3)}{\sqrt{2N}}\gamma_{\mathbf{k}}v_{\mathbf{q}}, \tag{3.24}$$

with $\tilde{\gamma}_{\mathbf{k}} = 1/2(\cos k_x - \cos k_y)$;

The free hopping elements arising from the next-nearest and third neighbor hoppings

$$F_1(\mathbf{k}) = -\frac{4t'\gamma'_{\mathbf{k}}}{9} - \frac{4t''\gamma''_{\mathbf{k}}}{9}, \tag{3.25}$$

$$F_2(\mathbf{k}) = -\frac{8t'\gamma'_{\mathbf{k}}}{3\sqrt{6}} - \frac{8t''\gamma''_{\mathbf{k}}}{3\sqrt{6}}, \tag{3.26}$$

$$F_3(\mathbf{k}) = -\frac{2t'\gamma'_{\mathbf{k}}}{3} - \frac{2t''\gamma''_{\mathbf{k}}}{3}, \tag{3.27}$$

$$F_4(\mathbf{k}) = -\frac{t'\gamma'_{\mathbf{k}}}{3} - \frac{t''\gamma''_{\mathbf{k}}}{3}; \tag{3.28}$$

The polaronic next-nearest and third neighbor hopping elements

$$L_1(\mathbf{k},\mathbf{q}) = \frac{4t'}{3\sqrt{N}}\gamma'_{\mathbf{k-q}}u_{\mathbf{q}} + \frac{4t''}{3\sqrt{N}}\gamma''_{\mathbf{k-q}}u_{\mathbf{q}}, \tag{3.29}$$

$$L_2(\mathbf{k},\mathbf{q}) = \frac{4t'}{3\sqrt{N}}\gamma'_{\mathbf{k}}v_{\mathbf{q}} + \frac{4t''}{3\sqrt{N}}\gamma''_{\mathbf{k}}v_{\mathbf{q}}, \tag{3.30}$$

$$L_3(\mathbf{k},\mathbf{q}) = \frac{8t'}{3\sqrt{6N}}\gamma'_{\mathbf{k-q}}u_{\mathbf{q}} + \frac{8t''}{3\sqrt{6N}}\gamma''_{\mathbf{k-q}}u_{\mathbf{q}}, \tag{3.31}$$

$$L_4(\mathbf{k},\mathbf{q}) = \frac{8t'}{3\sqrt{6N}}\gamma'_{\mathbf{k}}v_{\mathbf{q}} + \frac{8t''}{3\sqrt{6N}}\gamma''_{\mathbf{k}}v_{\mathbf{q}}. \tag{3.32}$$

We stress that while $\hat{V}$'s again depend on the the five hopping parameters, their form is far more complex than in the case of an added electron.

3.4. Theoretical (inverse-)photoemission spectra

Using the SCBA method [70, 74, 98, 107, 114], which was discussed in section 1.7, we calculate the relevant Green's functions for the single electron ($5d^6$ doublon, $|d\rangle$) doped into the AF

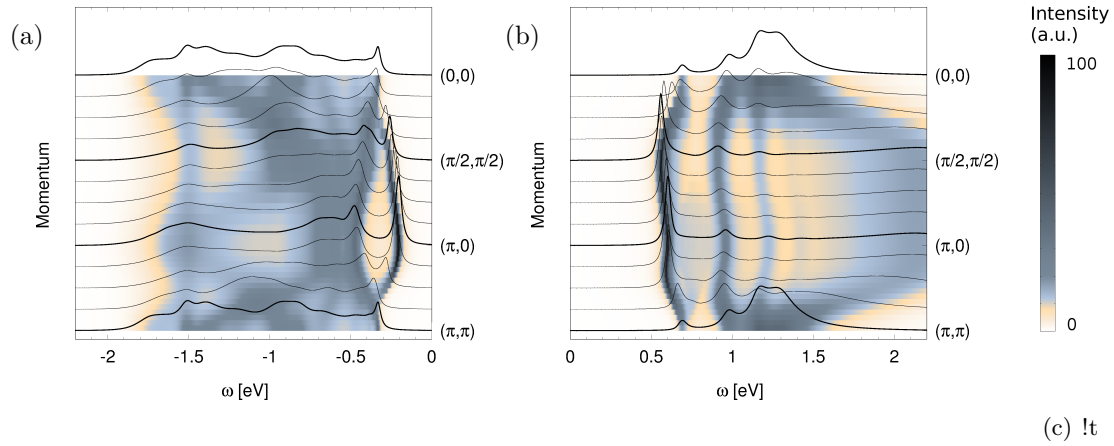

Figure 3.3.: Theoretical spectral functions of iridates: (a) photoemission (PES) and (b) inverse photoemission (IPES) spectral function of the low-energy (polaronic) models developed for the square-lattice iridates and solved using the self-consistent Born approximation. Following parameters are used: spin exchange $J_1 = 0.06\,\mathrm{eV}$, $J_2 = -0.02\,\mathrm{eV}$, $J_2 = 0.015\,\mathrm{eV}$, and spin-orbit coupling $\xi = 0.382\,\mathrm{eV}$ following Ref. [58]; hopping integrals calculated as the best fit to the density functional theory (DFT) band structure as discussed in section 3.3.2: $t_1 = -0.2239\,\mathrm{eV}$, $t_2 = -0.373\,\mathrm{eV}$, $t' = -0.1154\,\mathrm{eV}$, $t_3 = -0.0592\,\mathrm{eV}$, $t'' = -0.0595\,\mathrm{eV}$; spectra offset by (a) $E = -0.77$ eV and (b) $E = -1.47$ eV; broadening $\delta = 0.01$ eV.

ground state of the quasi-two-dimensional iridates

$$G_{\mathrm{IPES}}(\mathbf{k},\omega) = \langle \mathrm{AF}|d_{\mathbf{k}}\frac{1}{\omega - \mathcal{H}_{\mathrm{IPES}} + i\delta}d^{\dagger}_{\mathbf{k}}|\mathrm{AF}\rangle, \tag{3.33}$$

and the single hole ($5d^4$ hole, $|\mathbf{h}\rangle$) doped into the AF ground state of the quasi-two-dimensional iridates

$$G_{\mathrm{PES}}(\mathbf{k},\omega) = \mathrm{Tr}\langle \mathrm{AF}|\mathbf{h}_{\mathbf{k}}\frac{1}{\omega - \mathcal{H}_{\mathrm{PES}} + i\delta}\mathbf{h}^{\dagger}_{\mathbf{k}}|\mathrm{AF}\rangle. \tag{3.34}$$

We note that using the SCBA method to treat the spin-polaronic problems is well-established and that the non-crossing approximation is well-justified [70, 98, 107]. We solve the SCBA equations on a finite lattice of 16×16 sites and calculate the imaginary parts of the above Green's functions – which (qualitatively) correspond to the theoretical IPES and PES spectral functions.

We first discuss the calculated angle-resolved IPES spectral function shown in Fig. 3.3(b). One can see that the first addition state has a quasiparticle character, though its dispersion is relatively small (compared to the LDA bands, see section 3.3.2): there is a rather shallow minimum at $(\pi/2, \pi/2)$ and a maximum at the Γ point. Moreover, a large part of the spectral weight is transferred from the quasiparticle to the higher lying ladder spectrum, due to the rather small ratio of the spin exchange constants and the electronic hopping [74]. Altogether, these are all well-known signatures of the spin-polaron physics: the mobile defect in an AF is strongly coupled to magnons (leading to the ladder spectrum) and can move coherently as a quasiparticle only on the scale of the spin exchange J_1 [50, 74, 97]. Thus, it is not striking that the calculated IPES spectrum of the iridates is similar to the PES spectrum of the t-J model with a negative next nearest neighbor hopping – the model case of the hole-doped cuprates [6, 27, 98, 114]. This agrees with a more general conjecture, previously reported in

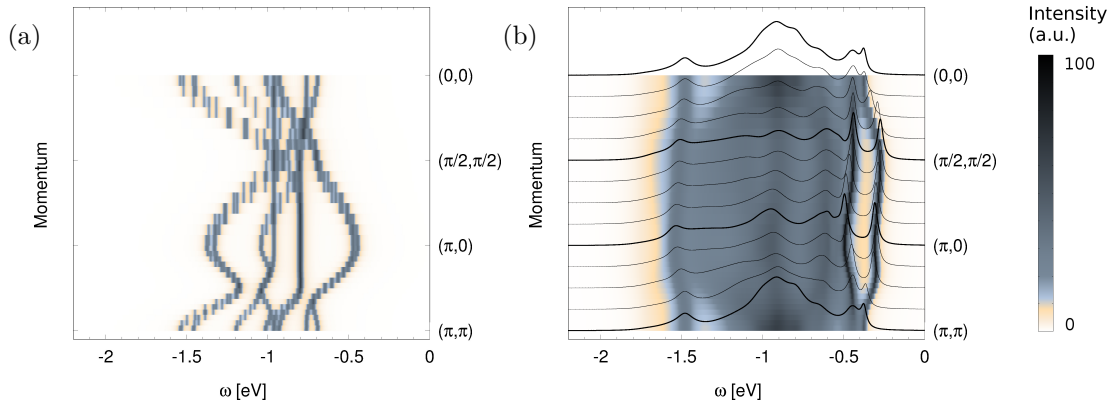

Figure 3.4.: Free and polaronic contributions to the spectrum: (a) Theoretical photoemission spectral function with only propagation of the hole not coupled to magnons allowed as achieved by setting $\hat{V}^{\alpha}_{\mathbf{k}} = \hat{V}^{\beta}_{\mathbf{k}} \equiv 0$. (b) Theoretical photoemission spectral function with only polaronic propagation via coupling to magnons allowed (i.e. no free dispersion) as achieved by setting $\hat{V}^{0}_{\mathbf{k}} \equiv 0$. Parameters as in Fig. 3.3.

the literature: the correspondence between the physics of the hole-doped cuprates and the electron-doped iridates [111].

Due to the internal spin and orbital angular momentum degrees of freedom of the $5d^4$ states, the angle-resolved PES spectrum of the iridates [Fig. 3.3(a)] is very different. The first removal state shows a quasiparticle character with a relatively small dispersion and a minimum is at the $(\pi, 0)$ point (so that we obtain an indirect gap for the quasi-two-dimensional iridates). On a qualitative level this quasiparticle dispersion resembles the situation found in the PES spectrum of the t-J model with a positive next nearest neighbor hopping [114], which should model the electron-doped cuprates (or IPES on the undoped). However, the higher energy part of the PES spectrum of the iridates is quite distinct not only w.r.t. the IPES but also the PES spectrum of the t-J model with the positive next nearest neighbor hopping [6, 27, 114]. Thus, the spin-polaron physics, as we know it from the cuprate studies [50, 74, 97], is modified in this case and we find only very partial agreement with the paradigm stating that the electron-doped cuprates and the hole-doped iridates show similar physics [111].

The above result follows from the interplay between the free [Fig. 3.4(a)] and polaronic hoppings [Fig. 3.4(b)] (we note that typically such interplay is highly nontrivial and the resulting full spectrum is never a simple superposition of these two types of hopping processes, cf. Refs. [6, 25, 30, 90, 114, 121]). The free hopping of the $5d^4$ hole is possible here for both the $J = 0$ singlet and $J = 1$ triplets which leads to the onset of several bands. As already stated, the $J = 1$ triplets can freely hop not only to the next nearest neighbors but also to the nearest neighbors (see above). For the polaronic hopping, the appearance of several polaronic channels, originating in the free J-bands being dressed by the $j = 1/2$ magnons, contributes to the strong quantitative differences w.r.t. the $5d^6$ doublon case or the cuprates.

3.5. Comparison to the experiment

To directly compare our results with the experimental ARPES spectra of Sr_2IrO_4 [54, 61, 83, 109], we plot the zoomed-in spectra for PES, see Fig. 3.5. Clearly, we find that the first electron removal state is at a deep minimum at $(\pi, 0)$, in good agreement with experiment. This locus coincides with the k-point where the final state $J = 0$ singlet has maximum spectral weight, see Fig. 3.5(b). Also the plateau around $(\pi/2, \pi/2)$ and the shallow minimum of the

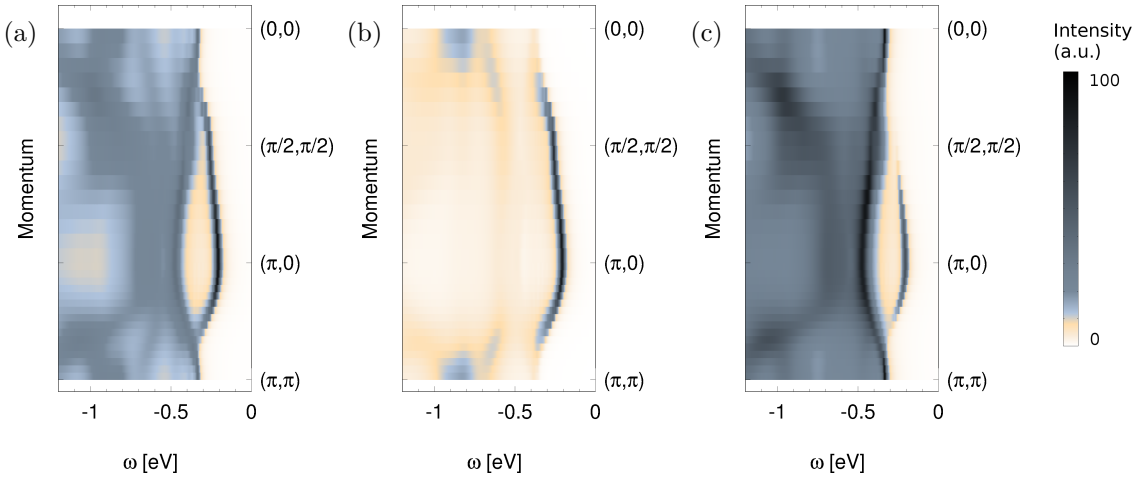

Figure 3.5.: A zoom-in into the photoemission spectrum: (a) a zoom-in into the complete theoretical photoemission spectral function of Fig. 3.4(a), (b, c) same as panel (a) but J-resolved – with (b) showing the $J = 0$ contribution (motion of a "singlet hole") and (c) the $J = 1$ contribution (motion of a "triplet hole").

dispersion at the Γ point are reproduced, where the latter is related to a strong back-bending of higher energy $J = 1$ triplets, see Fig. 3.5(c). Thus one observes that the motion of the $5d^4$ hole with the singlet character is mostly visible around the minimum at $(\pi, 0)$ and near the plateau at $(\pi/2, \pi/2)$ [Fig. 3.5(b)], whereas the triplet is mostly visible at the Γ points and much less at $(\pi, 0)$ [Fig. 3.5(c)]. The higher energy features in the PES spectrum are mostly of triplet character, due to the difference in the on-site energies between the singlet and triplets λ. These features, however, may in case of real materials be strongly affected by the onset of the oxygen states in the PES spectrum (not included in this study, see above).

Experimentally, electron doping causes Fermi-arcs to appear in Sr_2IrO_4 that are centered around $(\pi/2, \pi/2)$ [16, 60, 61, 124], which indeed corresponds the momentum at which our calculations place the lowest energy d^6 electron addition state. On the basis of the calculated electron-hole asymmetry one expects that for hole-doping such Fermi arcs must instead be centered around $(\pi, 0)$, unless of course such doping disrupts the underlying host electronic structure of Sr_2IrO_4.

Finally, it shall be noted that although the iridate spectral function calculated using LDA+DMFT is also in good agreement with the experimental ARPES spectrum [128], there are two well-visible spectral features that are observed experimentally, and seem to be better reproduced by the t-J model based approach: the experimentally observed maximum at Γ point in ARPES being 150-250 meV lower than the maximum at the X point [12, 16, 54, 61, 69, 83, 109, 123], and the more incoherent spectral weight just below the quasiparticle peak around the Γ point than around the M point. We believe that the better agreement with the experiment of the spin polaronic approach than of the DMFT is due to the momentum independence of the DMFT self-energy – which means that the latter method is not able to fully capture the spin-polaron physics [74, 105]. It is known that the self-energy of the quaiparticle in the spin-polaron problem is in general momentum-dependent [74]. Similarly, in the spin-polaronic problem applicable to the iridates studied here, the self-energy is also explicitely momentum dependent, as illustrated in Fig. 3.6. Particularly strong momentum dependence is observed near Γ point where the most prominent differences to LDA+DMFT indeed take place.

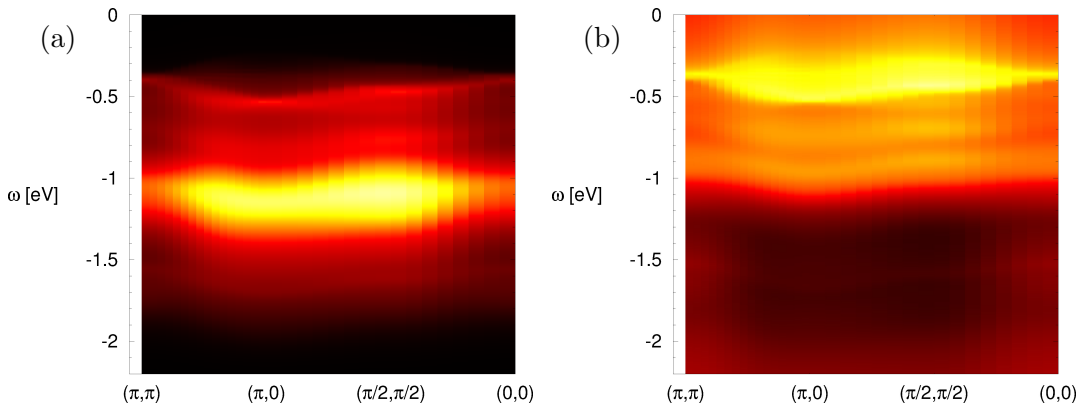

Figure 3.6.: The momentum dependence of imaginary (a) and real (b) part of the self-energy $\mathbf{\Sigma}(\mathbf{k}, \omega)$ calculated for the Green's function in Eq. (3.34) using Dyson's equation [72]. Here brighter color indicate higher intensity.

3.6. Conclusions

The differences between the motion of the added hole and electron in the quasi-two-dimensional iridates have crucial consequences for our understanding of these compounds. The PES spectrum of the undoped quasi-two-dimensional iridates should be interpreted as showing the $J = 0$ and $J = 1$ bands dressed by $j = 1/2$ magnons and a free nearest and further neighbor dispersion.

The IPES spectrum, on the other hand, consists solely of a $J = 0$ band dressed by $j = 1/2$ magnons and a free next nearest and third neighbor dispersion. Thus, whereas the IPES spectrum of the quasi-two-dimensional iridates qualitatively resemble the PES spectrum of the cuprates, this is not the case of the iridate PES.

This result suggests that, unlike in the case of the cuprates, the differences between the electron and hole doped quasi-two-dimensional iridates cannot be modelled by a mere change of sign in the next nearest hopping in the respective Hubbard or t-J model. Any realistic model of the hole doped iridates should instead include the onset of $J = 0$ and $J = 1$ quasiparticle states upon hole doping.

CHAPTER 4

Spin-polaron ladder spectrum of Sr_2IrO_4 probed by scanning tunneling spectroscopy

4.1. Preface

We have shown in chapter 3 that the extended t-J model accounting for a realistic set of hopping parameters and the on-site many-body multiplet structure successfully explains the recent ARPES experiments on Sr_2IrO_4 including small details of the spectra like lowering of the maximum at Γ point or spectral weight transfer to the incoherent part of the spectrum. As pointed out in section 1.6, such a realistic polaronic approach can explain many of the experiments on strongly correlated materials where some sort of charge excitation is created. In the photoemission process a charge excitation is created by the incident light beam from a synchrotron source or a gas-discharge lamp [45]. The same kind of excited state, a charge excitation, is also present in scanning tunneling spectroscopy where the electronic occupation is changed due to an applied voltage bias. In PES, probing states above the Fermi level is a difficult task since some electrons have to be excited to the unoccupied states first, for example as in inverse photoelectron spectroscopy [101] or using pump laser pulses as done in time-resolved photoelectron spectroscopy (tr-PES) [89]. In STS, however, those states are probed conveniently as the applied bias changes from negative to positive. In a scanning tunneling microscope, the differential conductance dI/dV is measured as a function of the tip position, which can be controlled in three spatial dimensions x, y parallel and z perpendicular to the sample's surface. A precision in the picometer range can be achieved [42], making it possible to measure on-site spectral function in real space. The information obtained using STS complements data measured by ARPES since it lacks k-resolution but instead gives a high lateral resolution as well as access to the states both above and below Fermi level.

In this chapter we analyse tunneling conductance data [106] that reveal distinct shoulder-like features at occupied and unoccupied states beyond the Mott gap $\Delta \approx 620$ meV. We show, using the self-consistent Born approximation, that these anomalies at the positive bias side can be interpreted as the spin-polaron ladder spectrum in this material. On the negative bias side, however, the internal degree of freedom of the charge excitation renders incoherence of the quasiparticle and broadens the delta-function-like features, so the observed peaks is interpreted as singlet and triplet states of the spin polaron. These results confirm the strongly correlated electronic structure of square-lattice iridates.

In the following we discuss spin-polaron ladder spectrum of Sr_2IrO_4 probed by scanning tunneling spectroscopy presented in [106] mostly focusing on the theoretical theoretical description of the tunneling conductance spectra. First, we introduce the t-J_z model and ladder physics in section 4.2. Then, the experimental STS data (courtesy by Z. Sun, J. M. Guevara, D. Baumann, K. Manna, S. Wurmehl, B. Büchner and C. Hess) are discussed in the section 4.3. Derivation of the model is discussed in section 4.4.1 followed by the general discussion on the nature of the ladder spectra introduction in section 4.4.2. In 4.4.3 we will discuss the relevance of the classical t-J_z model to the model discussed here and show that ladder spectrum can indeed be directly observed from the STS measurements. Finally, we highlight the main conclusions in section 4.5.

4.2. Introduction

As discussed in chapters 1 and 3, the motion of a single charge (hole or doublon) added to the AF and insulating ground state of the undoped Sr_2IrO_4 can be modeled within the spin-polaron model. As will be shown in section 4.4, within this model the shoulder-like features at unoccupied states in the STS spectra are directly related to an inherent ladder spectrum attributed to the presence of confined spin polaron quasiparticles in Sr_2IrO_4.

But before we proceed, let us discuss the ladder spectrum which in classical example occurs in the much simpler t-J_z model. Assuming the ground state to be *exactly* a classical Néel state (i.e. without spin fluctuations), one can describe the motion of the hole in the AF

background by a t-J_z model which naturally follows from the anisotropic t-J model [50] in the Ising limit $\alpha = J_\perp/J_z = 0$:

$$\mathcal{H} = \sum_{\mathbf{q}} \omega_{\mathbf{q}} a^\dagger_{\mathbf{q}} a_{\mathbf{q}} + \frac{zt}{\sqrt{N}} \sum_{\mathbf{k},\mathbf{q}} a^\dagger_{\mathbf{q}} h^\dagger_{\mathbf{k}} h_{\mathbf{k+q}} \left(u_{\mathbf{q}} \gamma_{\mathbf{k-q}} + v_{\mathbf{q}} \gamma_{\mathbf{k}}\right) + \text{h.c.}, \tag{4.1}$$

where a charge excitation is described by a spinless fermion with creation operator $h^\dagger_{\mathbf{k}}$ and spin excitations are represented by the boson operators $a^\dagger_{\mathbf{q}}$. The spin-wave dispersion $\omega_{\mathbf{q}} = zsJ\left(1-\delta\right)^2 \nu_{\mathbf{q}}$ where $s = 1/2$ is the spin and z is the coordination number of the underlying square lattice and the Bogoliubov factors are given by

$$\begin{aligned} \nu_{\mathbf{q}} &= \sqrt{1-\alpha^2\gamma^2_{\mathbf{q}}}, \\ u_{\mathbf{q}} &= \sqrt{\frac{1+\nu_{\mathbf{q}}}{2\nu_k}}, \\ v_{\mathbf{q}} &= -\text{sign}(\gamma_{\mathbf{q}}) \sqrt{\frac{1-\nu_{\mathbf{q}}}{2\nu_{\mathbf{q}}}}, \end{aligned} \tag{4.2}$$

and coupling of the hole to magnons is described by $\gamma_{\mathbf{q}} = \frac{1}{z} \sum\limits_{\vec{\tau}} cos\mathbf{q} \cdot \vec{\tau}$ (see section 1.6 for a detailed discussion on the t-J model). Substituting $\alpha = 0$ to Eq. (4.1) we get the t-J_z model in explicit form

$$\mathcal{H} = \omega \sum_{\mathbf{q}} a^\dagger_{\mathbf{q}} a_{\mathbf{q}} + \frac{zt}{\sqrt{N}} \sum_{\mathbf{k},\mathbf{q}} \gamma_{\mathbf{k}} a^\dagger_{\mathbf{q}} h^\dagger_{\mathbf{k}} h_{\mathbf{k+q}} + \text{h.c.}, \tag{4.3}$$

where the coefficients become $\mathbf{q}$-independent: $\omega = szJ_z$ and $\gamma_{\mathbf{k}} = \frac{1}{2}(\cos k_x + \cos k_y)$.

Unlike in t-J model where the low energy excitations are described by Heisenberg Hamiltonian (1.3) and ground state can be modeled as a Néel state dressed with quantum fluctuations, in t-J_z model low-energy description is given by Ising Hamiltonian

$$\mathcal{H}_{\text{Ising}} = J_z \sum_{\langle i,j \rangle} \left(S^z_i S^z_j - \frac{n_i n_j}{4} \right), \tag{4.4}$$

for which a Néel state is the exact solution for $J > 0$.

A hole introduced into the AF background interacts strongly with its environment of ordered spins and forms a new quasiparticle – the spin polaron. Its excitations in t-J_z model have been investigated within the self-consistent Born approximation [50, 74] and quantum wave function methods [94]. These studies show that the spin polaron is characterized by coupling to a string of misaligned spins, forming an effective potential of confinement where the polaron can occupy excited states of different orbital-like character [122] as shown in Fig. 4.1.

The one-particle spectrum of the hole in the t-J_z model calculated using SCBA is shown in Fig. 4.2. It is characterized by dispersionless excitations separated by energy intervals, first of which is proportional to $t(J_z/t)^{2/3}$ [14]. This *ladder-like* spectrum is typically observed if the particle is confined by a correlated background. In our case the confinement is created by strings of spin defects in the AF background, which are not allowed to relax due to the absence of the spin-flip terms (Eqs. (1.10-1.11)) in the Ising Hamiltonian (4.4) as compared to the Heisenberg Hamiltonian (1.3). The different internal excitations of the hole within this so-called spin polaron shown in Fig. 4.1 manifest themselves as the different "rungs" in the corresponding ladder spectrum.

If the spin-flip processes are allowed, i.e., the ground state is dressed with quantum fluctuations, spin defects can relax and the quasiparticle becomes dispersive, thus partially (or in some cases even completely) encaving the ladder structure.

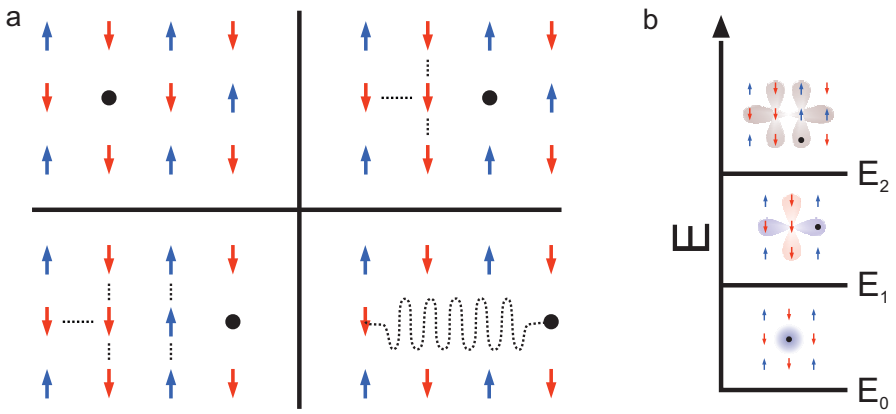

Figure 4.1.: Behavior of a hole in a strongly correlated antiferromagnetic background forming the spin polaron. (a) The motion of the hole is accompanied by the creation of strings of misaligned spins (indicated by dotted lines) leading to an effective potential which prevents the hole to move freely (wavy dotted line). (b) Some of the possible internal excitations of the spin polaron with respect to the number of misaligned spins and symmetry of orbital momentum. The excitation energy values are well separated and appear in the one-particle spectrum as characteristic "ladder structure". Courtesy by J. M. Guevara [106].

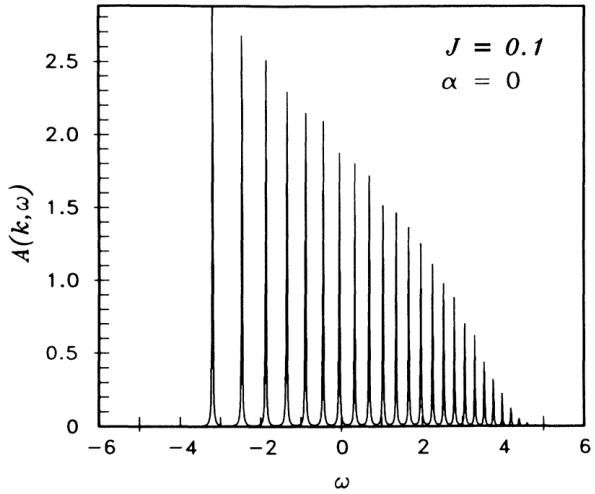

Figure 4.2.: Spectral function of a hole in the t-J_z model. Calculated on the lattice 16×16 with $J = 0.1t$ and broadening $\delta = 0.01t$. Reproduced from Ref. [74].

4.3. Experimental results

The tunneling spectroscopy measurements were performed on single crystals of $Sr_2IrO_{4-\delta}$. The crystals exhibit a slightly reduced resistivity as compared to the stoichiometric parent compound, allowing for high-resolution STS measurements even at very low temperature ($T < 10$ K). STM data obtained at the cold-cleaved crystal surface (Fig. 4.3(a)) yield atomically resolved SrO-terminated flat terraces with several local defects, about 2% with respect to Ir.

Fig. 4.3(b) shows an overview tunneling conductance dI/dV spectrum taken at 8.8 K at

a place free of defects. The data reveal a sizable gap $\Delta \approx 620$ meV, where $dI/dV \approx 0$, in agreement with earlier findings [26, 124]. Remarkably, at larger bias voltages V_{bias}, distinct shoulder-like structures are visible (indicated by arrows). These interesting features suggest a direct coupling of the tunneling electrons/holes to some specific excitations of the correlated Mott state. There are resonance peak-like features in the conductance spectrum at about 700 mV and 1100 mV. These signatures are directly related to the presence of an inherent ladder spectrum attributed to the presence of confined spin polaron quasiparticles in Sr_2IrO_4 as will be shown in sections (4.4.1 – 4.4.3). Also at the negative bias side, there are clear although less pronounced peaks at about 300 mV and 700 mV below the Fermi level, which shall be interpreted as singlet and triplet states of the spin polaron. We note that the spectra at negative bias side are in general more continuous.

At larger $V_{\text{bias}} \gtrsim 1.3$ eV, the dI/dV spectra increase sharply. Because of a strong energy dependence of the tunneling matrix element, higher-order electronic excitations and dominant oxygen $2p$ orbital contributions at such large energies, also comparing with the optical results [91], we restrict our discussion to the rich and interesting structure at $|V_{\text{bias}}| \lesssim 1.3$ eV.

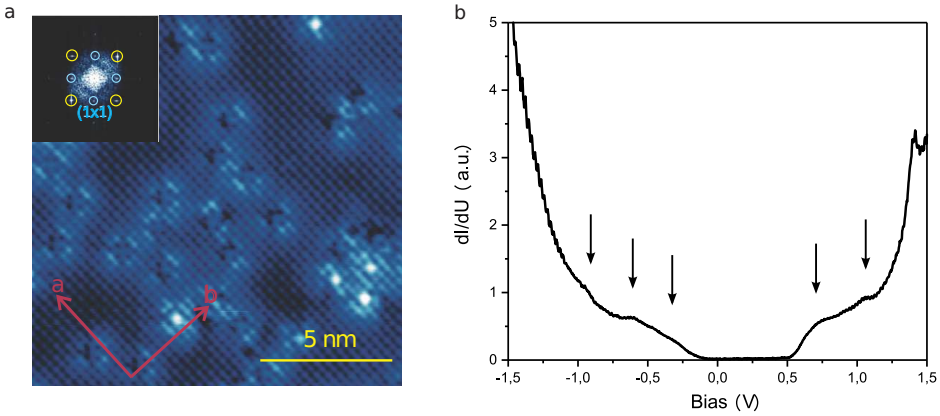

Figure 4.3.: Topography and experimental tunneling conductance of the clean area of the surface. (a) Topography of the sample surface for the defect-free area with bias voltage 1.0 V. The onset shows the Fourier transition of the topography image, where we labeled the Bragg peak and the (1×1) reconstruction. (b) Large scale tunneling conductance spectrum taken on a clean place. Courtesy by J. M. Guevara [106].

4.4. Modeling the tunneling data

4.4.1. Derivation of the theoretical model

Constructing a polaronic model to calculate dI/dV spectra, we address separately the positive and negative bias regions since the strong on-site correlations render these two cases very different [86]. When a negative bias is applied, an electron is removed from the d^5 configuration creating an excitation which can be locally described as a d^4 configuration with its complicated intrinsic multiplet structure. Thus, this charge excitation in the lowest energy subspace of the Hilbert space would form a singlet and a triplet state. The corresponding charge excitation creation operator $\mathbf{h}$ would therefore posses an additional internal degree of freedom $|\mathbf{h}\rangle \equiv \{|J=0\rangle, |J=1, J_z=1\rangle, |J=1, J_z=0\rangle, J=1, J_z=-1\rangle\}$. Opposite to this, applying positive bias results in adding an electron to the local Ir site with d^5 configuration. Hence, the charge excitation one has to consider would resemble the filled-shell d^6 configuration and be described by polaronic excitations shown in Fig. 4.1.

The motion of the charge excitation on positive (+) and negative (−) sides of the dI/dV spectra is described by the Hamiltonian

$$\mathcal{H}^{+,-} = \mathcal{H}_{\text{mag}} + \mathcal{H}_t^{+,-}, \tag{4.5}$$

where $\mathcal{H}_{\text{mag}}$ describes low energy excitations of the AF $J_{\text{eff}} = 1/2$ ground state. It is derived from Heisenberg model (1.3) by applying consequently Fourier, Hostein-Primakoff and Bogoliubov transformations (see section 1.6 for details) and is given by

$$\mathcal{H}_{\text{mag}} = \sum_{\mathbf{k}} \omega_{\mathbf{k}} (\alpha_{\mathbf{k}}^\dagger \alpha_{\mathbf{k}} + \beta_{\mathbf{k}}^\dagger \beta_{\mathbf{k}}), \tag{4.6}$$

where $\omega_{\mathbf{k}}$ is the dispersion of the (iso)magnons represented by the quasiparticle states $|\alpha_{\mathbf{k}}\rangle$ and $|\beta_{\mathbf{k}}\rangle$. The hopping part of the Hamiltonian, $\mathcal{H}_t^{+,-}$, describes the transfer of the charge excitation in the bulk coupled to the magnons (which we also address as polaron quasiparticle). It is given by

$$\begin{aligned}
\mathcal{H}_t^+ &= \sum_{\mathbf{k}} V_{\mathbf{k}}^0 \left(d_{\mathbf{k}A}^\dagger d_{\mathbf{k}A} + d_{\mathbf{k}B}^\dagger d_{\mathbf{k}B} \right) + \sum_{\mathbf{k},\mathbf{q}} V_{\mathbf{k},\mathbf{q}} \left(d_{\mathbf{k-q}B}^\dagger d_{\mathbf{k}A} \alpha_{\mathbf{q}}^\dagger + d_{\mathbf{k-q}A}^\dagger d_{\mathbf{k}B} \beta_{\mathbf{q}}^\dagger + \text{h.c.} \right), \qquad (4.7) \\
\mathcal{H}_t^- &= \sum_{\mathbf{k}} \left(\mathbf{h}_{\mathbf{k}A}^\dagger \hat{V}_{\mathbf{k}}^0 \mathbf{h}_{\mathbf{k}A} + \mathbf{h}_{\mathbf{k}B}^\dagger \hat{V}_{\mathbf{k}}^0 \mathbf{h}_{\mathbf{k}B} \right) + \sum_{\mathbf{k},\mathbf{q}} \left(\mathbf{h}_{\mathbf{k-q}B}^\dagger \hat{V}_{\mathbf{k},\mathbf{q}}^\alpha \mathbf{h}_{\mathbf{k}B} \alpha_{\mathbf{q}}^\dagger + \mathbf{h}_{\mathbf{k-q}A}^\dagger \hat{V}_{\mathbf{k},\mathbf{q}}^\beta \mathbf{h}_{\mathbf{k}B} \beta_{\mathbf{q}}^\dagger + \text{h.c.} \right),
\end{aligned}$$

where A, B are the two antiferromagnetic sublattices. The dispersions $V_{\mathbf{k}}^0$ ($\hat{V}_{\mathbf{k}}^0$) describe the nearest, next nearest, and third neighbor free hopping. The terms $V_{\mathbf{k},\mathbf{q}}$ ($\hat{V}_{\mathbf{k},\mathbf{q}}^\alpha$ and $\hat{V}_{\mathbf{k},\mathbf{q}}^\beta$) are vertices describing the polaronic hopping of the charge excitation on the positive (negative) side and are given explicitly in Eqs. (3.12 – 3.14). The Hamiltonians (4.7) resemble Hamiltonians (3.7) and (3.11) and their derivation is given explicitly in chapter 3. All the vertices were obtained analytically in the limit of strong on-site Coulomb repulsion and depend on the five hopping parameters of the minimal tight-binding model obtained as the best fit of the latter to the LDA calculations.

The tunneling conductance spectra are then obtained as

$$dI/dV(\omega) \propto -\frac{1}{2\pi} \sum_{\mathbf{k}} \text{Im} G(\mathbf{k}, \omega), \tag{4.8}$$

where the Green's function is calculated using SCBA as

$$G(\mathbf{k}, \omega)^- = \text{Tr} \langle \text{AF} | \mathbf{h}_{\mathbf{k}} \frac{1}{\omega - \mathcal{H}^- + i\delta} \mathbf{h}_{\mathbf{k}}^\dagger | \text{AF} \rangle, \tag{4.9}$$

$$G(\mathbf{k}, \omega)^+ = \langle \text{AF} | d_{\mathbf{k}} \frac{1}{\omega - \mathcal{H}^+ + i\delta} d_{\mathbf{k}}^\dagger | \text{AF} \rangle, \tag{4.10}$$

where $d_{\mathbf{k}}^\dagger$ creates an electron on the positive side of the conductance spectra and the charge excitation vector operator $\mathbf{h}_{\mathbf{k}}^\dagger$ creates a hole with four internal degrees of freedom $|\mathbf{h}\rangle$ described above.

The calculated tunneling conductance spectra displayed in Fig. 4.4 show the ladder structure of the peaks on the positive bias side typical for the t-J_z model even though the model described here is more complicated. This ladder structure on the positive bias side can be clearly identified from the experimental data, see peaks at about 700 mV and 1100 mV. One can see that position of the peaks in the theoretical calculation corresponds very well to that in the experiment. We note, that the tunneling spectra on the positive side is further broadened by other effects including measurement precision and electron-phonon scattering processes, which are not taken into account in our effective low-energy model. We also note, that there are no adjustable parameters in the calculation apart from the total energy shift

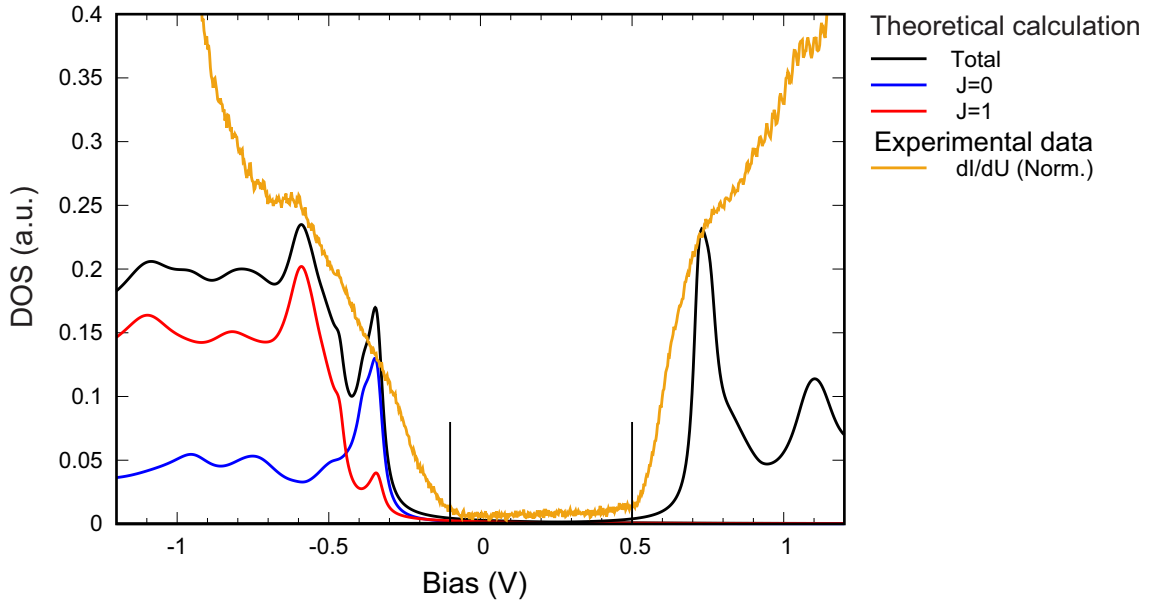

Figure 4.4.: Tunneling conductance spectra for the clean surface: Experiment is shown in brown, calculated within SCBA full spectra – in black. Additionally, J-resolved calculated spectra are shown, with blue corresponding to charge excitations with total angular momenta $J = 0$ and red to $J = 1$. The spectra are offset by $E = -0.9$ V (negative side) and $E = -1.52$ V (positive side). Broadening of 10 meV was used.

coming from chemical potential, which cannot be included in the polaronic model directly and on which the distance between two peaks in theoretical spectra does not depend. In sections 4.4.2 – 4.4.3 it is shown that indeed, the ladder spectrum features can be directly observed in STS measurements.

Not surprisingly, however, such ladder spectrum is not present on the negative bias side. The polaron motion on the negative voltage is additionally complicated by the internal degree of freedom of the charge excitation, which not only creates additional interacting channels but also provides a possibility for a nearest-neighbor free hopping of the polaronic quasiparticle. This renders polaron quasiparticle less localized and more dispersive, greatly broadening delta-like features, thus encaving the internal polaron excitation structure shown in Fig. 4.1, and transfers some spectral weight to the incoherent part of the spectra.

By studying separate contributions to the total Green's function $G(\mathbf{k}, \omega)^-$ in Eq. (4.9) instead of taking the trace, one can access the Green's function for a polaron carrying particular value of total quantum momenta $J = 0, 1$ and study the manifestation of these additional degrees of freedom in the spectral function. Such J-resolved spectra are shown in Fig. 4.4 in blue and red correspondingly. Unlike on the positive bias side, the two peaks observed on the negative side of the tunneling conductance spectra correspond to singlet and triplet polarons rather than to the ladder-like features.

By careful analysis of the spectra shown on on Fig. 2.2 one can also extract the value of Coulomb repulsion. The Hubbard U is connected to the Mott gap value Δ^{Mott} as

$$\Delta^{\text{Mott}} = U - E^{\text{pol}}_{\text{hole}} - E^{\text{pol}}_{\text{electron}}, \tag{4.11}$$

where $E^{\text{pol}}_{\text{hole}}$ ($E^{\text{pol}}_{\text{electron}}$) is the binding energy of the polaron formed when a hole (electron) is added to the ground state of the system. We estimate polaron binding energies by performing SCBA calculations setting the hopping part of Hamiltonian Eq. (4.7) to zero separately for

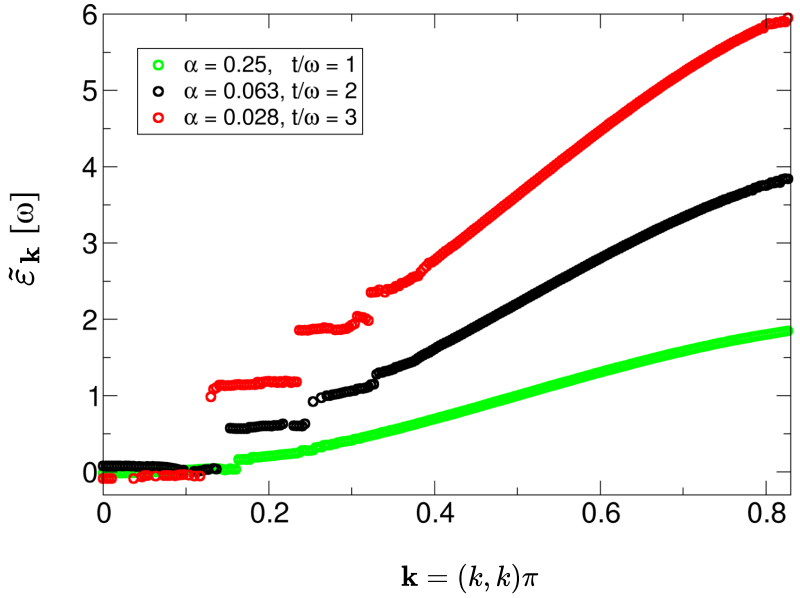

Figure 4.5.: Polaronic quasiparticle dispersion for the effective Hamiltonian of the anisotropic t-J model given by Eq. ((4.1)) calculated for three different values of the ratio $\alpha = J_\perp/J_z$. The value of t is fixed throughout the calculation. The spectrum becomes more ladder-like as α approaches the Ising limit $\alpha = 0$. For the lowest value of α (red circles) the value of t/ω lies in the relevant for Sr_2IrO_4 parameter region (as indicated in Fig. 4.6(b)) and the energy spacing between the first and second excitation is of the order of J. Courtesy by S. Sykora.

positive and negative bias cases. This way the polaron is artificially fully localized and its spectral function is simply a delta function. The binding energies are then calculated as a relative shift between these delta function peaks and quasiparticle peaks in the full calculation (Fig. 4.4) and are estimated to be

$$\begin{aligned} E^{\text{pol}}_{\text{hole}} &= 0.57\,\text{eV} \\ E^{\text{pol}}_{\text{electron}} &= 0.81\,\text{eV}. \end{aligned} \tag{4.12}$$

Then the Coulomb repulsion $U = 2.05 - 2.18$ eV since the Mott gap $\Delta^{\text{Mott}} \approx \Delta$ correct to the lowest quasiparticle peak bandwidth (both on positive and negative bias sides).

4.4.2. Ladder spectrum in the the t-J_z model

To show that indeed different excitations in the ladder spectrum of the t-J_z model can be directly observed in the tunneling spectroscopy experiment, we map the polaronic Hamiltonian (4.1) onto an effective system of free fermions and bosons

$$\tilde{\mathcal{H}} = \sum_{\mathbf{q}} \tilde{\omega}_{\mathbf{q}} \alpha^\dagger_{\mathbf{q}} \alpha_{\mathbf{q}} + \sum_{\mathbf{k}} \tilde{\varepsilon}_{\mathbf{k}} f^\dagger_{\mathbf{k}} f_{\mathbf{k}}, \tag{4.13}$$

where the new effective Hamiltonian $\tilde{\mathcal{H}}$ is related to the original Hamiltonian via a unitary transformation, $\tilde{\mathcal{H}} = e^X \mathcal{H} e^{-X}$. Such a method enables to study the polaron excitations as projected on the effective free particle, which can directly couple to the tunneling electrons in the STS experiment.

The unitary transformation e^X in general renormalizes the spin excitations of the background (first term of Eq. (4.13)) and generates the second term of Eq. (4.13). Since the

Eq. (4.13) has the quadratic diagonal form and the transformation e^X is unitary, the energy quantities $\tilde{\varepsilon}_{\mathbf{k}}$ and $\tilde{\omega}_{\mathbf{q}}$ can be seen as eigenenergies of the original model. The transformation e^X can be constructed and numerically carried out by using the projective renormalization method (PRM) (see Ref. [21]). Within this method the polaronic term of the Hamiltonian is integrated out in steps (1500 in the actual calculation), leading to the renormalization of the fermion and boson energy parameters.

Using the unitary transformation e^X, the one-particle spectral function can be calculated immediately,

$$A_{\mathbf{k}}(E) = |\tilde{a}^0_{\mathbf{k}}|^2 \delta(E - \tilde{\varepsilon}_{\mathbf{k}}) + \frac{1}{N} \sum_{\mathbf{q}} |\tilde{a}^1_{\mathbf{k},\mathbf{q}}|^2 \delta(E - \tilde{\varepsilon}_{\mathbf{k}-\mathbf{q}} - \tilde{\omega}_{\mathbf{q}}) + \ldots, \tag{4.14}$$

where $\tilde{a}^0_{\mathbf{k}}$ and $\tilde{a}^1_{\mathbf{k},\mathbf{q}}$ are calculated in the renormalization process described above and represent the spectral weight of the particular polaron excitation.

The internal excitations of the polaron can also be visualized by its wave function. Following [94], we write it in the form

$$|\Psi_{\mathbf{k}}\rangle = a^0(\mathbf{k}) f^\dagger_{\mathbf{k}} |0\rangle + \frac{1}{\sqrt{N}} \sum_{\mathbf{q}} a^1(\mathbf{k},\mathbf{q}) f^\dagger_{\mathbf{k}-\mathbf{q}} \alpha^\dagger_{\mathbf{q}} |0\rangle + \ldots. \tag{4.15}$$

Here, $|0\rangle$ is the product of the hole vacuum and the spin-wave vacuum, and $\tilde{a}^0_{\mathbf{k}}$, $\tilde{a}^1_{\mathbf{k},\mathbf{q}}$ are so-called *Reiter* coefficients. We see that the wave function of the doped hole can in principle be approximated by a superposition of the wave function of a free hole and m wave functions of the hole dressed with m magnons.

Fig. 4.5 shows the calculated effective dispersion of the spin polaron for different values of the ratio $\alpha = J_\perp/J_z$. For small values of α, i.e. close to the Ising limit, one clearly sees that the energy of the polaron increases as a function of its momentum $\mathbf{k}$ in stair-step fashion: as soon as the momentum $\mathbf{k}$ is sufficiently large to produce a magnon, the polaron is raised to the next excited level. The ground state of the polaron is characterized by momentum states around $\mathbf{k} = 0$ where only a finite range of momentum values is occupied. Since the values of α examined in Fig. 4.5 are small ($\alpha < 0.25$), the magnon dispersion $\tilde{\omega}_{\mathbf{q}}$ is almost momentum-independent and approximately equal to the magnon dispersion in the t-J_z model 4.3. For smaller values of $\alpha = 0.028$ (shown in Fig. 4.5 with red circles), the polaron dispersion within each rung is quite flat, whereas for larger values of $\alpha = 0.25$ (green circles), the polaron becomes more dispersive. Overall, the polaron becomes less localized with the ratio t/ω decreasing.

The possibility to map the spin polaron model to an effective model of free charge carriers (dressed with characteristic ladder-like quasiparticle dispersion) indicates that it must indeed be possible to detect internal excitations of spin polarons in STM experiment.

To get better understanding of the nature of polaron states shown on the Fig. 4.1, we calculate first two Reiter coefficients $a^0(\mathbf{k})$ and $a^1(\mathbf{k},\mathbf{q})$ from Eq. 4.15 using perturbation theory with respect to the parameter t/ω assuming $\omega \gg t$ (strong coupling limit):

$$\begin{aligned} a^0(\mathbf{k}) &= 1 - \frac{1}{N} \sum_{\mathbf{q}} \frac{\gamma^2_{\mathbf{k}-\mathbf{q}}}{\omega^2} \\ a^1(\mathbf{k},\mathbf{q}) &= \frac{\gamma_{\mathbf{k}-\mathbf{q}}}{\omega}. \end{aligned} \tag{4.16}$$

In this approximation, the spectral function of the hole has the form (similar to Eq. 4.14)

$$A_{\mathbf{k}}(E) = [a^0(\mathbf{k})]^2 \delta(E) + \frac{1}{N} \sum_{\mathbf{q}} \frac{\gamma^2_{\mathbf{k}-\mathbf{q}}}{\omega^2} \delta(E - \omega). \tag{4.17}$$

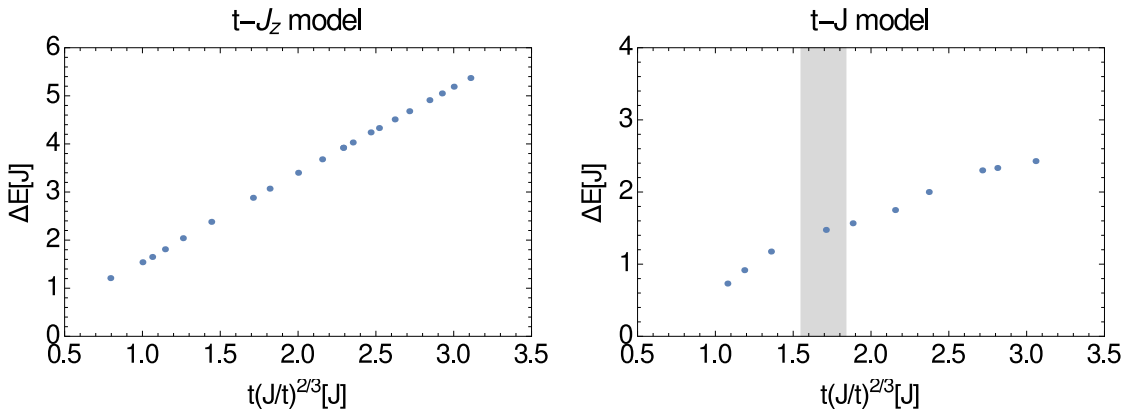

Figure 4.6.: Comparison of energy spacing between first and second excitation state of polaron scaling as a function of J/t ratio: (a) t-J_z model, (b) material-specific t-J model defined by H^+ in Eq. (4.5). In light gray the region of the J/t values relevant for the Sr_2IrO_4 is shown: $J = 0.06$ eV, first neighbor hoppings takes values from 0.224 eV to 0.373 eV depending on the orbital character.

This equation includes two different types of internal excitations. As one can see from the momentum dependence of the Reiter coefficients, the lowest excitation $a^0(\mathbf{k})$ has s-wave character and represents a rather localized state of the hole. The second excitation $a^1(\mathbf{k}, \mathbf{q})$ is spatially more extended due to its proportionality to cos-functions, and the sign of the coefficient changes as a function of momentum, which means that it is orthogonal to the first term.

4.4.3. Relevance of the t-J_z ladder physics to Sr_2IrO_4

To show relevance of the above discussed theory to the case of Sr_2IrO_4, we have calculated the scaling of the energy spacing between the first and second excited states on the positive side of the tunneling conductance as a function of J/t ratio for the material specific t-J-like model (4.5). It is known, that for the t-J_z model this energy spacing scales as $t(J_z/t)^{2/3}$ [14], see Fig. 4.6(a). As one can see on the Fig. 4.6(b), first energy gap calculated for model (4.5) follows the same law in the region of parameters relevant to the real material Sr_2IrO_4 (shown in light gray).

4.5. Conclusions

We have analyzed the STM/STS spectra of clean surfaces of Sr_2IrO_4. The observation of nearly equidistant peak-like features in the spectrum indicates the direct coupling of the tunneling carriers to specific internal excitations of the underlying antiferromagnetic Mott system. The experimental results are compared with the calculated spectrum based on a realistic spin polaron model which has been also used to consistently describe measured ARPES spectra of Sr_2IrO_4. We find excellent agreement between the measurements and theory.

We have investigated the excitations on the positive and negative sides of the tunneling conductance spectra using SCBA. We conclude that for the positive bias, STS probes the spin-polaron ladder spectrum resulting from the confinement of the hole in the AF background as is well known from other anti-ferromagnetic Mott systems. The features on the negative bias side shall be assigned to singlet and triplet states of the spin polaron arising from the complicated multiplet structure of the charge excitations on the negative bias side. Thus, we

have shown that STS can probe internal excitations of quasiparticles.

CHAPTER 5

Spin-orbit interaction in Sr_2IrO_4: *jj* vs *LS* coupling schemes

5.1. Preface

The excellent agreement between the experimental and theoretical PES spectra on Sr_2IrO_4 discussed in the chapter 3 is both interesting and intriguing. Many theoretical works inspired by Ref. [46] have assumed, following Ref. [46], that the superexchange model for Sr_2IrO_4 can be derived by projecting the Kugel-Khomskii model (1.24) onto the SO basis (see section 1.5). However, this is a valid approach only if the virtual intermediate doubly occupied states considered in the second order perturbation theory can be well approximated by the $^3T_1$, $^1T_2$, ^1E and $^1A_1$ basis set. Such a basis set is defined by the full Coulomb Hamiltonian which includes the $10Dq$ crystal field as well as the Hund's coupling, but not SOC. In other words, this approach is valid in the limit of crystal field and Hund's coupling much larger than SOC. Consequently, the multiplet structure of d^4 configuration is well described by the LS coupling scheme. This is indeed the assumption made in chapter 3 while deriving the t-J-like model for Sr_2IrO_4.

Yet, for materials with large atomic number Z, such as Ir, SOC is expected to be larger than the Hund's coupling. It is well known that the electrostatic energy of an electron in the field of atomic charge Ze scales as

$$\bar{\lambda} \sim \left(\frac{Ze^2}{\hbar c}\right)^2 \frac{me^4}{\hbar^2}\,. \tag{5.1}$$

Thus, SOC scales as Z^2, and naturally the heavier the atom, the more pronounced this effect will be. It should be noted that SOC strength is often said to scale as Z^4, which is not precisely correct because once we consider spin-orbit coupling as a perturbation, we have to average it over the non-perturbed state to calculate the energy. For an electron in the outer shell, this implies that Eq. (5.1) should be multiplied by the probability of the electron being in the proximity of the core, which scales as $1/Z^2$. Interested reader is referred to § 72 of the Landau and Lifshitz textbook [65]. It is known that the LS coupling scheme holds well for atoms in the iron group which includes Fe, Ni, Co [102]. For atoms in the platinum group consisting of Ru, Rh, Rd, Os, Ir, Pt, there are increasing deviations from the LS coupling scheme, and for heavier atoms such as Pb and Bi the LS coupling scheme is expected to fail.

As the relation of SOC to the electrostatic interaction increases with increasing atomic number Z, neither L nor S are any longer good quantum numbers and the LS coupling scheme breaks down. To estimate the relation between the electrostatic correlation and spin-orbit coupling we evaluate the ratio [132]

$$\chi = \frac{\xi}{F_2}\,, \tag{5.2}$$

where ξ is SOC defined in Eq. (5.11) and F_2 is a Slater integral connected to the Slater parameter $F^{(2)}$ as $F_2 = F^{(2)}/49$ [93] for d^2 configuration. The Slater parameters can be evaluated using Racah parameters B and C [92, 93] as

$$F^{(2)} = 49\left(B + \frac{5}{441}F^{(4)}\right), \tag{5.3}$$

$$F^{(4)} = \frac{441}{35}C. \tag{5.4}$$

Adopting the values for Racah parameters of an Ir^{4+} ion in an octahedral crystal field from Ref. [5] we get

$$F^{(2)} = 35280\,\mathrm{cm}^{-1}, \tag{5.5}$$

$$F^{(4)} = 26460\,\mathrm{cm}^{-1}, \tag{5.6}$$

and the Slater integral $F_2 = 720\,\mathrm{cm}^{-1}$. Substituting $\xi \approx 0.4\,\mathrm{eV} \approx 3226\,\mathrm{cm}^{-1}$, we get

$$\chi \approx 4.48. \tag{5.7}$$

It is known that the *LS* coupling scheme is a good approximation for values $\chi \lesssim 1$ [132]. Therefore, for the case of iridium the choice of the *LS* coupling scheme is questionable.

At the same time, caution must be exercised in the choice of the coupling scheme. For example, the authors of Ref. [52] claim that $4d$ and $5d$ transition metal ions with t_{2g}^4 configuration such as Re^{3+}, Ru^{4+}, Os^{4+} and Ir^{5+} realize a low-spin $S = 1$ state because of relatively large Hund's coupling J_H, and therefore the multiplet structure should be calculated within the *LS* coupling scheme. While it is likely to be true for Ru^{4+} as a $4d$-element, which is in fact the only element discussed in detail in Refs. [3, 18, 52], the validity of the statement for heavier elements of the platinum group (e.g. TM ions with partly filled $5d$ shell) is not *a priori* known.

In this chapter, therefore, we investigate the implications of the two coupling schemes in the experimental observations on Sr_2IrO_4. In particular, we study theoretical ARPES and STS spectra caclualated within the *jj* coupling scheme and compare them with the corresponding results obtained earlier in chapters 3 – 4. This is particularly relevant in view of the fact that a number of assumptions in the theoretical investigations of iridates have been doubted or even proved wrong later on. For example, the number of nearest neighbor couplings required to fit the magnon dispersion [59], and the critical role played by the in-plane rotations of oxygen octahedra and distortions in resolving the puzzling behavior (see [15] and chapter 1).

We first discuss how *LS* and the *jj* coupling schemes appear in perturbation theory calculations of the multiplet structure in section 5.2. In section 5.3, we discuss the case of two holes on t_{2g} shell relevant for theoretical modeling of the ARPES spectra of iridates. After that in section 5.4 we discuss how the choice of the coupling scheme manifests itself in the *t-J* model. We show how the kinetic Hamiltonian derived in chapter 3 describing hopping of one electron from one site to another depends on the coupling scheme. In section 5.5, the relevance of all these results to the calculation of ARPES spectra on Sr_2IrO_4 will be discussed. Finally, the conclusions will be made in section 5.6.

5.2. Introduction

In the classical textbooks [23, 65, 102], computing the multiplet structure in both *LS* and the *jj* coupling schemes has been discussed. Most of the textbooks deal with the *LS* coupling scheme in some detail including the consideration of more sophisticated problems such as possible violation of the Pauli principle in orbital configurations. However, not much attention is usually paid to the *jj* coupling scheme [95]. Some authors discuss it in much greater detail and even link the two coupling schemes [102]. However, details including basis transformations of wave functions in both coupling scheme are often left out.

In short, the *LS* and the *jj* coupling schemes are two different ways to sum up the individual spin or orbital momenta of electrons to obtain the total momenta J describing the system. For a single atom in the lattice, there are two effects to consider: (i) interaction between one-particle spin $\mathbf{s}$ and orbital $\mathbf{l}$ momenta $\mathbf{j} = \mathbf{l} + \mathbf{s}$ and (ii) electrostatic interaction between the electrons (in particular, its direction-dependent, i.e. angular part):

$$\mathbf{L} = \mathbf{l}_1 + \mathbf{l}_2 + \dots, \tag{5.8}$$

$$\mathbf{S} = \mathbf{s}_1 + \mathbf{s}_2 + \dots. \tag{5.9}$$

Naturally, both of these effects have to be included into the full Hamiltonian describing the system. In order to solve the full Hamiltonian one chooses to treat both effects perturbatively since the exact solution requires immense computational power and is often not possible.

Depending on the order of included perturbations, one or another coupling scheme is said being used. Let us start with a full Hamiltonian in its general form

$$\mathcal{H} = \tilde{\mathcal{H}} + \mathcal{H}_{\mathrm{SOC}}, \tag{5.10}$$

where $\mathcal{H}_{\mathrm{SOC}}$ describes the sum of all the on-site spin-orbit interactions (1.32)

$$\mathcal{H}_{\mathrm{SOC}} = \sum_{i=1}^{N} \xi_i \mathbf{l}_i \mathbf{s}_i, \tag{5.11}$$

and $\tilde{\mathcal{H}}$ is the full Schrödinger Hamiltonian

$$\tilde{\mathcal{H}} = \sum_{i=1}^{N} \left(-\frac{1}{2}\nabla_{r_i}^2 - \frac{Z}{r_i} \right) + \sum_{i>j}^{N} \frac{1}{r_{ij}}\,, \tag{5.12}$$

where Z is the atomic number of the nucleus and N is the total amount of electrons in the system.

Naturally, in a completely filled orbital, half of the electrons have spin up, the other half spin down, therefore filled shells have zero contribution to the total $\mathbf{S}$. Moreover, for each electron on the orbital $\mathbf{l}$ with a quantum momentum m_l there is an electron with the quantum momentum $-m_l$, so the filled shell contribution to the total $\mathbf{L}$ momentum is zero as well. Therefore electrons in closed shells are not considered in the sum in Eq. (5.11). It should be noted that in the limit of strong electron-electron correlation and under certain approximations, e.g. neglecting inter-site electron-electron correlation and kinetic interactions between farther neighbors Eq. (5.12) can be mapped onto the multiorbital Hubbard model (1.14).

The Hamiltonian (5.12) can be separated into a central field part, which includes kinetic energy of all electrons, nucleus-electron Coulomb interaction and central-symmetric part $S(r_i)$ of the Coulomb electron-electron repulsion

$$\mathcal{H}_{\mathrm{CF}} = \sum_{i=1}^{N} \left(-\frac{1}{2}\nabla_{r_i}^2 - \frac{Z}{r_i} + S(r_i) \right), \tag{5.13}$$

and a residual Coulomb Hamiltonian

$$\mathcal{H}_{\mathrm{res}} = \sum_{i>j}^{N} \frac{1}{r_{ij}} - \sum_{i=1}^{N} S(r_i), \tag{5.14}$$

describing the angular part of the Coulomb interaction between electrons. The relevant energy scales are the on-site Coulomb repulsion U and Hund's couping J_H corresponding to the Hamiltonians (5.13) and (5.14), respectively.

To solve Eq. (5.10), we invoke perturbation theory taking $\mathcal{H}_{\mathrm{CF}}$ to be the unperturbed part of the Hamiltonian since usually in lattices $\mathcal{H}_{\mathrm{CF}} >> \mathcal{H}_{\mathrm{res}}$ and $\mathcal{H}_{\mathrm{CF}} >> \mathcal{H}_{\mathrm{SOC}}$. The eigenstates of this unperturbed system are described by ψ_{CF}:

$$\mathcal{H}_{\mathrm{CF}} \left|\psi_{\mathrm{CF}}\right\rangle = E_{\mathrm{CF}} \left|\psi_{\mathrm{CF}}\right\rangle, \tag{5.15}$$

and define the electronic configuration $\psi_{\mathrm{CF}} = |n_1\, l_1, n_2\, l_2, \ldots, n_{\mathrm{N}} l_{\mathrm{N}}\rangle$ where n_i is a principal quantum number of the i-th particle. Each electronic configuration $|n_1\, l_1, n_2\, l_2, \ldots, n_{\mathrm{N}}\, l_{\mathrm{N}}\rangle$ consists of $\prod_{i=1}^{N} 2(2l_i+1)$ states, which are degenerate in the absence of the non-central-symmetric part of the Coulomb interaction and SO interaction.

Depending on whether $\mathcal{H}_{\mathrm{res}} > \mathcal{H}_{\mathrm{SOC}}$ or $\mathcal{H}_{\mathrm{SOC}} > \mathcal{H}_{\mathrm{res}}$ the equations (5.11) and (5.14) would be taken as the first and the second order perturbations. We consider two cases separately, starting with the former.

5.2.1. *LS* coupling scheme

If $\mathcal{H}_{\text{res}} > \mathcal{H}_{\text{SOC}}$, then the strongest perturbation to the eigenstates of $\mathcal{H}_{\text{CF}}$ can be calculated as $\langle \psi_{\text{CF}} | \mathcal{H}_{\text{res}} | \psi_{\text{CF}} \rangle$. Electronic configurations then split into *multiplet terms*

$$\psi^{LS} = |\gamma S\, M_S\, L\, M_L\rangle\,, \tag{5.16}$$

characterized by the total orbital **L** and spin **S** momenta that fulfill

$$[\mathcal{H}_{\text{res}}, \mathbf{L}] = [\mathcal{H}_{\text{res}}, \mathbf{S}] = 0. \tag{5.17}$$

Here $M_{L,S}$ is the projection of the **L**, **S** momenta on the quantization axis and $|\gamma\rangle$ stands for a particular electronic configuration. One usually uses Latin letters to label states with different L: S, P, D, F, G, H, I... refer to $L = 0, 1, 2, 3, 4, 5, 6...$, respectively. [102]. When SOC is added as a further perturbation, each multiplet term splits into levels described by the total momenta $\mathbf{J} = \mathbf{L} + \mathbf{S}$. As an example, in Fig. 5.1 one can see the splitting of multiplets for a p^2 configuration which is also relevant for theoretical modeling of the ARPES spectra of iridates as shown later in section 5.3. Such multiplet splitting is called *fine structure* and can be measured for example in extended x-ray absorption edge fine structure (EXAFS).

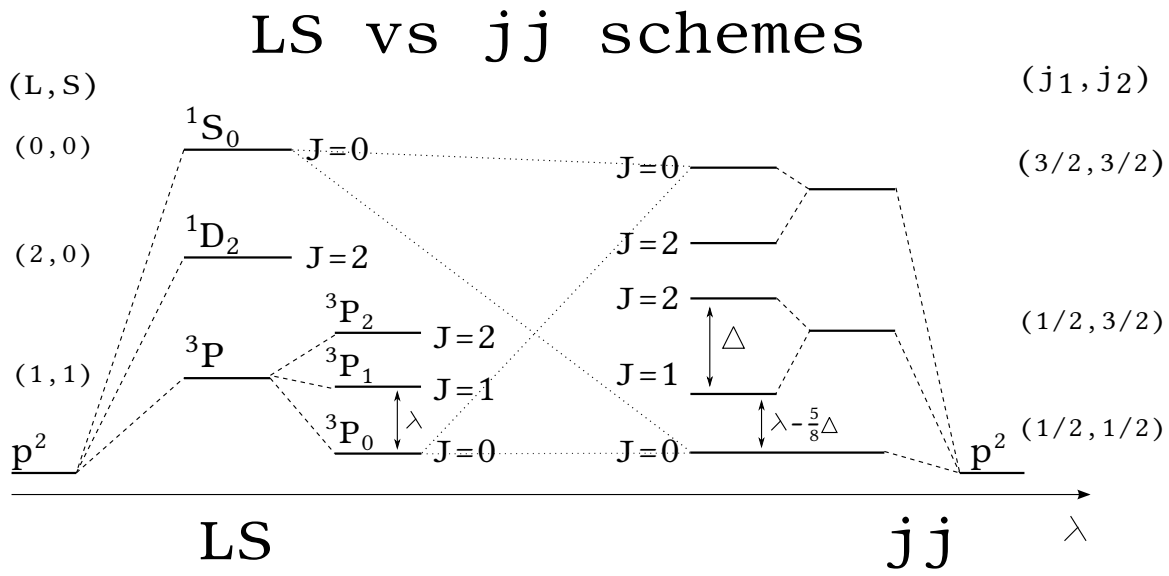

Figure 5.1.: Schematic representation of the multiplet structure for a p^2 configuration in the *LS* coupling scheme (left) and the *jj* coupling scheme (right). The mixing between ${}^3P_0$ and ${}^1S_0$ multiplets is schematically shown by dotted line (see section 5.4 for details) For comparison, the energy reference has been chosen to be equal in both coupling schemes.

The total momentum J can take values $L + S \geqslant J \geqslant |L - S|$. In most cases, $L \geqslant S$ and then there are $2S + 1$ different values of J, i.e. the level described by L, S under small SOC would split into $2S + 1$ different components. Therefore the number $2S + 1$ is referred to as *multiplicity*. In the rare cases of $L \leqslant S$ the term would split into $2L + 1$ components, however by multiplicity one would nevertheless mean $2S + 1$. Depending on the multiplicity, terms are referred to as singlet, doublet, triplet and so on. Multiplicity of the term is usually shown as the left superscript of the term symbol ${}^{2S+1}L_J$ (see Fig. 5.1).

In general, there are $(2L + 1)(2S + 1)$ states included in one term ${}^{2S+1}L_J$ which differ from each other by values of M_L and M_S. Spin-orbit interaction cannot lift this degeneracy

fully, so all of the $2J+1$ states described by different M_J have the same energy. Obviously, applying SO coupling does not change the total amount of the states corresponding to a particular term:

$$\sum_J (2J+1) = (2S+1)(2L+1). \tag{5.18}$$

The degeneracy of M_J states can be further lifted by applying magnetic field.

It is important to note the order of the states. For a particular electronic configuration containing indistinguishable electrons according to the empirical Hund's rule the ground state is the one with the largest possible for this configuration value of the total spin S and the largest possible for this S value of the total orbital momentum L. If an electron configuration is less than half-filled (i.e. $n < 2l+1$), then the multiplets are ordered *normally*, i.e. the component with smallest possible value of $J = |L-S|$ has the smallest possible energy. If the filling is more than a half ($n > 2l+1$) then the lowest in energy level has the largest possible $J = L+S$ and the multiplets are addressed as *inverted*.

5.2.2. *jj* coupling scheme

In the *jj* coupling scheme, one assumes $\mathcal{H}_{\text{SOC}} > \mathcal{H}_{\text{res}}$ and takes $\mathcal{H}_{\text{SOC}}$ to be the strongest perturbation to $\mathcal{H}_{\text{CF}}$. In practice this means that L and S are not good quantum numbers anymore (i.e. they are not even forming good first order approximation to the unknown eingenbasis of the total Hamiltonian (5.10)) and the total **J** momentum has to be calculated as a sum of individual **j** momenta characterizing each electron. So, one has to first sum up the individual moments of one electron:

$$\mathbf{j}_i = \mathbf{l}_i + \mathbf{s}_i\,, \tag{5.19}$$

and then calculate the total momentum as

$$\mathbf{J} = \mathbf{j}_1 + \mathbf{j}_2 + ... \tag{5.20}$$

It is interesting to note that a mixed type of coupling takes place for atoms in highly exited states: while the atomic core is in Russel-Saunders state, the highly excited electron(s) are best described in *jj* coupling approximation [65]. This happens because an electron excited to a state with much higher principal number n is a subject to reduced electrostatic interaction due to the increased distance to the nucleus while the SO interaction does not depend on the distance and remains constant.

5.3. Multiplet structure of the t_{2g}^2 configuration: Ir atom

Calculating the ARPES spectral function for Sr_2IrO_4 amounts to calculating the Green's function of the hole introduced into the AF $j = 1/2$ ground state in the photoemission process (see chapter 3 for details). Since adding a hole (i.e. removing an electron) to the Ir^{4+} ion leads to the $5d^4$ configuration, we are interested in the multiplet structure of the latter. In the octahedral crystal field, the d shell splits into e_g and t_{2g} manifolds. Two holes residing on a site with d^4 configuration occupy the t_{2g} manifold with effective orbital momentum $l = 1$ per hole [1]. Therefore, the d^4 configuration effectively mimics the p^2 configuration (see Fig. 5.1) which was discussed in subsection 5.2.1.

Calculating the multiplet structure for a p^2 configuration depends on the coupling scheme. In the LS coupling scheme, it amounts to first summing up the **l** and **s** momenta of all the electrons and then summing up total **L** and total **S** momenta to a total **J**. In the *jj* coupling scheme, one first sum up individual **l** and **s** momenta for an electron and then calculating total $\mathbf{J} = \sum_i \mathbf{j}_i$. It is important to note that even if the complete Hilbert space is considered,

choice of the coupling scheme could have prominent consequences due to change in relative energy splittings and composition of the multiplets.

Such effects on the kinetic energy term of Hamiltonian (3.9), i.e. eq. (3.11) and its manifestation in theoretical ARPES and STS spectra are discussed in the following.

5.3.1. *LS* coupling scheme: high weight decomposition method

Let us start with the *LS* coupling scheme as used in chapter 3 and discuss it here in detail. We want to establish an unambiguous link between $|\alpha\sigma\rangle, |\alpha'\sigma'\rangle$ single particle basis (for two holes) and the final multiplet set $|S, M_S, L, M_L\rangle$ where $\alpha, \alpha' = xy, yz, xz$ indicate the orbitals occupied by the holes, and σ and σ' stands for their spins.

First, we make a basis transformation from the $|\alpha\sigma\rangle$ basis to the single-particle $|lsm_l m_s\rangle$ basis as described in section 1.5.

Secondly, we want to construct the basis transformation to arrive at the total L and S. In principle, one can try to use Clebsch-Gordan coefficients, however, one has to do it with caution: Clebsch-Gordan tables are formulated for summation of momenta of two *inequivalent* electrons. So, if we want to sum spins $\mathbf{s}_1$ and $\mathbf{s}_2$ of two electrons, they have to have some degree of freedom to differentiate between them. If they were on two different sites, then the position would do the job, if they are however on one site as in our case, they must reside on different orbitals in order to be correctly treated by Clebsch-Gordan coefficients. Let's say we want to calculate the total spin momenta of two electrons residing on one orbital (i.e. indistinguishable). We know that Pauli principle forbids any other state than one electron with spin up, another one with spin down. But according to CGC (see appendix B for the CGC table), two particles with $s = 1/2$, $s' = 1/2$ and $m_s = 1/2$, $m_{s'} = -1/2$ can form two different states. So, bearing this in mind we avoid using CGC for two-particle configurations and instead perform moment summation using the *high weight decomposition method*.

We start with the "high spin" state with the largest possible total spin $S = 1$ and highest possible $\mathbf{L}$ for this $\mathbf{S}$. Obviously, there are nine states with $S = 1$ and $L = 1$ which form the ^3P multiplet. From them we choose the one with the maximum projections M_L and M_S: $\psi_1^{LS} = |S\, M_S\, L\, M_L\rangle = |1\,1\,1\,1\rangle$. In terms of single-particle second quantization operators there is only one way this state can possibly be constructed:

$$\psi_1^{LS} = |1, 1, 1, 1\rangle = c^\dagger_{0\uparrow} c^\dagger_{1\uparrow} |0\rangle\,, \tag{5.21}$$

where $c^\dagger_{\alpha\sigma}$ is an operator creating an electron on the $l_{\text{eff}} = 1$ orbital with $m_l = \alpha$ and spin σ, and the vacuum state $|0\rangle$ is defined as empty t_{2g} shell. To construct the next possible state we employ a ladder operator $\hat{L}^-$:

$$\psi_2^{LS} = \hat{L}^- \psi_1^{LS}. \tag{5.22}$$

Using formula for the ladder operator known from textbooks (see for example Landau and Lifshitz [65])

$$\langle L, M_{L-1}|\, \hat{L}^-\, |L, M_L\rangle = \sqrt{(L + M_L)(L - M_L + 1)}, \tag{5.23}$$

and normalizing (5.22) we get

$$\psi_2^{LS} = |1\,1\,1\,0\rangle = c^\dagger_{-1\uparrow} c^\dagger_{1\uparrow} |0\rangle\,. \tag{5.24}$$

Now we can either apply $\hat{L}^-$ once more or employ spin ladder $\hat{S}^-$ operator instead. Let us look at the effect of the latter:

$$|1\,0\,1\,0\rangle = \hat{S}^- \psi_2^{LS} = \frac{1}{\sqrt{2}} \left(c^\dagger_{-1\downarrow} c^\dagger_{1\uparrow} + c^\dagger_{-1\uparrow} c^\dagger_{1\downarrow} \right) |0\rangle\,. \tag{5.25}$$

Having obtained all nine states of the ^3P multiplet in this way we proceed by searching for a state with the highest possible total orbital momentum. Since one has to place two electrons on the same orbital to get total orbital momentum $L = 2$, they must have opposite spins in order to obey Pauli's principle. This state thus has $L = 2$, $S = 0$ and belongs to ^1D quintet. Again, for the state with the highest possible momentum, be it orbital or spin, there is always one unique way to construct it:

$$\psi_{10}^{LS} = |0\,0\,2\,2\rangle = c_{1\downarrow}^\dagger c_{1\uparrow}^\dagger |0\rangle\,. \tag{5.26}$$

It is important on this step to keep operator ordering convention consistent with that used in (5.21). After we have obtained all five states of ^1D multiplet using ladder operators, we only need to find the last missing state: singlet ^1S (full list of multiplets forming for a particular electronic configuration can be found in many atomic physics book, see e.g. Table 2.1 in [102]). We know that ^1S state shall have $M_S = 0$ and $M_L = 0$, but we do not know what the quantum numbers L, S are. What we however know is that ^1S state has to be orthogonal to the other two states with $M_S = 0$ and $M_L = 0$, which are written as

$$\begin{aligned} |1\,0\,1\,0\rangle &= \frac{1}{\sqrt{2}}\left(c_{-1\downarrow}^\dagger c_{1\uparrow}^\dagger + c_{-1\uparrow}^\dagger c_{1\downarrow}^\dagger\right)|0\rangle\,, \\ |0\,0\,2\,0\rangle &= \frac{1}{\sqrt{6}}\left(c_{-1\downarrow}^\dagger c_{1\uparrow}^\dagger - c_{-1\uparrow}^\dagger c_{1\downarrow}^\dagger + 2c_{0\downarrow}^\dagger c_{0\uparrow}^\dagger\right)|0\rangle\,. \end{aligned} \tag{5.27}$$

Since there can be no other combination of two creation operators creating a state with both $M_S = 0$ and $M_L = 0$ other than the three used in (5.27) the missing state has to be a combination of them as well and simultaneously orthogonal to the two states in (5.27). Employing trivial linear algebra we get that the ^1S multiplet is written as

$$\psi_{15}^{LS} = |0\,0\,0\,0\rangle = \frac{1}{\sqrt{3}}\left(c_{-1\downarrow}^\dagger c_{1\uparrow}^\dagger - c_{-1\uparrow}^\dagger c_{1\downarrow}^\dagger - c_{0\downarrow}^\dagger c_{0\uparrow}^\dagger\right)|0\rangle\,. \tag{5.28}$$

Having obtained in this way all the states of new basis we can construct the matrix U_1 that transforms the Hamiltonian $\mathcal{H}_{ls}$ from the product state $|l\ s\ m_l\ m_s\rangle\,|l'\ s'\ m_l'\ m_s'\rangle$ basis to the total spin and orbital momentum $|L\ S\ M_L\ M_S\rangle$ basis:

$$\mathcal{H}_{LS-\text{basis}}^{LS} = U_1^\dagger \mathcal{H}_{ls-\text{basis}} U_1, \tag{5.29}$$

where

$$U_1 = \begin{pmatrix}
0 & 0 & 0 & 0 & 0 & 0 & 0 & 0 & 0 & 1 & 0 & 0 & 0 & 0 & 0 \\
1 & 0 & 0 & 0 & 0 & 0 & 0 & 0 & 0 & 0 & 0 & 0 & 0 & 0 & 0 \\
0 & 0 & 0 & \frac{1}{\sqrt{2}} & 0 & 0 & 0 & 0 & 0 & 0 & \frac{1}{\sqrt{2}} & 0 & 0 & 0 & 0 \\
0 & 1 & 0 & 0 & 0 & 0 & 0 & 0 & 0 & 0 & 0 & 0 & 0 & 0 & 0 \\
0 & 0 & 0 & 0 & \frac{1}{\sqrt{2}} & 0 & 0 & 0 & 0 & 0 & 0 & \frac{1}{\sqrt{6}} & 0 & 0 & \frac{1}{\sqrt{3}} \\
0 & 0 & 0 & \frac{1}{\sqrt{2}} & 0 & 0 & 0 & 0 & 0 & 0 & -\frac{1}{\sqrt{2}} & 0 & 0 & 0 & 0 \\
0 & 0 & 0 & 0 & 0 & 0 & 1 & 0 & 0 & 0 & 0 & 0 & 0 & 0 & 0 \\
0 & 0 & 0 & 0 & \frac{1}{\sqrt{2}} & 0 & 0 & 0 & 0 & 0 & 0 & -\frac{1}{\sqrt{6}} & 0 & 0 & -\frac{1}{\sqrt{3}} \\
0 & 0 & 0 & 0 & 0 & 0 & 0 & 1 & 0 & 0 & 0 & 0 & 0 & 0 & 0 \\
0 & 0 & 0 & 0 & 0 & 0 & 0 & 0 & 0 & 0 & 0 & \sqrt{\frac{2}{3}} & 0 & 0 & -\frac{1}{\sqrt{3}} \\
0 & 0 & 1 & 0 & 0 & 0 & 0 & 0 & 0 & 0 & 0 & 0 & 0 & 0 & 0 \\
0 & 0 & 0 & 0 & 0 & \frac{1}{\sqrt{2}} & 0 & 0 & 0 & 0 & 0 & 0 & \frac{1}{\sqrt{2}} & 0 & 0 \\
0 & 0 & 0 & 0 & 0 & \frac{1}{\sqrt{2}} & 0 & 0 & 0 & 0 & 0 & 0 & -\frac{1}{\sqrt{2}} & 0 & 0 \\
0 & 0 & 0 & 0 & 0 & 0 & 0 & 0 & 1 & 0 & 0 & 0 & 0 & 0 & 0 \\
0 & 0 & 0 & 0 & 0 & 0 & 0 & 0 & 0 & 0 & 0 & 0 & 0 & 1 & 0
\end{pmatrix}, \tag{5.30}$$

where the product state $|l\ s\ m_l\ m_s\rangle\,|l'\ s'\ m_l'\ m_s'\rangle$ basis is defined as

$$\hat{a} = \begin{pmatrix} 1 & 1 & 0 & 0 & 0 & 0 \\ 1 & 0 & 1 & 0 & 0 & 0 \\ 1 & 0 & 0 & 1 & 0 & 0 \\ 1 & 0 & 0 & 0 & 1 & 0 \\ 1 & 0 & 0 & 0 & 0 & 1 \\ 0 & 1 & 1 & 0 & 0 & 0 \\ 0 & 1 & 0 & 1 & 0 & 0 \\ 0 & 1 & 0 & 0 & 1 & 0 \\ 0 & 1 & 0 & 0 & 0 & 1 \\ 0 & 0 & 1 & 1 & 0 & 0 \\ 0 & 0 & 1 & 0 & 1 & 0 \\ 0 & 0 & 1 & 0 & 0 & 1 \\ 0 & 0 & 0 & 1 & 1 & 0 \\ 0 & 0 & 0 & 1 & 0 & 1 \\ 0 & 0 & 0 & 0 & 1 & 1 \end{pmatrix}, \tag{5.31}$$

where 1(0) means (un-)occupied state of the single particle Hilbert space defined by $|m_l m_s\rangle$ as $\{|1\uparrow\rangle, |1\downarrow\rangle, |0\uparrow\rangle, |0\downarrow\rangle, |-1\uparrow\rangle, |-1\downarrow\rangle\}$. The multiplet basis $|S\ M_S\ L\ M_L\rangle$ is defined as

$$\begin{aligned}\hat{A} =\{&|1\,1\,1\,1\rangle, |1\,1\,1\,0\rangle, |1\,1\,1\,-1\rangle, |1\,0\,1\,1\rangle, |1\,0\,1\,0\rangle, |1\,0\,1\,-1\rangle, |1\,-1\,1\,1\rangle, |1\,-1\,1\,0\rangle, \\ &|1\,-1\,1\,-1\rangle, |0\,0\,2\,2\rangle, |0\,0\,2\,1\rangle, |0\,0\,2\,0\rangle, |0\,0\,2\,-1\rangle, |0\,0\,2\,-2\rangle, |\,0\,0\,0\,0\rangle\},\end{aligned} \tag{5.32}$$

so that

$$\hat{A} = U_1 \hat{a}. \tag{5.33}$$

After employing this transformation, we have effectively taken Hamiltonian (5.14) that defines the first-order corrections to the eigenstates of the system into account. As discussed in section 5.2.1, according to Hund's rules the state with the lowest energy is the one with the highest multiplicity and the highest possible **L**, i.e. in the first approximation the ground state is the nine-fold degenerate ^3P multiplet.

To account for further perturbations on the system, which in case of the LS coupling scheme is the on-site spin-orbit coupling (5.11), we now have to go to the basis of total **J** momenta. We truncate our Hilbert space down to the high spin ^3P states only because we are building the low-energy effective model. Since total spin $S = 1$ and orbital momenta $L = 1$ are distinguishable by their nature, we can simply use the CG coefficients to sum them up:

$$U_2 = \begin{pmatrix} 0 & 0 & 0 & 0 & 1 & 0 & 0 & 0 & 0 \\ 0 & \frac{1}{\sqrt{2}} & 0 & 0 & 0 & \frac{1}{\sqrt{2}} & 0 & 0 & 0 \\ \frac{1}{\sqrt{3}} & 0 & \frac{1}{\sqrt{2}} & 0 & 0 & 0 & \frac{1}{\sqrt{6}} & 0 & 0 \\ 0 & -\frac{1}{\sqrt{2}} & 0 & 0 & 0 & \frac{1}{\sqrt{2}} & 0 & 0 & 0 \\ -\frac{1}{\sqrt{3}} & 0 & 0 & 0 & 0 & 0 & \sqrt{\frac{2}{3}} & 0 & 0 \\ 0 & 0 & 0 & \frac{1}{\sqrt{2}} & 0 & 0 & 0 & \frac{1}{\sqrt{2}} & 0 \\ \frac{1}{\sqrt{3}} & 0 & -\frac{1}{\sqrt{2}} & 0 & 0 & 0 & \frac{1}{\sqrt{6}} & 0 & 0 \\ 0 & 0 & 0 & -\frac{1}{\sqrt{2}} & 0 & 0 & 0 & \frac{1}{\sqrt{2}} & 0 \\ 0 & 0 & 0 & 0 & 0 & 0 & 0 & 0 & 1 \end{pmatrix}, \tag{5.34}$$

arriving at the final Hamiltonian

$$\mathcal{H}^{LS}_{J-\text{basis}} = U_2^\dagger \mathcal{H}^{LS}_{LS-\text{basis}} U_2\,, \tag{5.35}$$

where $\mathcal{H}^{LS}_{J-\text{basis}}$ is written in the spin-orbit coupled basis

$$\hat{J} = \{S, T_1, T_0, T_{-1}, M_2, M_1, M_0, M_{-1}, M_{-2}\}\,, \tag{5.36}$$

which consists of the lowest $J = 0$ singlet S, the higher $J = 1$ triplets T_σ ($\sigma = -1, 0, 1$, split by energy λ from the singlet state) and $J = 2$ quintets (see section 3.3.3 and Fig. 3.1 for detailed explanation).

To build an effective low-energy model we further truncate the Hilbert space and reduce the basis set to the two lowest multiplets $^3P_0$ and $^3P_1$ (see Fig 5.1):

$$\hat{J} = \{S, T_1, T_0, T_{-1}\}\,. \tag{5.37}$$

We note that reducing the Hilbert space down to $J = 0$ and $J = 1$ states is a well justified physical cutoff since we are interested in the low-energy physics. However, mathematically such a basis is incomplete, and a proper basis transformation between the product state basis (Eq. 5.31) and multiplet basis (Eq. 5.32) can not be defined. Therefore we have considered the full set of 15 configurations formed by two holes residing on the xy, yz and xz orbitals while deriving transformations (5.30,5.34) and have implemented the cutoff only after we arrived at the final basis set which is a good approximation to the eigenstates of the full Hamiltonian.

5.3.2. *jj* coupling scheme

We now derive the basis transformation to connect Hamiltonian in the $|\alpha\sigma\rangle\,, |\alpha'\sigma'\rangle$ independent particle basis to the Hamiltonian defined in the basis of the total momenta $\mathbf{J}$ in the jj coupling scheme. First, we use CGC to sum up the total momenta on each site

$$c^\dagger_{0\uparrow} c^\dagger_{1\uparrow} |0\rangle \to \left(\sqrt{\frac{2}{3}} \left|\frac{3}{2}\frac{1}{2}\right\rangle - \sqrt{\frac{1}{3}} \left|\frac{1}{2}\frac{1}{2}\right\rangle\right) \left(\left|\frac{3}{2}\frac{3}{2}\right\rangle\right), \tag{5.38}$$

where the latter is written in the $|j\ m_j\rangle$ spin-orbit coupled single-particle basis. Since we perform CG summation here independently for both electrons, we have to take Pauli principle into account manually by projecting out forbidden states by hand. In the end, we arrive at the following matrix:

$$U_3 = \begin{pmatrix}
0 & -\sqrt{\frac{2}{3}} & 0 & 0 & 0 & 0 & 0 & 0 & 0 & \frac{1}{\sqrt{3}} & 0 & 0 & 0 & 0 & 0 \\
0 & \frac{1}{\sqrt{3}} & 0 & 0 & 0 & 0 & 0 & 0 & 0 & \sqrt{\frac{2}{3}} & 0 & 0 & 0 & 0 & 0 \\
0 & 0 & -\frac{1}{\sqrt{3}} & 0 & 0 & 0 & 0 & 0 & 0 & 0 & \sqrt{\frac{2}{3}} & 0 & 0 & 0 & 0 \\
0 & 0 & \sqrt{\frac{2}{3}} & 0 & 0 & 0 & 0 & 0 & 0 & 0 & \frac{1}{\sqrt{3}} & 0 & 0 & 0 & 0 \\
0 & 0 & 0 & 0 & 0 & 0 & 0 & 0 & 0 & 0 & 0 & 0 & 1 & 0 & 0 \\
0 & 0 & 0 & 1 & 0 & 0 & 0 & 0 & 0 & 0 & 0 & 0 & 0 & 0 & 0 \\
\frac{\sqrt{2}}{3} & 0 & 0 & 0 & -\frac{1}{3} & \frac{2}{3} & 0 & 0 & 0 & 0 & 0 & \frac{\sqrt{2}}{3} & 0 & 0 & 0 \\
-\frac{2}{3} & 0 & 0 & 0 & \frac{\sqrt{2}}{3} & \frac{\sqrt{2}}{3} & 0 & 0 & 0 & 0 & 0 & \frac{1}{3} & 0 & 0 & 0 \\
0 & 0 & 0 & 0 & 0 & 0 & 0 & \sqrt{\frac{2}{3}} & 0 & 0 & 0 & 0 & 0 & \frac{1}{\sqrt{3}} & 0 \\
-\frac{1}{3} & 0 & 0 & 0 & -\frac{\sqrt{2}}{3} & -\frac{\sqrt{2}}{3} & 0 & 0 & 0 & 0 & 0 & \frac{2}{3} & 0 & 0 & 0 \\
\frac{\sqrt{2}}{3} & 0 & 0 & 0 & \frac{2}{3} & -\frac{1}{3} & 0 & 0 & 0 & 0 & 0 & \frac{\sqrt{2}}{3} & 0 & 0 & 0 \\
0 & 0 & 0 & 0 & 0 & 0 & 0 & -\frac{1}{\sqrt{3}} & 0 & 0 & 0 & 0 & 0 & \sqrt{\frac{2}{3}} & 0 \\
0 & 0 & 0 & 0 & 0 & 0 & 1 & 0 & 0 & 0 & 0 & 0 & 0 & 0 & 0 \\
0 & 0 & 0 & 0 & 0 & 0 & 0 & 0 & \frac{1}{\sqrt{3}} & 0 & 0 & 0 & 0 & 0 & \sqrt{\frac{2}{3}} \\
0 & 0 & 0 & 0 & 0 & 0 & 0 & 0 & -\sqrt{\frac{2}{3}} & 0 & 0 & 0 & 0 & 0 & \frac{1}{\sqrt{3}}
\end{pmatrix}, \tag{5.39}$$

which is to be used as

$$\mathcal{H}^{jj}_{jj-\text{basis}} = U_3^{\dagger}\mathcal{H}^{jj}_{ls-\text{basis}}U_3 \tag{5.40}$$

to transform the Hamiltonian from the basis (5.31) into the individual j basis $|j\, m_j\, j'\, m_{j'}\rangle$:

$$\begin{aligned}\hat{j} =\{ &\left|\tfrac{1}{2}\,-\tfrac{1}{2}\,\tfrac{1}{2},\tfrac{1}{2}\right\rangle, \left|\tfrac{3}{2}\,\tfrac{3}{2}\,\tfrac{1}{2},\tfrac{1}{2}\right\rangle, \left|\tfrac{3}{2}\,\tfrac{3}{2}\,\tfrac{1}{2},-\tfrac{1}{2}\right\rangle, \left|\tfrac{3}{2}\,\tfrac{1}{2}\,\tfrac{1}{2},\tfrac{1}{2}\right\rangle, \left|\tfrac{3}{2}\,\tfrac{1}{2}\,\tfrac{1}{2},-\tfrac{1}{2}\right\rangle, \left|\tfrac{3}{2}\,-\tfrac{1}{2}\,\tfrac{1}{2},\tfrac{1}{2}\right\rangle,\\ &\left|\tfrac{3}{2}\,-\tfrac{1}{2}\,\tfrac{1}{2},-\tfrac{1}{2}\right\rangle, \left|\tfrac{3}{2}\,-\tfrac{3}{2}\,\tfrac{1}{2}\,\tfrac{1}{2}\right\rangle, \left|\tfrac{3}{2}\,-\tfrac{3}{2}\,\tfrac{1}{2},-\tfrac{1}{2}\right\rangle, \left|\tfrac{3}{2}\,\tfrac{1}{2}\,\tfrac{3}{2}\,\tfrac{3}{2}\right\rangle, \left|\tfrac{3}{2}\,-\tfrac{1}{2}\,\tfrac{3}{2},\tfrac{3}{2}\right\rangle,\\ &\left|\tfrac{3}{2}\,-\tfrac{1}{2}\,\tfrac{3}{2}\,\tfrac{1}{2}\right\rangle, \left|\tfrac{3}{2}\,-\tfrac{3}{2}\,\tfrac{3}{2},\tfrac{3}{2}\right\rangle, \left|\tfrac{3}{2}\,-\tfrac{3}{2}\,\tfrac{3}{2}\,\tfrac{1}{2}\right\rangle, \left|\tfrac{3}{2}\,-\tfrac{3}{2}\,\tfrac{3}{2},-\tfrac{1}{2}\right\rangle\}.\end{aligned} \tag{5.41}$$

We employ now the high weight decomposition method introduced in section 5.3.1 in order to obtain Hamiltonian (5.40) in the total J basis:

$$\begin{aligned}\hat{J} =\{&S^{(\frac{1}{2},\frac{1}{2})}, T_1^{(\frac{3}{2},\frac{1}{2})}, T_0^{(\frac{3}{2},\frac{1}{2})}, T_{-1}^{(\frac{3}{2},\frac{1}{2})}, M_2^{(\frac{3}{2},\frac{1}{2})}, M_1^{(\frac{3}{2},\frac{1}{2})}, M_0^{(\frac{3}{2},\frac{1}{2})}, M_{-1}^{(\frac{3}{2},\frac{1}{2})},\\ &M_{-2}^{(\frac{3}{2},\frac{1}{2})}, S^{(\frac{3}{2},\frac{3}{2})}, M_2^{(\frac{3}{2},\frac{3}{2})}, M_1^{(\frac{3}{2},\frac{3}{2})}, M_0^{(\frac{3}{2},\frac{3}{2})}, M_{-1}^{(\frac{3}{2},\frac{3}{2})}, M_{-2}^{(\frac{3}{2},\frac{3}{2})}\},\end{aligned} \tag{5.42}$$

where S is singlet state, T_α represents a triplet state with $J=1$, $J_z=\alpha$, M_α signifies a triplet state with $J=2$, $J_z=\alpha$ and the superscript stands for (j_1, j_2). Basis (5.42) is equivalent to (5.36) when cut down to the lowest 9 states and to (5.37) upon further truncation to lowest 4 states. We start from the state with highest possible $M_J = 2$. The state with the highest total momenta $J=2$ can be constructed either by placing one electron on the $j=\frac{3}{2}$ state with energy $\lambda = \xi/2$ and one electron on the $\frac{1}{2}$ state or by placing two electrons on $j=\frac{3}{2}$ quartets both having energy $\lambda=\xi/2$ so that a two-particle state has energy $\lambda=\xi$. Let us start with a state that is lower in energy

$$\psi_5^{jj} = |J=2\; M_J=2\rangle^{(\frac{3}{2},\frac{1}{2})} = \left|\frac{3}{2}\,\frac{3}{2}\,\frac{1}{2}\,\frac{1}{2}\right\rangle. \tag{5.43}$$

Applying ladder operator J^- and normalizing the result we obtain the next state

$$\psi_6^{jj} = |J=2\; M_J=1\rangle^{(\frac{3}{2},\frac{1}{2})} = \frac{\sqrt{3}}{2}\left|\frac{3}{2}\,\frac{1}{2}\,\frac{1}{2}\,\frac{1}{2}\right\rangle + \frac{1}{2}\left|\frac{3}{2}\,\frac{3}{2}\,\frac{1}{2}\,-\frac{1}{2}\right\rangle. \tag{5.44}$$

Once we have obtained five possible $J=2$ states we consider the other $|J=2\; M_J=1\rangle$ configuration formed by two electrons in the $j=\frac{3}{2}$ quartet:

$$\psi_{11}^{jj} = |J=2\; M_J=2\rangle^{(\frac{3}{2},\frac{3}{2})} = \left|\frac{3}{2}\,\frac{1}{2}\,\frac{3}{2}\,\frac{1}{2}\right\rangle. \tag{5.45}$$

Note that once chosen, the ordering convention has to be followed since fermionic operators anticommute.

We perform the rest of the derivation analogously to that in section 5.3.1 and arrive at the

basis transformation

$$U_4 = \begin{pmatrix}
1 & 0 & 0 & 0 & 0 & 0 & 0 & 0 & 0 & 0 & 0 & 0 & 0 & 0 & 0 \\
0 & 0 & 0 & 0 & 1 & 0 & 0 & 0 & 0 & 0 & 0 & 0 & 0 & 0 & 0 \\
0 & \frac{\sqrt{3}}{2} & 0 & 0 & 0 & \frac{1}{2} & 0 & 0 & 0 & 0 & 0 & 0 & 0 & 0 & 0 \\
0 & -\frac{1}{2} & 0 & 0 & 0 & \frac{\sqrt{3}}{2} & 0 & 0 & 0 & 0 & 0 & 0 & 0 & 0 & 0 \\
0 & 0 & \frac{1}{\sqrt{2}} & 0 & 0 & 0 & \frac{1}{\sqrt{2}} & 0 & 0 & 0 & 0 & 0 & 0 & 0 & 0 \\
0 & 0 & -\frac{1}{\sqrt{2}} & 0 & 0 & 0 & \frac{1}{\sqrt{2}} & 0 & 0 & 0 & 0 & 0 & 0 & 0 & 0 \\
0 & 0 & 0 & \frac{1}{2} & 0 & 0 & 0 & \frac{\sqrt{3}}{2} & 0 & 0 & 0 & 0 & 0 & 0 & 0 \\
0 & 0 & 0 & -\frac{\sqrt{3}}{2} & 0 & 0 & 0 & \frac{1}{2} & 0 & 0 & 0 & 0 & 0 & 0 & 0 \\
0 & 0 & 0 & 0 & 0 & 0 & 0 & 0 & 1 & 0 & 0 & 0 & 0 & 0 & 0 \\
0 & 0 & 0 & 0 & 0 & 0 & 0 & 0 & 0 & 0 & 1 & 0 & 0 & 0 & 0 \\
0 & 0 & 0 & 0 & 0 & 0 & 0 & 0 & 0 & 0 & 0 & 1 & 0 & 0 & 0 \\
0 & 0 & 0 & 0 & 0 & 0 & 0 & 0 & 0 & -\frac{1}{\sqrt{2}} & 0 & 0 & \frac{1}{\sqrt{2}} & 0 & 0 \\
0 & 0 & 0 & 0 & 0 & 0 & 0 & 0 & 0 & \frac{1}{\sqrt{2}} & 0 & 0 & \frac{1}{\sqrt{2}} & 0 & 0 \\
0 & 0 & 0 & 0 & 0 & 0 & 0 & 0 & 0 & 0 & 0 & 0 & 0 & 1 & 0 \\
0 & 0 & 0 & 0 & 0 & 0 & 0 & 0 & 0 & 0 & 0 & 0 & 0 & 0 & 1
\end{pmatrix}. \tag{5.46}$$

The final Hamiltonian than can be obtained as

$$\mathcal{H}^{jj}_{JJ-\text{basis}} = U_4^\dagger \mathcal{H}^{jj}_{jj-\text{basis}} U_4. \tag{5.47}$$

5.4. Manifestation of the coupling scheme in the *t-J* model

Naturally, once having obtained the kinetic part of the *t-J* model (3.9) in *LS* (Hamiltonian (5.35)) and *jj* (Hamiltonian (5.47)) coupling schemes, one would want to check if there are any differences and if so then how dramatic are they. Applying basis transformations in the *LS* coupling approximation from section 5.3.1 to the Hamiltonian derived from Eq. (3.8) as $\langle 5d^4_{\mathbf{i}}\, 5d^5_{\mathbf{j}} | \mathcal{H}_{\text{TB}} | 5d^5_{\mathbf{i}}\, 5d^4_{\mathbf{j}} \rangle$ followed by slave-fermion, Holstein-Primakoff, Fourier, and Bogoliubov transformations one arrives at Hamiltonian (3.11), see section 3.3.3 for details. In similar fashion we derive the kinetic Hamiltonian using basis transformation derived within *jj* coupling approximation in section 5.3.2:

$$\mathcal{H}^{j-j}_{\text{t}} = \sum_{\mathbf{k}} \left(\mathbf{h}^\dagger_{\mathbf{k}\text{A}} \hat{W}^0_{\mathbf{k}} \mathbf{h}_{\mathbf{k}\text{A}} + \mathbf{h}^\dagger_{\mathbf{k}\text{B}} \hat{W}^0_{\mathbf{k}} \mathbf{h}_{\mathbf{k}\text{B}} \right) + \sum_{\mathbf{k},\mathbf{q}} \left(\mathbf{h}^\dagger_{\mathbf{k}-\mathbf{q}\text{B}} \hat{W}^\alpha_{\mathbf{k},\mathbf{q}} \mathbf{h}_{\mathbf{k}\text{B}} \alpha^\dagger_{\mathbf{q}} + \mathbf{h}^\dagger_{\mathbf{k}-\mathbf{q}\text{A}} \hat{W}^\beta_{\mathbf{k},\mathbf{q}} \mathbf{h}_{\mathbf{k}\text{B}} \beta^\dagger_{\mathbf{q}} + \text{h.c.} \right). \tag{5.48}$$

One can see that it has similar structure to Hamiltonian (3.11), however the terms $\hat{W}^0_{\mathbf{k}}$ describing the nearest, next nearest, and third neighbor free hopping, and the vertices $\hat{W}^\alpha_{\mathbf{k},\mathbf{q}}$ and $\hat{W}^\beta_{\mathbf{k},\mathbf{q}}$ describing the polaronic hopping are different from $\hat{V}^0_{\mathbf{k}}$, $\hat{V}^\alpha_{\mathbf{k},\mathbf{q}}$ and $\hat{V}^\beta_{\mathbf{k},\mathbf{q}}$ in Eqs. (3.12 – 3.14). The free hopping matrix now reads

$$\hat{W}^0_{\mathbf{k}} = \begin{pmatrix}
\frac{3}{2}F_1 & 0 & -\sqrt{\frac{3}{2}}F_2 & 0 & 0 & \sqrt{\frac{3}{2}}P_2 & 0 & -\sqrt{\frac{3}{2}}P_1 \\
0 & F_4 & 0 & 0 & \sqrt{\frac{3}{2}}P_1 & 0 & Q_1 & 0 \\
-\sqrt{\frac{3}{2}}F_2 & 0 & F_3 & 0 & 0 & Q_2 & 0 & Q_1 \\
0 & 0 & 0 & 0 & -\sqrt{\frac{3}{2}}P_2 & 0 & Q_2 & 0 \\
0 & \sqrt{\frac{3}{2}}P_1 & 0 & -\sqrt{\frac{3}{2}}P_2 & \frac{3}{2}F_1 & 0 & \sqrt{\frac{3}{2}}F_2 & 0 \\
\sqrt{\frac{3}{2}}P_2 & 0 & Q_2 & 0 & 0 & 0 & 0 & 0 \\
0 & Q_1 & 0 & Q_2 & \sqrt{\frac{3}{2}}F_2 & 0 & F_3 & 0 \\
-\sqrt{\frac{3}{2}}P_1 & 0 & Q_1 & 0 & 0 & 0 & 0 & F_4
\end{pmatrix}, \tag{5.49}$$

while the matrices containing vertices are

$$\hat{W}^{\alpha}_{\mathbf{k},\mathbf{q}} = \begin{pmatrix} 0 & \sqrt{\frac{3}{2}}L_3 & 0 & -\sqrt{\frac{3}{2}}L_3 & \frac{3}{2}Y_1 & 0 & -\sqrt{\frac{3}{2}}W_2 & 0 \\ \sqrt{\frac{3}{2}}L_3 & 0 & L_1 & 0 & 0 & Y_4 & 0 & W_1 \\ 0 & L_1 & 0 & L_1 & -\sqrt{\frac{3}{2}}W_2 & 0 & Y_2 & 0 \\ -\sqrt{\frac{3}{2}}L_3 & 0 & L_1 & 0 & 0 & W_1 & 0 & Y_3 \\ 0 & 0 & 0 & 0 & 0 & \sqrt{\frac{3}{2}}L_4 & 0 & -\sqrt{\frac{3}{2}}L_4 \\ 0 & 0 & 0 & 0 & \sqrt{\frac{3}{2}}L_4 & 0 & L_2 & 0 \\ 0 & 0 & 0 & 0 & 0 & L_2 & 0 & L_2 \\ 0 & 0 & 0 & 0 & -\sqrt{\frac{3}{2}}L_4 & 0 & L_2 & 0 \end{pmatrix}, \quad (5.50)$$

and

$$\hat{W}^{\beta}_{\mathbf{k},\mathbf{q}} = \begin{pmatrix} 0 & \sqrt{\frac{3}{2}}L_4 & 0 & -\sqrt{\frac{3}{2}}L_4 & 0 & 0 & 0 & 0 \\ \sqrt{\frac{3}{2}}L_4 & 0 & L_2 & 0 & 0 & 0 & 0 & 0 \\ 0 & L_2 & 0 & L_2 & 0 & 0 & 0 & 0 \\ -\sqrt{\frac{3}{2}}L_4 & 0 & L_2 & 0 & 0 & 0 & 0 & 0 \\ \frac{3}{2}Y_1 & 0 & \sqrt{\frac{3}{2}}W_2 & 0 & 0 & \sqrt{\frac{3}{2}}L_3 & 0 & -\sqrt{\frac{3}{2}}L_3 \\ 0 & Y_3 & 0 & W_1 & \sqrt{\frac{3}{2}}L_3 & 0 & L_1 & 0 \\ \sqrt{\frac{3}{2}}W_2 & 0 & Y_2 & 0 & 0 & L_1 & 0 & L_1 \\ 0 & W_1 & 0 & Y_4 & -\sqrt{\frac{3}{2}}L_3 & 0 & L_1 & 0 \end{pmatrix}. \quad (5.51)$$

The matrices are written in the basis (5.37) where additionally the sublattice index A/B accounting for the AF order has been introduced:

$$\hat{J} = \{S_{\mathrm{A}}, T_{1\mathrm{A}}, T_{0\mathrm{A}}, T_{-1\mathrm{A}}, S_{\mathrm{B}}, T_{1\mathrm{B}}, T_{0\mathrm{B}}, T_{-1\mathrm{B}}\}. \quad (5.52)$$

Comparing Eqs (5.49 – 5.51) with Eqs. (3.12 – 3.14) one can see directly that changing the coupling scheme results in renormalization of free-polaron dispersion $\hat{W}^{0}_{\mathbf{k}}$ and vertices $\hat{W}^{\alpha}_{\mathbf{k},\mathbf{q}}$ and $\hat{W}^{\beta}_{\mathbf{k},\mathbf{q}}$, in particular of those entries in the matrix that describe propagation of the polaron with a singlet $S_{\mathrm{A,B}}$ character. The coupling scheme seem to have a particular way of manifesting itself in the structure of the t-J model: each term of kinetic Hamiltonian (3.11) containing $h^{\dagger}_{\mathrm{S\,(A,B)}}$ ($h_{\mathrm{S\,(A,B)}}$) operator gets a factor of $\sqrt{\frac{3}{2}}$ while those containing two of singlet creation (annihilation) operators get a factor of $\frac{3}{2}$.

Actually, there is a mixing of the two $J = 0$ states $^3P_0$ and $^1S_0$ as one goes from the LS to the jj limit which explains the observed renormalization. This mixing is shown schematically in Fig. 5.1 with dotted lines. One knows that the coupling scheme can not result in the change of the number of multiplets or appearance of new multiplets so there exists a misconception that the coupling scheme cannot influence the eigenstates of the system at all. However, the choice of the coupling scheme can have interesting consequences for the low-energy effective model.

In fact, the same renormalization effect would be also observed for a hole in the material with $t^1_{2\mathrm{g}}$ configuration in ground state and strong on-site SOC for any geometry and choice of hopping parameters (see Fig. 3.2). For example, deriving a t-J model for a honeycomb iridates with one hole which forms the many-body d^4 configurations as well, one would get the same renormalization of the kinetic Hamiltonian when going from LS to jj limit, even though the motion of free charge on the honeycomb lattice is described by a completely different TB

model: the hoppings between different orbitals are much larger than the hoppings between the same ones and they are moreover strongly bond-dependent [34].

Naturally, there will be a mixing between the two $J = 2$ states, ${}^1D_2$ and ${}^3P_2$, as well. However, we do not consider it here in detail since we are not interested in the higher energy levels. It is also omitted from Fig. 5.1 for clarity.

In fact, the correspondence between the multiplets $\psi^{LS}_{S\,L\,J\,M_J}$ and $\psi^{jj}_{j\,j'\,J\,M_J}$ obtained within the LS and jj coupling schemes can generally be described as [102]:

$$\psi^{jj}_{J\,M_J\,j\,j'} = \sum_{L,S} \left(ss'[S]ll'[L]J|sl[j]s'l'[j']J\right) \psi^{LS}_{S\,M_S\,L\,M_L}. \tag{5.53}$$

Since the transition between LS and the jj coupling scheme is a change of the scheme of summation of four angular momenta, transformation coefficients in (5.53) can be expressed in terms of $9j$ symbols [102]:

$$\begin{aligned}\left(ss'[S]ll'[L]J|sl[j]s'l'[j']J\right) &= (-1)^{S+L-J+s+l-j+s'+l'-j'} \left(ll'[L]ss'[S]J|ls[j]l's'[j']J\right) = \\ &= \sqrt{(2S+1)\,(2L+1)\,(2j+1)\,(2j'+1)} \begin{Bmatrix} l & l' & L \\ j & j' & J \\ \frac{1}{2} & \frac{1}{2} & S \end{Bmatrix}. \end{aligned} \tag{5.54}$$

The values of the factor

$$\begin{Bmatrix} l & l' & L \\ j & j' & J \\ \frac{1}{2} & \frac{1}{2} & S \end{Bmatrix} = A\left(SLJ;\, jj'J\right) \tag{5.55}$$

are given, for example, in table (5.23) of Ref. [102] or in Ref. [75].

Calculating the transformation coefficients (5.54), although straightforward, may demand tedious computations. Let us, however, explicitly calculate how $\psi^{jj}_{0\,0\,\frac{1}{2}\,\frac{1}{2}}$ transforms into the $\psi^{L-S}_{S\,L\,J\,M_J}$ basis to understand the renormalization we observed in Eqs. (5.49 – 5.51):

$$\psi^{jj}_{0\,0\,\frac{1}{2}\,\frac{1}{2}} = \sqrt{(2S+1)\,(2L+1)\left(2\cdot\frac{1}{2}+1\right)\left(2\cdot\frac{1}{2}+1\right)} \cdot A\left(S\;L\;0;\;0\;0\;0\right). \tag{5.56}$$

Using table (5.23) of [102] we calculate the values of $A\left(S\;L\;0;\;0\;0\;0\right)$ and arrive at

$$\psi^{jj}_{0\,0\,\frac{1}{2}\,\frac{1}{2}} = \frac{1}{\sqrt{3}}\psi^{L-S}_{0\,0\,0\,0} + \sqrt{\frac{2}{3}}\psi^{LS}_{1\,1\,0\,0}, \tag{5.57}$$

i.e.

$$\psi^{jj}_{0\,0\,\frac{1}{2}\,\frac{1}{2}} = \frac{1}{\sqrt{3}}\psi\left({}^1S_0\right) + \sqrt{\frac{2}{3}}\psi\left({}^3P_0\right). \tag{5.58}$$

Indeed, the singlet state in the jj coupling scheme gets only $\sqrt{\frac{2}{3}}$ of the spectral weight of the singlet derived in the LS coupling scheme. This renormalization is compensated by the $\sqrt{\frac{3}{2}}$ factors arising in Eqs. (5.49 – 5.51). The physical consequences of this renormalization we will see in the next section where the theoretical ARPES spectra for Sr_2IrO_4 will be explored in both coupling schemes.

5.5. Influence of the coupling scheme choice on the Sr_2IrO_4 theoretical spectral function

Having obtained the vertices Eqs. (5.49 – 5.51) describing the propagation of the polaron in Sr_2IrO_4, we can now calculate the Green's functions of the polaron and plot its spectral

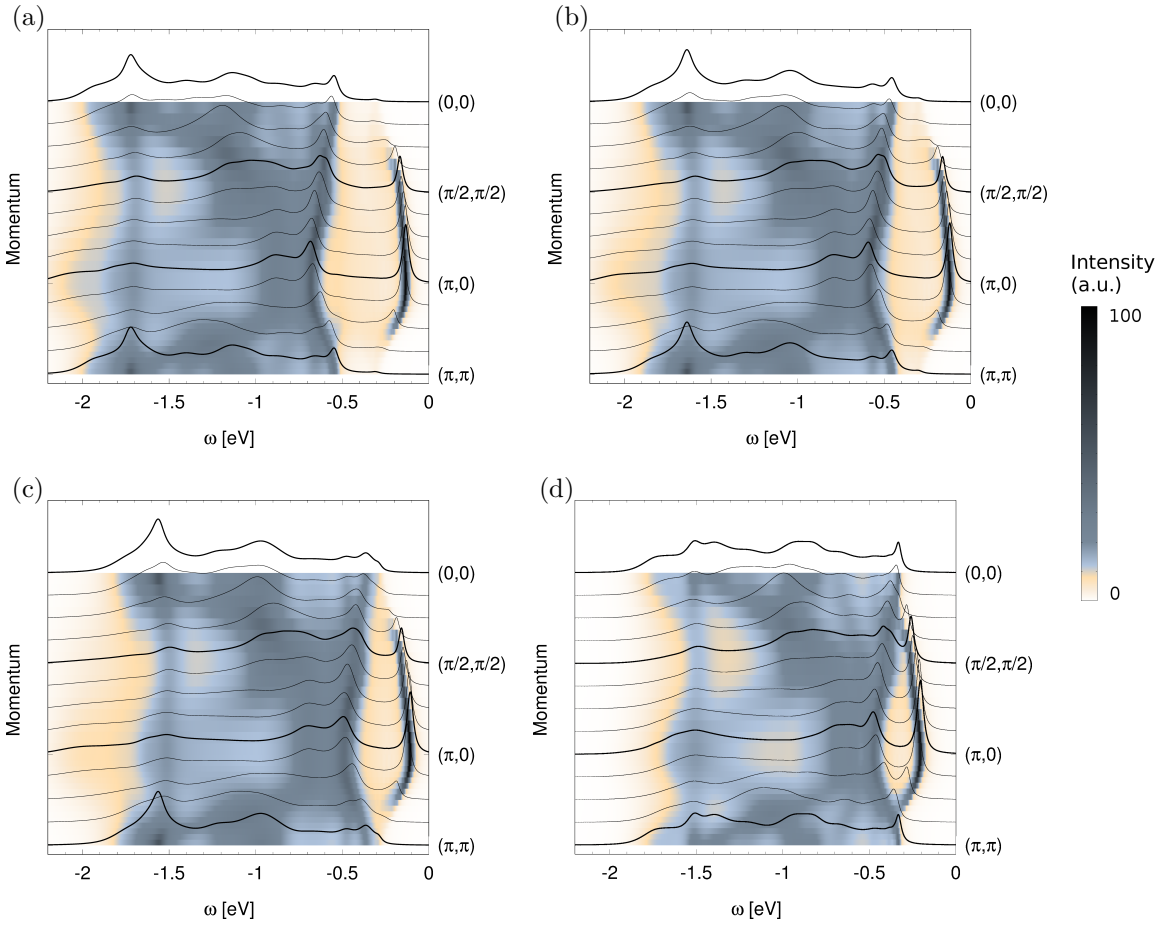

Figure 5.2.: Theoretical PES spectral function of the low-energy (polaronic) models developed for the square-lattice iridates within the *jj* coupling scheme and solved using the self-consistent Born approximation. The value of Coulomb splitting Δ varies so that singlet-triplet splitting $\lambda - 5/8\Delta$ is (a) λ, (b) 0.5λ, (c) 0.25λ. Spectral function calculated within the *LS* coupling scheme is shown on (d) for comparison (see also Fig. 3.3). Here spin-orbit coupling $\lambda = \xi/2$ where one-particle SOC $\xi = 0.382$ eV following Ref. [58]; hopping integrals calculated as the best fit to the density functional theory (DFT) band structure as discussed in section 3.3.2: $t_1 = -0.2239$ eV, $t_2 = -0.373$ eV, $t' = -0.1154$ eV, $t_3 = -0.0592$ eV, $t'' = -0.0595$ eV; spectra offset by (a)–(c) $E = -0.97$ eV, (c) $E = -0.77$ eV; broadening $\delta = 0.01$ eV.

function whithin SCBA. The only remaining problem is that we do not know the exact value of splitting Δ between $\psi^{jj}_{1\,\mathrm{M}\,\frac{1}{2}\,\frac{3}{2}}$ and $\psi^{jj}_{2\,\mathrm{M}'\,\frac{1}{2}\,\frac{3}{2}}$ (see Fig. 5.1) which depends on the Hund's coupling J_H. Therefore, we take Δ as a free parameter and perform calculations for four values of Δ such that the value of singlet-triplet splitting $\lambda - 5/8\Delta$ takes values between λ and $\lambda/4$ (see Fig. 5.2).

There have been plenty of ARPES experiments recently revealing the shape of the iridate spectral functions [12, 16, 54, 61, 69, 83, 109, 113, 123], see chapter 3 for more details. Upon comparison with the experiment, one can see that the experimentally observed maximum at Γ point at $0.35-0.45$ eV below Fermi level is not present on the theoretical spectral function calculated within the *jj* coupling for any choice of Coulomb Δ. However, as Δ increases, the comparison becomes better. One could expect that for Δ larger than λ, comparison would be even better, however in this case using the *jj* coupling scheme is not applicable anymore and

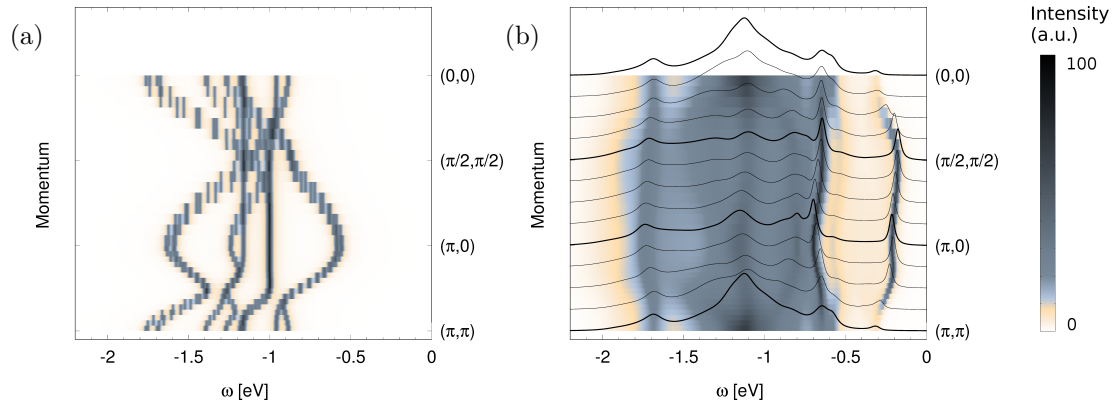

Figure 5.3.: Free and polaronic contributions to the spectrum in Fig. 5.2(a). (a) Theoretical photoemission spectral function with only propagation of the hole not coupled to magnons allowed as achieved by setting $\hat{W}^{\alpha}_{\mathbf{k}} = \hat{W}^{\beta}_{\mathbf{k}} \equiv 0$. (b) Theoretical photoemission spectral function with only polaronic propagation via coupling to magnons allowed (i.e. no free dispersion) as achieved by setting $\hat{W}^{0}_{\mathbf{k}} \equiv 0$. Parameters as in Fig. 5.2.

the *LS* coupling scheme has to be used instead. Indeed, comparing Fig. 5.2(d) obtained for a *t-J* model derived within *LS* coupling scheme to the experiment we note excellent agreement.

It is interesting to note, that most prominent changes in the spectral function within the *jj* coupling scheme is the larger relative shift of the quasiparticle peak. Although this depends on the singlet-triplet splitting, it is not fully defined by it. Thus, even in the case of unrealistically small gap of $\lambda/4$ (shown in Fig. 5.2(c)) one observes significant band shifting as compared to the spectral function calculated within the *LS* coupling scheme (Fig. 5.2(d)). In fact, the significant shift of the quasiparticle peak can be understood as an effect of the renormalization of the polaronic coupling discussed in section 5.4. As can be seen in Fig. 5.3 the coupling scheme has a stronger influence on the polaronic part of the spectra (Fig. 5.3(a)) rather than on the free part (Fig. 5.3(b)). Indeed, the hole of a singlet character has a biggest contribution to the low-energy band (see Fig. 5.4) and when the strength of its coupling to magnons is increased by a factor of $\frac{3}{2}$, the band gets additionally renormalized, thus indicating the importance of the polaronic processes. It is also interesting to note that there is less quasiparticle weight from $J = 1$ sector as compared to the *LS* coupling scheme (compare Fig. 5.4(b) and Fig. 3.5(b)).

Apart from the photoemission spectra, the two coupling schemes can also influence the theoretical STS spectra. In Fig. 5.5, we see the ramifications of the *jj* coupling scheme used in the calculation of tunneling conductance. We see that the the distance between two primary peaks, corresponding to singlet and triplet charge excitation, on the negative side of the spectra calculated within the *jj* coupling scheme is quite large, whereas in the experiment the peaks are close to each other and even appear merging. The STS data on Sr_2IrO_4 are in general featureless compared to the ARPES data, but we nevertheless see that the *LS* coupling scheme (Fig. 4.4) gives much better agreement to experiment than the *jj* scheme (Fig. 5.5). We note, that the theoretical spectra for positive bias are not affected, since adding extra electron to the ground state of Sr_2IrO_4 creates a polaron which does not posses internal multiplet degree of freedom (see section 4.4.1 for a detailed discussion).

It is known that for ions with intermediate strong SOC, ground state multiplets are in general much better captured by *LS* coupling scheme than the excited states [132]. Thus, for rare-earth compounds which have $\xi \approx 1 - 10$, *LS* coupling usually describes quite well the experimentally measured lowest multiplet but not higher states. For example, for Er^{+3} ion,

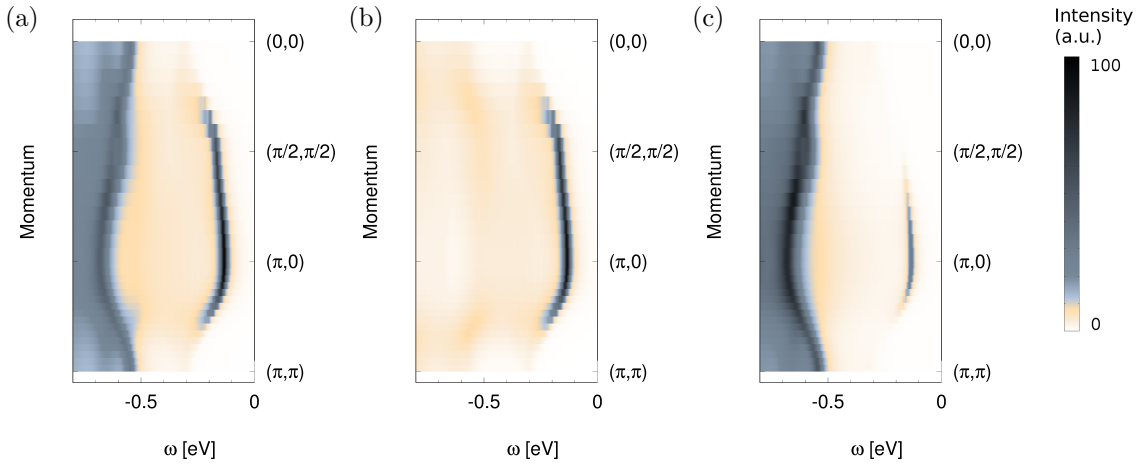

Figure 5.4.: (a) A zoom-in into theoretical photoemission spectral function of Fig. 5.2(a). (b, c) As panel (a) but J-resolved – with (b) showing the $J = 0$ contribution (motion of a "singlet hole") and (c) the $J = 1$ contribution (motion of a "triplet hole").

which has a value of $\xi \approx 5.53$ close to Ir, the ground-state wave function is given by

$$|\psi_{GS}\rangle = 0,982|^4I\rangle - 0,186|^2K\rangle \approx |^4I_{15/2}\rangle\,. \tag{5.59}$$

i.e. the ground state is indeed well described by the LS coupling scheme. However, already for the highest exited multiplet in the same term we have

$$|\psi_1\rangle = 0,627|^4I\rangle - 0,416|^2K\rangle - 0,342|^2G\rangle - 0,219|^2H\rangle + 0,276|^2G'\rangle + 0.438|^2H'\rangle\,. \tag{5.60}$$

We see that the multiplet ^4I, which according to the LS coupling scheme should describe $|\psi_1\rangle$, has in fact only 39% contribution in the corresponding excited wave function.

Most of the SO driven strongly correlated materials lie in the intermediate spin-orbit coupling regime rather than in the extreme well defined by the LS or jj coupling schemes [102]. In fact, knowledge of the composition of the low-energy states and the relative energy splittings unambiguously dictates which coupling scheme is appropriate. For example, for one hole doped Sr_2IrO_4, if the orbital moments in the ground state is $\langle L^z\rangle \approx 0.9$, the system is well described by the LS coupling scheme. On the other hand, $\langle L^z\rangle \approx 0.7$ would suggest that the jj coupling is to be used. In the absence of such concrete experimental signatures, one needs to resort to indirect verification of a suitable theoretical model.

It is also important to note that, in the case of Ir, the first excited state $^3P_1$ is not affected by the coupling scheme choice as there exist a unique $J = 1$ state. However, this is not the case for, i.e., p^3 and p^4 configurations. In p^3 configuration, two lowest multiplets, $^4S_{\frac{3}{2}}$ and $^4D_{\frac{3}{2}}$, can in general mix with each other as well as with higher lying $3P_{\frac{3}{2}}$. In the p^4 configuration, where the order of some states is inverted as compared to the p^2 configuration, the first two excited multiplets $^3P_0$ and $^3P_2$ do change places upon going from one coupling scheme to another [102], probably rendering more pronounced changes in the theoretical description. One can in general expect much bigger ramifications of the coupling scheme choice in the cases where the excited states are renormalized, since under the same values of SOC they usually do get renormalized much more than the ground state, as exemplified by Eqs. (5.59) – (5.60).

We note, that in case of strong distortions deviations from presented here results may occur since distortions can cause additional mixing of the states [10], and, even more importantly, the renormalization of the Clebsch-Gordan coefficients [46].

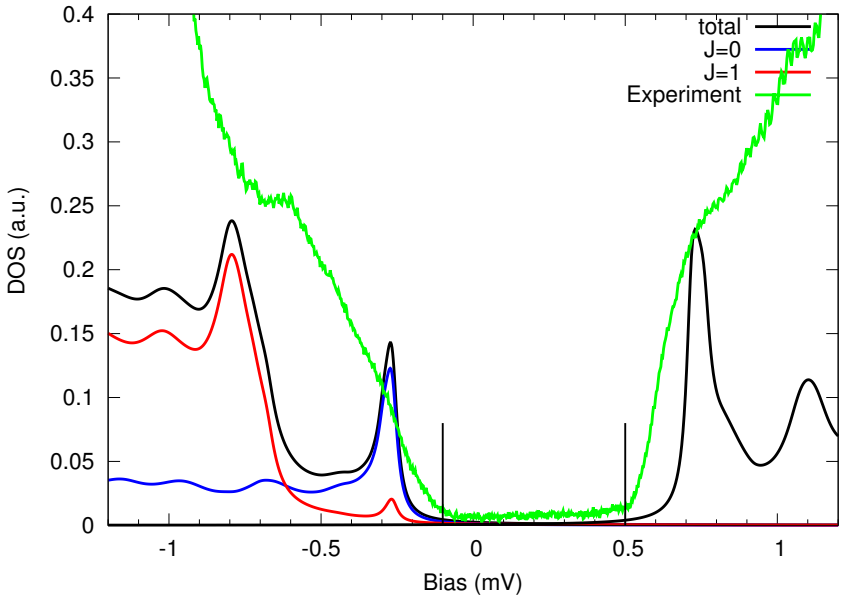

Figure 5.5.: Tunneling conductance spectra for the a surface: Experiment is shown in brown, theoretical spectra spectra calculated within *jj* coupling scheme – in black. Additionally, J-resolved calculated spectra is shown, with blue corresponding to charge excitations with total angular momenta $J = 0$ and red to $J = 1$. The spectra are offset by $E = -1.1$ V (negative side) and $E = 1.52$ V (positive side). Such an offset is required to account for the chemical potential which is not taken care of in the polaronic models. Broadening of 10 mV was used.

5.6. Conclusions

In conclusion, we have studied how the choice of the coupling scheme can influence the multiplet structure and consequently the low-energy effective model in spin-orbit driven correlated materials. Although, the choice of the coupling scheme and the effective low-energy model can be guided by the knowledge of the composition and relative energy splittings of the multiplets, in the absence of such experimental and/or quantum chemistry studies, the validity of the same must be ascertained.

For the case of p^2 configuration relevant for Sr_2IrO_4,we have investigated the implications of the two coupling schemes in the effective low-energy models and theoretical ARPES and STS spectra of Sr_2IrO_4. We have shown that for a t-J-like model for Sr_2IrO_4, the *jj* coupling scheme induces renormalization of the vertices in the kinetic part of the Hamiltonian and prominent changes in the spectral function calculated within SCBA. We have compared spectra calculated in both coupling schemes to the experimental ARPES data on Sr_2IrO_4 [12, 16, 54, 61, 69, 83, 109, 113, 123]. Interestingly, despite large SOC, we find much better agreement to the experiment for the model derived within the *LS* coupling scheme. We argue that just as well as for many rare-earth compounds, which have comparable SOC strength, the spin orbit coupling albeit strong is yet weak enough to allow for successful description of the ground state in the framework of the *LS* coupling scheme.

For other electronic configurations, such as p^3 or p^4, where all of the low-energy multiplets are renormalized as we go from *LS* to *jj* coupling scheme, more dramatic consequences are expected in the theoretical ARPES and STS spectra.

Presented here analysis highlights the importance of careful choice of the coupling scheme while deriving low energy-effective model since an ill-motivated choice can significantly affect

the results. Furthermore, the analysis also suggests that the superexchange model for Sr_2IrO_4 can be derived by simply projecting the Kugel-Khomskii model (1.24) onto the spin-orbit coupled basis as done in e.g. Ref. [46].

Bibliography

[1] A. Abragam and B. Bleaney. *Electron paramagnetic resonance of transitionions*. Oxford University Press, 1970.

[2] S. Agrestini et al. "Long-range interactions in the effective low-energy Hamiltonian of Sr_2IrO_4: A core-to-core resonant inelastic x-ray scattering study". In: *Phys. Rev. B* 95 (20 2017), p. 205123. DOI: 10.1103/PhysRevB.95.205123.

[3] A. Akbari and G. Khaliullin. "Magnetic excitations in a spin-orbit-coupled d^4 Mott insulator on the square lattice". In: *Phys. Rev. B* 90 (3 2014), p. 035137. DOI: 10.1103/PhysRevB.90.035137.

[4] L. J. P. Ament, G. Khaliullin, and J. van den Brink. "Theory of resonant inelastic x-ray scattering in iridium oxide compounds: probing spin-orbit-entangled ground states and excitations". In: *Phys. Rev. B* 84 (5 2011), R020403. DOI: 10.1103/PhysRevB.84.020403.

[5] B. Andlauer, J. Schneider, and W. Tolksdorf. "Optical Absorption, Fluorescence, and Electron Spin Resonance of Ir^{4+}on Octahedral Sites in $Y_3Ga_5O_{12}$". In: *physica status solidi (b)* 73.2 (1976), pp. 533–540. DOI: 10.1002/pssb.2220730220.

[6] J. Bala, A. M. Oleś, and J. Zaanen. "Spin polarons in the t-t'-J model". In: *Phys. Rev. B* 52 (6 1995), pp. 4597–4606. DOI: 10.1103/PhysRevB.52.4597.

[7] G. Baskaran, S. Mandal, and R. Shankar. "Exact Results for Spin Dynamics and Fractionalization in the Kitaev Model". In: *Phys. Rev. Lett.* 98 (24 2007), p. 247201. DOI: 10.1103/PhysRevLett.98.247201.

[8] E. J. Bergholtz and Z. Liu. "Topological flat band models and fractional Chern insulators". In: *International Journal of Modern Physics B* 27.24 (2013), p. 1330017. DOI: 10.1142/S021797921330017X.

[9] P. Blaha et al. *WIEN2K, An Augmented Plane Wave + Local Orbitals Program for Calculating Crystal Properties*. Wien, Austria: Karlheinz Schwarz, Techn. Universität Wien, Austria, 2001.

[10] N. A. Bogdanov et al. "Orbital reconstruction in nonpolar tetravalent transition-metal oxide layers". In: *Nat. Commun.* 6 (2015), p. 7306. DOI: 10.1038/ncomms8306.

[11] J. van den Brink and O. P. Sushkov. "Single-hole Green's functions in insulating copper oxides at nonzero temperature". In: *Phys. Rev. B* 57 (6 1998), pp. 3518–3524. DOI: 10.1103/PhysRevB.57.3518.

[12] V. Brouet et al. "Transfer of spectral weight across the gap of Sr_2IrO_4 induced by La doping". In: *Phys. Rev. B* 92 (8 2015), p. 081117. DOI: 10.1103/PhysRevB.92.081117.

[13] W. Brzezicki, A. M. Oleś, and M. Cuoco. "Spin-Orbital Order Modified by Orbital Dilution in Transition-Metal Oxides: From Spin Defects to Frustrated Spins Polarizing Host Orbitals". In: *Phys. Rev. X* 5 (1 2015), p. 011037. DOI: 10.1103/PhysRevX.5.011037.

[14] L. N. Bulaevskii, E. L. Nagaev, and D. L. Khomskii. "A new type of auto-localized state of a conduction electron". In: *Sov. Phys. JETP* 27 (1968), p. 836.

[15] G. Cao and P. Schlottman. *The Challenge of Spin-Orbit-Tuned Ground States in Iridates*. 2017. arXiv: 0902.0885.

[16] Y. Cao et al. "Hallmarks of the Mott-metal crossover in the hole-doped pseudospin-1/2 Mott insulator Sr_2IrO_4". In: *Nature Communications* 7 (2016), p. 11367. DOI: 10.1038/ncomms11367.

[17] J.-M. Carter, V. Shankar, and H.-Y. Kee. "Theory of metal-insulator transition in the family of perovskite iridium oxides". In: *Phys. Rev. B* 88 (3 2013), p. 035111. DOI: 10.1103/PhysRevB.88.035111.

[18] J. Chaloupka and G. Khaliullin. "Doping-induced ferromagnetism and possible triplet pairing in d^4 Mott insulators". In: *Phys. Rev. Lett.* 116 (1 2016), p. 017203. DOI: 10.1103/PhysRevLett.116.017203.

[19] J. Chaloupka, G. Jackeli, and G. Khaliullin. "Kitaev-Heisenberg Model on a Honeycomb Lattice: Possible Exotic Phases in Iridium Oxides A_2IrO_3". In: *Phys. Rev. Lett.* 105 (2 2010), p. 027204. DOI: 10.1103/PhysRevLett.105.027204.

[20] K. A. Chao, J. Spałek, and A. M. Oleś. "Canonical perturbation expansion of the Hubbard model". In: *Phys. Rev. B* 18 (7 1978), pp. 3453–3464. DOI: 10.1103/PhysRevB.18.3453.

[21] D. N. Cho et al. "Unconventional superconductivity and interaction induced Fermi surface reconstruction in the two-dimensional Edwards model". In: *Scientific Reports* 6 (2 2016), p. 22548. DOI: 10.1038/srep22548.

[22] R. Coldea et al. "Spin Waves and Electronic Interactions in La_2CuO_4". In: *Phys. Rev. Lett.* 86 (23 2001), pp. 5377–5380. DOI: 10.1103/PhysRevLett.86.5377.

[23] E. Condon and G. Shortley. *Theory of Atomic Spectra*. Cambridge, at the university press, 1959.

[24] M. K. Crawford et al. "Structural and magnetic studies of Sr_2IrO_4". In: *Phys. Rev. B* 49 (13 1994), pp. 9198–9201. DOI: 10.1103/PhysRevB.49.9198.

[25] M. Daghofer et al. "Absence of hole confinement in transition-metal oxides with orbital degeneracy". In: *Phys. Rev. Lett.* 100 (6 2008), p. 066403. DOI: 10.1103/PhysRevLett.100.066403.

[26] J. Dai et al. "Local density of states study of a spin-orbit-coupling induced Mott insulator Sr_2IrO_4". In: *Physical Review B* 90.4 (2014), p. 041102. DOI: 10.1103/PhysRevB.90.041102.

[27] A. Damascelli, Z. Hussain, and Z.-X. Shen. "Angle-resolved photoemission studies of the cuprate superconductors". In: *Rev. Mod. Phys.* 75 (2 2003), pp. 473–541. DOI: 10.1103/RevModPhys.75.473.

[28] C. Dhital et al. "Neutron scattering study of correlated phase behavior in Sr_2IrO_4". In: *Phys. Rev. B* 87 (14 2013), p. 144405. DOI: 10.1103/PhysRevB.87.144405.

[29] Y. Ding et al. "Pressure-Induced Confined Metal from the Mott Insulator $Sr_3Ir_2O_7$". In: *Phys. Rev. Lett.* 116 (21 2016), p. 216402. DOI: 10.1103/PhysRevLett.116.216402.

[30] H. Ebrahimnejad, G. A. Sawatzky, and M. Berciu. "The dynamics of a doped hole in a cuprate is not controlled by spin fluctuations". In: *Nature Physics* 10 (2014), pp. 951–955. DOI: 10.1038/nphys3130.

[31] S. Eidelman et al. "Review of Particle Physics". In: *Physics Letters B* 592 (2004). DOI: 10.1016/j.physletb.2004.06.001.

[32] D. Feinberg et al. "Joint superexchange-Jahn-Teller mechanism for layered antiferromagnetism in $LaMnO_3$". In: *Phys. Rev. B* 57 (10 1998), R5583–R5586. DOI: 10.1103/PhysRevB.57.R5583.

[33] L. F. Feiner and A. M. Oleś. "Electronic origin of magnetic and orbital ordering in insulating $LaMnO_3$". In: *Phys. Rev. B* 59 (5 1999), pp. 3295–3298. DOI: 10.1103/PhysRevB.59.3295.

[34] K. Foyevtsova et al. "Ab initio analysis of the tight-binding parameters and magnetic interactions in Na_2IrO_3". In: *Phys. Rev. B* 88 (3 2013), p. 035107. DOI: 10.1103/PhysRevB.88.035107.

[35] M. Ge et al. "Lattice-driven magnetoresistivity and metal-insulator transition in single-layered iridates". In: *Phys. Rev. B* 84 (10 2011), p. 100402. DOI: 10.1103/PhysRevB.84.100402.

[36] H. Gretarsson et al. "Crystal-Field Splitting and Correlation Effect on the Electronic Structure of A_2IrO_3". In: *Phys. Rev. Lett.* 110 (7 2013), p. 076402. DOI: 10.1103/PhysRevLett.110.076402.

[37] H. Gretarsson et al. "Two-Magnon Raman Scattering and Pseudospin-Lattice Interactions in Sr_2IrO_4 and $Sr_3Ir_2O_7$". In: *Phys. Rev. Lett.* 116 (13 2016), p. 136401. DOI: 10.1103/PhysRevLett.116.136401.

[38] J. Griffith. *The theory of transition-metal ions*. Cambridge Univ. Press, 1964.

[39] A. Hampel, C. Piefke, and F. Lechermann. "Low-energy model and electron-hole doping asymmetry of single-layer Ruddlesden-Popper iridates". In: *Phys. Rev. B* 92 (8 2015), p. 085141. DOI: 10.1103/PhysRevB.92.085141.

[40] A. B. Harris et al. "Hidden symmetries and their consequences in t_{2g} cubic perovskites". In: *Phys. Rev. B* 69 (3 2004), p. 035107. DOI: 10.1103/PhysRevB.69.035107.

[41] D. Haskel et al. "Pressure Tuning of the Spin-Orbit Coupled Ground State in Sr_2IrO_4". In: *Phys. Rev. Lett.* 109 (2 2012), p. 027204. DOI: 10.1103/PhysRevLett.109.027204.

[42] C. Hess. *Introduction to Scanning Tunneling Spectroscopy of Correlated Materials, Experiments and Theory*. Jülich, Germany: Forschungszentrum Jülich GmbH, 2016.

[43] Q. Huang et al. "Neutron Powder Diffraction Study of the Crystal Structures of Sr_2RuO_4 and Sr_2IrO_4S at Room Temperature and at 10 K". In: *Journal of Solid State Chemistry* 112.2 (1994), pp. 355–361. DOI: http://dx.doi.org/10.1006/jssc.1994.1316.

[44] M. Imada, A. Fujimori, and Y. Tokura. "Metal-insulator transitions". In: *Rev. Mod. Phys.* 70 (4 1998), pp. 1039–1263. DOI: 10.1103/RevModPhys.70.1039.

[45] D. S. Inosov. "Angle-Resolved Photoelectron Spectroscopy Studies of the Many-Body Effects in the Electronic Structure of High-Tc Cuprates". PhD Thesis, 2008, 2008.

[46] G. Jackeli and G. Khaliullin. "Mott insulators in the strong spin-orbit coupling limit: from Heisenberg to a quantum compass and Kitaev models". In: *Phys. Rev. Lett* 102 (2009), p. 017205.

[47] J. Jeong et al. "Time-reversal symmetry breaking hidden order in $Sr_2(Ir,Rh)O_4$". In: *Nat. Commun.* 8 (2017), p. 15119. DOI: 10.1038/ncomms15119.

[48] C. Jia et al. "Using RIXS to Uncover Elementary Charge and Spin Excitations". In: *Phys. Rev. X* 6 (2 2016), p. 021020. DOI: 10.1103/PhysRevX.6.021020.

[49] J. Kanamori. "Crystal Distortion in Magnetic Compounds". In: *Journal of Applied Physics* 31.5 (1960), S14. DOI: http://dx.doi.org/10.1063/1.1984590.

[50] C. L. Kane, P. A. Lee, and N. Read. "Motion of a single hole in a quantum antiferromagnet". In: *Phys. Rev. B* 39 (10 1989), pp. 6880–6897. DOI: 10.1103/PhysRevB.39.6880.

[51] V. M. Katukuri et al. "Ab initio determination of excitation energies and magnetic couplings in correlated quasi-two-dimensional iridates". In: *Phys. Rev. B* 85 (22 2012), p. 220402. DOI: 10.1103/PhysRevB.85.220402.

[52] G. Khaliullin. "Excitonic magnetism in Van Vleck–type d^4 Mott insulators". In: *Phys. Rev. Lett.* 111 (19 2013), p. 197201. DOI: 10.1103/PhysRevLett.111.197201.

[53] G. Khaliullin. "Orbital Order and Fluctuations in Mott Insulators". In: *Progress of Theoretical Physics Supplement* 160 (2005), pp. 155–202. DOI: 10.1143/PTPS.160.155.

[54] B. J. Kim et al. "Novel $J_{\text{eff}} = 1/2$ Mott state induced by relativistic spin-orbit coupling in Sr_2IrO_4". In: *Phys. Rev. Lett.* 101 (7 2008), p. 076402. DOI: 10.1103/PhysRevLett.101.076402.

[55] B. J. Kim et al. "Phase-Sensitive Observation of a Spin-Orbital Mott State in Sr_2IrO_4". In: *Science* 323.5919 (2009), pp. 1329–1332. DOI: 10.1126/science.1167106.

[56] B. H. Kim, G. Khaliullin, and B. I. Min. "Magnetic couplings, optical spectra, and spin-orbit exciton in $5d$ electron Mott insulator Sr_2IrO_4". In: *Phys. Rev. Lett.* 109 (16 2012), p. 167205. DOI: 10.1103/PhysRevLett.109.167205.

[57] B. H. Kim, T. Shirakawa, and S. Yunoki. "From a quasimolecular band insulator to a relativistic Mott insulator in t_{2g}^5 systems with a honeycomb lattice structure". In: *Phys. Rev. Lett.* 117 (18 2016), p. 187201. DOI: 10.1103/PhysRevLett.117.187201.

[58] J. Kim et al. "Excitonic quasiparticles in a spin-orbit Mott insulator". In: *Nat. Commun.* 5 (2014), p. 5453. DOI: 10.1038/ncomms5453.

[59] J. Kim et al. "Magnetic excitation spectra of Sr_2IrO_4 probed by resonant inelastic X-Ray scattering: establishing links to cuprate superconductors". In: *Phys. Rev. Lett.* 108 (17 2012), p. 177003. DOI: 10.1103/PhysRevLett.108.177003.

[60] Y. K. Kim et al. "Fermi arcs in a doped pseudospin-1/2 Heisenberg antiferromagnet". In: *Science* 345.6193 (2014), pp. 187–190. DOI: 10.1126/science.1251151.

[61] Y. K. Kim et al. "Observation of a d-wave gap in electron-doped Sr_2IrO_4". In: *Nat. Phys.* 12 (2016), p. 37. DOI: 10.1038/nphys3503.

[62] A. Kitaev. "Anyons in an exactly solved model and beyond ". In: *Annals of Physics* 321.1 (2006), pp. 2–111. DOI: http://dx.doi.org/10.1016/j.aop.2005.10.005.

[63] O. B. Korneta et al. "Pressure-induced insulating state in $Ba_{1-x}R_xIrO_3$ (R = Gd, Eu) single crystals". In: *Phys. Rev. B* 81 (4 2010), p. 045101. DOI: 10.1103/PhysRevB.81.045101.

[64] K. Kugel' and D. Khomskii. "The Jahn-Teller effect and magnetism: transition metal compounds". In: *Soviet Physics Uspekhi* 25.4 (1982), p. 231.

[65] L. Landau and E. Lifshitz. *Quantum mechanics: non-relativistic theory. Volume 3 of the course of theoretical physics*. 3rd edition, revised and enlarged. Oxford: Pergamon Press, 1991.

[66] M. J. Lawler et al. "Gapless Spin Liquids on the Three-Dimensional Hyperkagome Lattice of $Na_4Ir_3O_8$". In: *Phys. Rev. Lett.* 101 (19 2008), p. 197202. DOI: 10.1103/PhysRevLett.101.197202.

[67] M. J. Lawler et al. "Topological Spin Liquid on the Hyperkagome Lattice of $Na_4Ir_3O_8$". In: *Phys. Rev. Lett.* 100 (22 2008), p. 227201. DOI: 10.1103/PhysRevLett.100.227201.

[68] L. Li et al. "Tuning the $J_{\text{eff}} = \frac{1}{2}$ insulating state via electron doping and pressure in the double-layered iridate $Sr_3Ir_2O_7$". In: *Phys. Rev. B* 87 (23 2013), p. 235127. DOI: 10.1103/PhysRevB.87.235127.

[69] Y. Liu et al. "Anomalous high-energy waterfall-like electronic structure in 5 d transition metal oxide Sr_2IrO_4 with a strong spin-orbit coupling". In: *Scientific Reports* 5 (2015), p. 13036. DOI: 10.1038/srep13036.

[70] Z. Liu and E. Manousakis. "Dynamical properties of a hole in a Heisenberg antiferromagnet". In: *Phys. Rev. B* 45 (5 1992), pp. 2425–2437. DOI: 10.1103/PhysRevB.45.2425.

[71] Y. Maeno et al. "Superconductivity in a layered perovskite without copper". In: *Nature* 372 (1994), pp. 532–534. DOI: 10.1038/372532a0.

[72] G. Mahan. *Many-particle physics*. 2nd. Plenum Press, New York, 1990.

[73] T. A. Maier et al. "Systematic study of d-wave superconductivity in the 2D repulsive Hubbard model". In: *Phys. Rev. Lett.* 95 (23 2005), p. 237001. DOI: 10.1103/PhysRevLett.95.237001.

[74] G. Martinez and P. Horsch. "Spin polarons in the t-J model". In: *Phys. Rev. B* 44 (1 1991), pp. 317–331. DOI: 10.1103/PhysRevB.44.317.

[75] H. Matsunobu and H. Takebe. "Tables of U Coefficients". In: *Progress of theoretical physics* 14.6 (1955), pp. 589–605.

[76] Z. Y. Meng, Y. B. Kim, and H.-Y. Kee. "Odd-parity triplet superconducting phase in multiorbital materials with a strong spin-orbit coupling: application to doped Sr_2IrO_4". In: *Phys. Rev. Lett.* 113 (17 2014), p. 177003. DOI: 10.1103/PhysRevLett.113.177003.

[77] F. Mila. *Physique du Solide III et IV*. École Polytechnique Fédérale de Lausanne, 2008.

[78] S. J. Moon et al. "Temperature dependence of the electronic structure of the $J_{\text{eff}} = \frac{1}{2}$ Mott insulator Sr_2IrO_4 studied by optical spectroscopy". In: *Phys. Rev. B* 80 (19 2009), p. 195110. DOI: 10.1103/PhysRevB.80.195110.

[79] M. Moretti Sala et al. "Crystal field splitting in $Sr_{n+1}Ir_nO_{3n+1}$ ($n = 1, 2$) iridates probed by x-ray Raman spectroscopy". In: *Phys. Rev. B* 90 (8 2014), p. 085126. DOI: 10.1103/PhysRevB.90.085126.

[80] S. Moser et al. "The electronic structure of the high-symmetry perovskite iridate Ba_2IrO_4". In: *New Journal of Physics* 16.1 (2014), p. 013008. DOI: 10.1088/1367-2630/16/1/013008.

[81] J. Nasu and S. Ishihara. "Dynamical Jahn-Teller effect in a spin-orbital coupled system". In: *Phys. Rev. B* 88 (9 2013), p. 094408. DOI: 10.1103/PhysRevB.88.094408.

[82] J. Nasu and S. Ishihara. "Resonating valence-bond state in an orbitally degenerate quantum magnet with dynamical Jahn-Teller effect". In: *Phys. Rev. B* 91 (4 2015), p. 045117. DOI: 10.1103/PhysRevB.91.045117.

[83] Y. Nie et al. "Interplay of spin-orbit interactions, dimensionality, and octahedral rotations in semimetallic $SrIrO_3$". In: *Phys. Rev. Lett.* 114 (2015), p. 016401. DOI: http://dx.doi.org/10.1103/PhysRevLett.114.016401.

[84] Y. Okamoto et al. "Spin-Liquid State in the $S = 1/2$ Hyperkagome Antiferromagnet $Na_4Ir_3O_8$". In: *Phys. Rev. Lett.* 99 (13 2007), p. 137207. DOI: 10.1103/PhysRevLett.99.137207.

[85] A. M. Oleś et al. "Fingerprints of spin-orbital physics in cubic Mott insulators: Magnetic exchange interactions and optical spectral weights". In: *Phys. Rev. B* 72 (21 2005), p. 214431. DOI: 10.1103/PhysRevB.72.214431.

[86] E. M. Pärschke et al. "Correlation induced electron-hole asymmetry in quasi- two-dimensional iridates". In: *Nat. Commun.* 8 (1 2017). DOI: 10.1038/s41467-017-00818-8.

[87] J. P. Perdew and Y. Wang. "Accurate and simple analytic representation of the electron-gas correlation energy". In: *Phys. Rev. B* 45 (23 1992), pp. 13244–13249. DOI: 10.1103/PhysRevB.45.13244.

[88] D. Pesin and L. Balents. "Mott physics and band topology in materials with strong spin-orbit interaction". en. In: *Nature Physics* 6.5 (2010), p. 376. DOI: doi:10.1038/nphys1606.

[89] C. Piovera et al. "Time-resolved photoemission of Sr_2IrO_4". In: *Phys. Rev. B* 93 (24 2016), p. 241114. DOI: 10.1103/PhysRevB.93.241114.

[90] E. M. Plotnikova et al. "Jahn-Teller effect in systems with strong on-site spin-orbit coupling". In: *Phys. Rev. Lett.* 116 (10 2016), p. 106401. DOI: 10.1103/PhysRevLett.116.106401.

[91] D. Pröpper et al. "Optical anisotropy of the $J_{\text{eff}} = 1/2$ Mott insulator Sr_2IrO_4". In: *Phys. Rev. B* 94 (3 2016), p. 035158. DOI: 10.1103/PhysRevB.94.035158.

[92] G. Racah. "Theory of Complex Spectra. I". In: *Phys. Rev.* 61 (3-4 1942), pp. 186–197. DOI: 10.1103/PhysRev.61.186.

[93] G. Racah. "Theory of Complex Spectra. II". In: *Phys. Rev.* 62 (9-10 1942), pp. 438–462. DOI: 10.1103/PhysRev.62.438.

[94] G. F. Reiter. "Self-consistent wave function for magnetic polarons in the t-J model". In: *Phys. Rev. B* 49 (2 1994), pp. 1536–1539. DOI: 10.1103/PhysRevB.49.1536.

[95] J. Rubio and J. J. Perez. "Energy levels in the *jj* coupling scheme". In: *Journal of Chemical Education* 63.6 (1986), p. 476. DOI: 10.1021/ed063p476. eprint: http://dx.doi.org/10.1021/ed063p476.

[96] J. Schlappa et al. "Spin-orbital separation in the quasi-one-dimensional Mott insulator Sr_2CuO_3". In: *Nature* 485 (2012), p. 82. DOI: 10.1038/nature10974.

[97] S. Schmitt-Rink, C. M. Varma, and A. E. Ruckenstein. "Spectral function of holes in a quantum antiferromagnet". In: *Phys. Rev. Lett.* 60 (26 1988), pp. 2793–2796. DOI: 10.1103/PhysRevLett.60.2793.

[98] Y. Shibata, T. Tohyama, and S. Maekawa. "Effect of magnetic frustration on the single-hole spectral function in the $t - t^{'} - t^{''} - J$ model". In: *Phys. Rev. B* 59 (3 1999), pp. 1840–1844. DOI: 10.1103/PhysRevB.59.1840.

[99] T. Shimura et al. "Structure and magnetic properties of $Sr_{2-x}A_xIrO_4$ (A=Ca and Ba)". In: *Phys. Rev. B* 52 (13 1995), pp. 9143–9146. DOI: 10.1103/PhysRevB.52.9143.

[100] A. Shitade et al. "Quantum Spin Hall Effect in a Transition Metal Oxide Na_2IrO_3". In: *Phys. Rev. Lett.* 102 (25 2009), p. 256403. DOI: 10.1103/PhysRevLett.102.256403.

[101] S. Sinn et al. "Electronic Structure of the Kitaev Material $\alpha - \text{RuCl}(3)$ Probed by Photoemission and Inverse Photoemission Spectroscopies". In: *Scientific Reports* 6 (2016). DOI: 10.1038/srep39544.

[102] I. Sobelman. *Atomic spectra and radiative transitions*. 2nd edition. Springer, 1996. DOI: 10.1007/978-3-642-76907-8.

[103] J. Spałek. "t-J Model Then and Now: a Personal Perspective from the Pioneering Times". In: *Acta Physica Polonica A* 111 (4 2007), pp. 409–424. DOI: 10.12693/APhysPolA.111.409.

[104] J. Spałek and A. Oleś. "Ferromagnetism in narrow s-band with inclusion of intersite correlations". In: *Physica B+C* 86 (1977), pp. 375–377. DOI: 10.1016/0378-4363(77)90352-7.

[105] R. Strack and D. Vollhardt. "Dynamics of a hole in the t-J model with local disorder: Exact results for high dimensions". In: *Phys. Rev. B* 46 (21 1992), pp. 13852–13861. DOI: 10.1103/PhysRevB.46.13852.

[106] Z. Sun et al. "Quasiparticle excitations in Sr_2IrO_4 probed by scanning tunneling spectroscopy". 2017.

[107] O. P. Sushkov. "Renormalization of the holespin-wave coupling constant in the t - J model". In: *Phys. Rev. B* 49 (2 1994), pp. 1250–1254. DOI: 10.1103/PhysRevB.49.1250.

[108] D. H. Torchinsky et al. "Structural Distortion-Induced Magnetoelastic Locking in Sr_2IrO_4 Revealed through Nonlinear Optical Harmonic Generation". In: *Phys. Rev. Lett.* 114 (9 2015), p. 096404. DOI: 10.1103/PhysRevLett.114.096404.

[109] A. de la Torre et al. "Collapse of the Mott gap and emergence of a nodal liquid in lightly doped Sr_2IrO_4". In: *Phys. Rev. Lett.* 115 (17 2015), p. 176402. DOI: 10.1103/PhysRevLett.115.176402.

[110] C. Wang et al. "Electrically tunable transport in the antiferromagnetic Mott insulator Sr_2IrO_4". In: *Phys. Rev. B* 92 (11 2015), p. 115136. DOI: 10.1103/PhysRevB.92.115136.

[111] F. Wang and T. Senthil. "Twisted Hubbard model for Sr_2IrO_4: Magnetism and possible high temperature superconductivity". In: *Phys. Rev. Lett.* 106 (13 2011), p. 136402. DOI: 10.1103/PhysRevLett.106.136402.

[112] H. Wang, S.-L. Yu, and J.-X. Li. "Fermi arcs, pseudogap, and collective excitations in doped Sr_2IrO_4: A generalized fluctuation exchange study". In: *Phys. Rev. B* 91 (16 2015), p. 165138. DOI: 10.1103/PhysRevB.91.165138.

[113] Q. Wang et al. "Dimensionality-controlled Mott transition and correlation effects in single-layer and bilayer perovskite iridates". In: *Phys. Rev. B* 87 (24 2013), p. 245109. DOI: 10.1103/PhysRevB.87.245109.

[114] Y. Wang et al. "Origin of strong dispersion in Hubbard insulators". In: *Phys. Rev. B* 92 (7 2015), p. 075119. DOI: 10.1103/PhysRevB.92.075119.

[115] H. Watanabe, T. Shirakawa, and S. Yunoki. "Microscopic study of a spin-orbit-induced Mott insulator in Ir oxides". In: *Phys. Rev. Lett.* 105 (21 2010), p. 216410. DOI: 10.1103/PhysRevLett.105.216410.

[116] H. Watanabe, T. Shirakawa, and S. Yunoki. "Monte Carlo study of an unconventional superconducting phase in iridium oxide J_{eff}=1/2 Mott insulators induced by carrier doping". In: *Phys. Rev. Lett.* 110 (2 2013), p. 027002. DOI: 10.1103/PhysRevLett.110.027002.

[117] H. Watanabe, T. Shirakawa, and S. Yunoki. "Theoretical study of insulating mechanism in multiorbital Hubbard models with a large spin-orbit coupling: Slater versus Mott scenario in Sr_2IrO_4". In: *Phys. Rev. B* 89 (16 2014), p. 165115. DOI: 10.1103/PhysRevB.89.165115.

[118] W. Witczak-Krempa et al. "Correlated quantum phenomena in the strong spin-orbit regime". In: *Annual Review of Condensed Matter Physics* 5.1 (2014), pp. 57–82. DOI: 10.1146/annurev-conmatphys-020911-125138.

[119] K. Wohlfeld, A. M. Oleś, and P. Horsch. "Orbitally induced string formation in the spin-orbital polarons". In: *Phys. Rev. B* 79 (2009), p. 224433. DOI: 10.1103/PhysRevB.79.224433.

[120] K. Wohlfeld et al. "Intrinsic Coupling of Orbital Excitations to Spin Fluctuations in Mott Insulators". In: *Physical Review Letters* 107 (2011), p. 147201. DOI: 10.1103/PhysRevLett.107.147201.

[121] K. Wohlfeld et al. "Spectral properties of orbital polarons in Mott insulators". In: *Phys. Rev. B* 78 (21 2008), p. 214423. DOI: 10.1103/PhysRevB.78.214423.

[122] P. Wróbel, W. Suleja, and R. Eder. "Spin-polaron band structure and hole pockets in underdoped cuprates". In: *Phys. Rev. B* 78 (6 2008), p. 064501. DOI: 10.1103/PhysRevB.78.064501.

[123] A. Yamasaki et al. "Three-dimensional electronic structures and the metal-insulator transition in Ruddlesden-Popper iridates". In: *Phys. Rev. B* 94 (11 2016), p. 115103. DOI: 10.1103/PhysRevB.94.115103.

[124] Y. J. Yan et al. "Electron-Doped Sr_2IrO_4: An Analogue of Hole-Doped Cuprate Superconductors Demonstrated by Scanning Tunneling Microscopy". In: *Phys. Rev. X* 5 (4 2015), p. 041018. DOI: 10.1103/PhysRevX.5.041018.

[125] Y. Yang et al. "Superconductivity in doped Sr_2IrO_4: A functional renormalization group study". In: *Phys. Rev. B* 89 (9 2014), p. 094518. DOI: 10.1103/PhysRevB.89.094518.

[126] F. Ye et al. "Magnetic and crystal structures of Sr_2IrO_4: A neutron diffraction study". In: *Phys. Rev. B* 87 (14 2013), p. 140406. DOI: 10.1103/PhysRevB.87.140406.

[127] Y.-Z. You, I. Kimchi, and A. Vishwanath. "Doping a spin-orbit Mott insulator: Topological superconductivity from the Kitaev-Heisenberg model and possible application to $(Na_2/Li_2)IrO_3$". In: *Phys. Rev. B* 86 (8 2012), p. 085145. DOI: 10.1103/PhysRevB.86.085145.

[128] H. Zhang, K. Haule, and D. Vanderbilt. "Effective J=1/2 Insulating State in Ruddlesden-Popper Iridates: An LDA+DMFT Study". In: *Phys. Rev. Lett.* 111 (24 2013), p. 246402. DOI: 10.1103/PhysRevLett.111.246402.

[129] L. Zhao et al. "Pressure-induced insulating state in $Ba_{1-x}R_xIrO_3$ (R = Gd, Eu) single crystals". In: *Nat. Phys.* 12 (1 2016), pp. 32–36. DOI: 10.1021/acs.jpcc.6b02246.

[130] Y. Zhou et al. "$Na_4Ir_3O_8$". In: *Phys. Rev. Lett.* 101 (19 2008), p. 197201. DOI: 10.1103/PhysRevLett.101.197201.

[131] D. A. Zocco et al. "Persistent non-metallic behavior in Sr_2IrO_4 and $Sr_3Ir_2O_7$ at high pressures". In: *Journal of Physics: Condensed Matter* 26.25 (2014), p. 255603. DOI: 10.1088/0953-8984/26/25/255603.

[132] A. K. Zvezdin et al. "Rare earth ions in magnetically ordered crystals /in russian/". In: *Moscow Izdatel Nauka* (1985).

APPENDIX A

Analysis of the spin-orbit exciton spectral function

In this appendix we discuss in greater details the spectral function of the spin-orbit exciton discussed in chapter 2. In appendix A.1 we discuss how the spectral function of the exciton depends on the model parameters and in appendix A.2 we present a toy model that sheds light on the peculiar shape of this spectral function, e.g. we discuss which physical processes are responsible for such features of the spectral function as minimum at the Γ point.

A.1. Dependence of the results on the model parameters

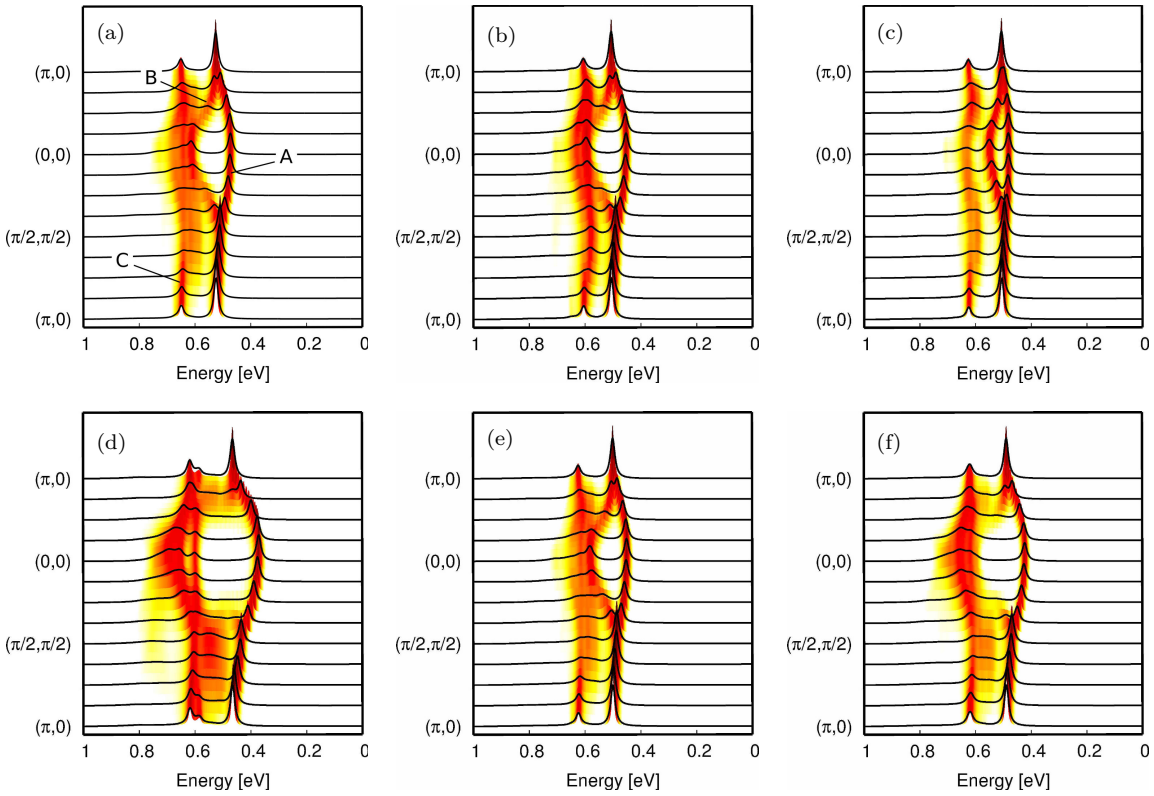

Figure A.1.: Dependence of the spin-orbit exciton spectral function on the parameters of the model [Eq. (4) in the main text of the paper]: on-site spin-orbit coupling λ, the on-site energy gap between the $|j_z| = 1/2$ and $|j_z| = 3/2$ excitons Δ_{BC}, and the Jahn-Teller coupling constant V and κ: (a) $\lambda = 6.67J_1$, (b) $\Delta_{BC} = 1.86J_1$, (c) $V = 0.4J_1$, (d) $V = 1.6J_1$, (e) $\kappa = 0.025$, (f) $\kappa = 0.4$. If not specified above, all other model parameters are as in the main text of the paper (cf. caption of Fig. 2). Letters 'A', 'B', 'C' in panel (a) denote three main spectral features of the spectrum – see text for further details.

The parameters we vary to analyse changes of the spin-orbit exciton spectral function as calculated within the model discussed in chapter 2 are: the on-site spin-orbit coupling λ, the on-site energy gap between the $|j_z| = 1/2$ and $|j_z| = 3/2$ excitons (following the notation used in Ref. [58] we call it Δ_{BC} below), and the Jahn-Teller coupling constants V and κ. We note, that the results for different choices of the superexchange parameters can already be inferred from Refs. [58, 59].

In Fig. A.1(a) the excitonic spectrum is shown for the value of $\lambda = 6.67J_1$ (which corresponds to one of the proposed values of $\lambda = 400$ meV [54] for Sr_2IrO_4). We see that increasing the value of the spin-orbit coupling with respect to the one chosen in the main text of the paper leads to a merely modest shift of the spectral weight to higher energies without a significant

change of the shape of the spectra. The decrease of the on-site energy gap between the $|j_z| = 1/2$ and $|j_z| = 3/2$ excitons from its main-text value of $\Delta_{BC} = 2.29J_1$ to $\Delta_{BC} = 1.86J_1$ (which follows from the crystal field splitting $\Delta = -155$ meV as suggested for Sr_2IrO_4 by e.g. Ref. [10]), cf. Fig. A.1(b), leads to a small shift of the spectrum and also slightly renormalises the spectral weight, especially around $(\pi, 0)$.

In Fig. A.1(c)-A.1(f) the dependence of the excitonic spectrum on the Jahn-Teller coupling constants is shown. Since the values of the Jahn-Teller coupling constants are rather hard to estimate and to the best of our knowledge no estimates are available for Sr_2IrO_4, we vary these values in a rather wide range. First we take V twice smaller than the one used in the main text of the paper, $V = 0.4J_1$, and keep κ unchanged. As we see in Fig. A.1(c) such change affects the spectra in the following way: the middle feature [denoted as 'B' in Fig. A.1(a)] shifts to the lower energies, separates more from the the highest one [denoted as 'C' in Fig. A.1(a)], and forms a clear maximum at the Γ point. Next, if we make V twice larger w.r.t. the value suggested in the main text of the paper [see Fig. A.1(d)], then the effect is exactly opposite: feature B shifts to higher energies, almost merges with C and some spectral weight shifts from feature B to C. Finally, as one varies κ, one sees almost no changes for a smaller value of κ w.r.t. the value suggested in the main text of the paper [see Fig. A.1(e)], while for a relatively large κ there is a relatively large shift of the spectral weight from feature B to C. It should also be noted that increasing the strength of the Jahn-Teller couplings (by making either V *or* κ larger) leads to a larger dispersion relation of all the features.

Altogether we conclude that there are rather severe constraints on the possible realistic values of these parameters, provided that the spectrum is intended to describe the excitonic propagation in one of the quasi-2D iridates (such as e.g. Sr_2IrO_4). Moreover, the changes in the excitonic spectrum, due to the small variations in λ or Δ_{BC}, are rather small. On the other hand, the values of the Jahn-Teller constants in the iridium oxides are rather hard to estimate and the large variations in the values of the Jahn-Teller constants may indeed lead to some more substantial changes in the shape of the excitonic spectrum. Nevertheless, such changes are never as substantial as to completely alter the main qualitative features of the excitonic spectrum: the mere existence of the three main features (A, B, C) as well as the generic features of their dispersion relations.

A.2. Understanding the free excitonic hopping arising from the Jahn-Teller model

In order to better understand the interplay of polaronic and free hopping processes in the Jahn-Teller and superexchange models, we introduced a toy model which is based on the above-written polaronic form of the Jahn-Teller model – though with modified polaronic and free hopping couplings in the following way:

First of all, we assume that the longer range exchange between the $j_{\text{eff}} = 1/2$ magnons vanishes, i.e. $J_2 = J_3 = 0$. Secondly, we assume a diagonal form of the matrix describing the polaronic hopping: $\hat{m}^{\,\mathrm{JT}} \to \mathbb{I}$. Next, we consider four different forms of the free hopping processes as described below.

In the first place, we put $\hat{E}^{\,\mathrm{JT}}_{\mathbf{k}} \to 0$ – the corresponding spectral function, calculated using SCBA (see main text of the paper), is shown in Fig. A.2(a). It is interesting to note that adding a next-nearest-neighbor free excitonic hopping with only diagonal elements between different flavors of the excitons, i.e. substituting $\hat{E}^{\,\mathrm{JT}}_{\mathbf{k}} \to zV\mathbb{I}\cdot|\gamma_{2\mathbf{k}}|$ (where $\gamma_{2\mathbf{k}} = \cos k_x \cos k_y$), does not change the generic features of the spectral function a lot, see Fig. A.2(b). Since the latter case qualitatively resembles the superexchange model for the excitonic hopping, as discussed in Ref. [58] and in the main text of the paper, this means that within the superexchange model the polaronic and the free hopping are responsible for the qualitatively

similar features in the spectral function. This is because, in the superexchange case both the polaronic and the free hopping allow for an effectively next-nearest-neighbor type of the excitonic dispersion.

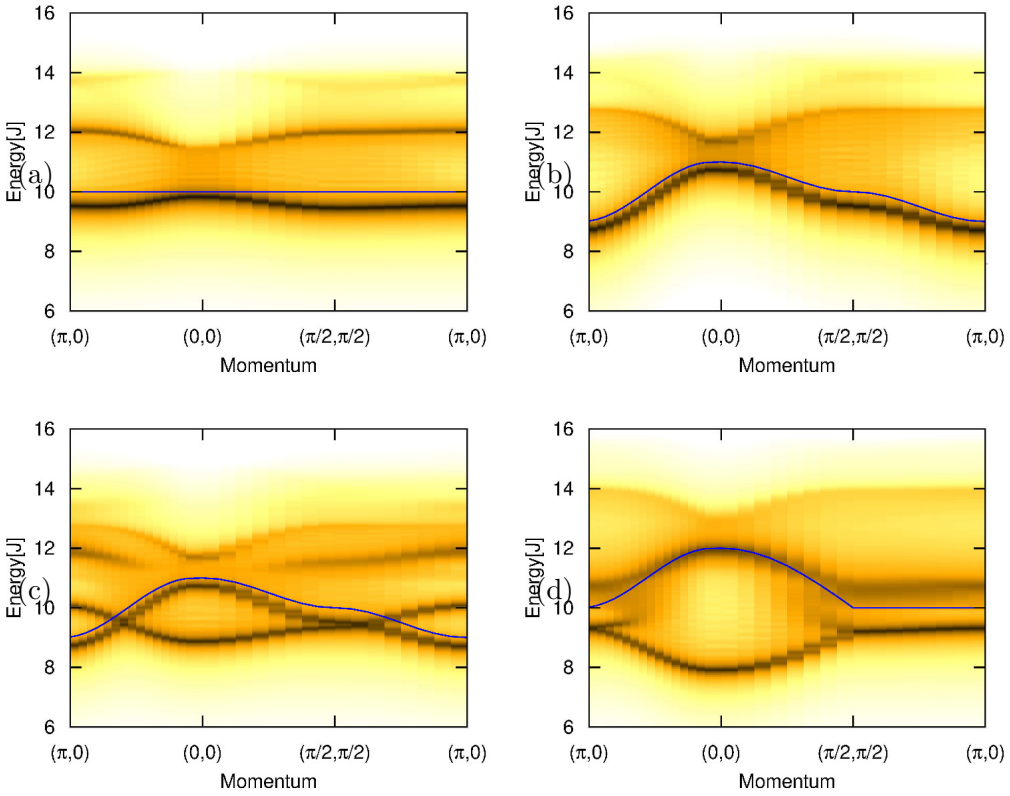

Figure A.2.: Toy model illustrating the interplay between the polaronic hopping and the various types of the free excitonic hopping: (a) no free hopping, (b) diagonal free hopping of next-nearest-neighbor type, (c) off-diagonal free hopping of next-nearest-neighbor type, (d) off-diagonal free hopping of nearest-neighbor type; see text for further details. The solid line denotes the dispersion arising from pure free hopping (i.e. the polaronic hopping is not included).

In the next step, we switch off the diagonal terms in the matrix describing the free excitonic hopping and instead introduce the off-diagonal free hopping – in order to mimic the Jahn-Teller model. More precisely, we substitute $\hat{E}^{\mathrm{JT}}_{\mathbf{k}} \rightarrow zV\mathbb{A} \cdot |\gamma_{2\,\mathbf{k}}|$, where matrix $\mathbb{A}$ has the form:

$$\mathbb{A} = \begin{pmatrix} 0 & 0 & 1 & 0 \\ 0 & 0 & 0 & 1 \\ 1 & 0 & 0 & 0 \\ 0 & 1 & 0 & 0 \end{pmatrix} \tag{A.1}$$

As one can easily see in Fig. A.2(c), involving the non-diagonal elements in the free hopping matrix instead of the diagonal ones drastically changes the spectrum – in particular, each of the two dispersive branches splits now into two branches. Finally, the spectrum in Fig. A.2(d) is calculated for a toy model which also has the off-diagonal free hopping elements in the matrix – however, instead of the next-nearest-neighbor hopping it includes solely the nearest-neighbor hopping [i.e. we substitute $\hat{E}^{\mathrm{JT}}_{\mathbf{k}} \rightarrow zV\mathbb{A} \cdot |\gamma_{\mathbf{k}}|$]. We note that the latter case of the toy model is the closest (out of all four toy models discussed) to the considered in the main text Jahn-Teller model.

One can see that the spectra in Figs. A.2(c) and A.2(d) have slightly more in common than the spectra in Figs. A.2(b) and A.2(c). This means that the presence of the off-diagonal hopping elements in the free excitonic hopping plays an even more important role in the propagation of the exciton, than the type of the free excitonic hopping dispersion (i.e. whether it is of the nearest- or next-nearest-neighbor character).

Altogether, we have shown that the particular features found in the excitonic spectrum of the Jahn-Teller model, which make it so different with respect to the superexchange model, originate from: (i) the nearest-neighbor-character of the free hopping that is always present in the Jahn-Teller Hamiltonian and has no analog in the superexchange model, and (ii) the off-diagonal elements in the free hopping matrix – which is also absent in the superexchange case.

APPENDIX B

Clebsch-Gordan Coefficients

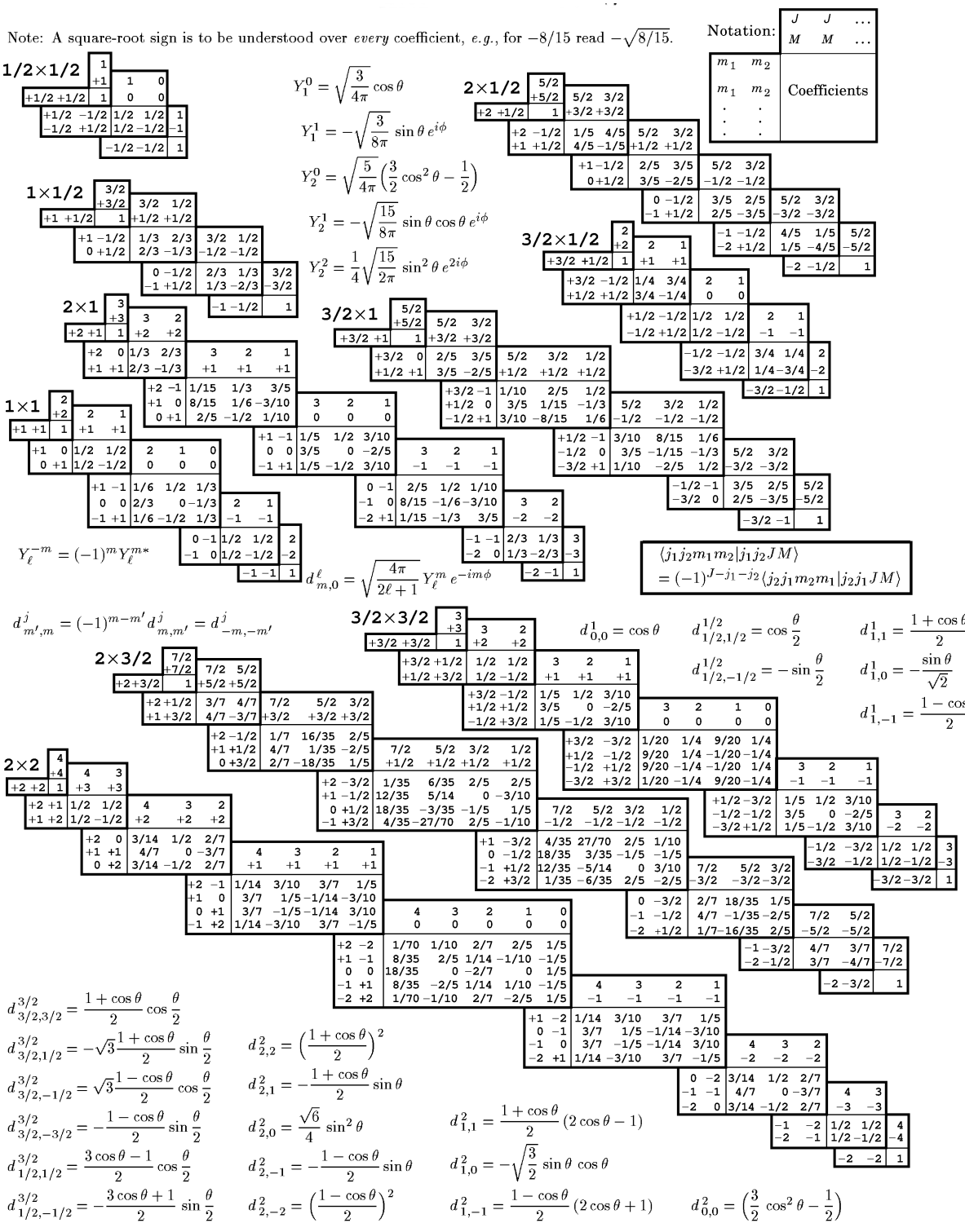

Figure B.1.: Clebsch-Gordan coefficients table reproduced from Ref. [31]

List of publications

1. C. J. Aas, P. J. Hasnip, R. Cuadrado, E. M. Plotnikova, L. Szunyogh, L. Udvardi, R. W. Chantrell, "Exchange coupling and magnetic anisotropy at Fe/FePt interfaces". In: *Phys. Rev. B* **88** (11 2013), p. 174409

2. E. M. Plotnikova, I. Trushkin , D. Lenkevich , A. Kotelnikov , A. Cockburn , K. A. Zvezdin, "Influence of the structure defects on the magnetic properties of the FePt/Fe bilayer". In: *J. Appl. Phys* **115** (04 2014), p. 134318

3. E. M. Plotnikova, M. Daghofer, J. van den Brink and K. Wohlfeld, "Jahn-Teller effect in systems with strong on-site spin-orbit coupling". In: *Phys. Rev. Lett.* **116** (10 2016), p. 106401

4. E. M. Pärschke, K. Wohlfeld, K. Foyevtsova and J. van den Brink, "Correlation induced electron-hole asymmetry in quasi-two-dimensional iridates". In: *Nat. Commun.* **8** (686 2017)

5. J. M. Guevara, Z. Sun, E. Pärschke, S. Sykora, K. Manna, J. Schoop, A. Maljuk, S. Wurmehl, J. van den Brink, B. Büchner and C. Hess, "Spin-polaron ladder spectrum of the spin-orbit-induced Mott insulator Sr_2IrO_4 probed by scanning tunneling spectroscopy", arXiv:1802.10028 (2018)

6. E. M. Pärschke, R. Ray "Influence of multiplet structure on photoemission spectra od spin-orbit driven Mott insulators: application to Sr_2IrO_4", arXiv:1802.04158 (2018)

The chapters 2-5 of this thesis are based on papers no. 3-6 correspondingly. Papers no. 1-2 were not covered in this manuscript.

Acknowledgements

First of all, I wish to acknowledge those who supervised and lead me through this long and at times not easy journey. I am thankful to Prof. Jeroen van den Brink for his patronage and support. It's hard to overestimate how much my way of thinking was influenced by him. I would always remember with warmth all the scientific trips we had together as well as the discussions that were so valuable to me and of which I hope to have more in the future. I am very grateful to Prof. Krzysztof Wohlfeld for spending so much time conveying his knowledge to me and for being such a great and patient teacher. I appreciate it that he has been there for me in these stirring times even though many rapid events happened in his own life. Each discussion we had was enlightening and inspired me even when I was truly down and discouraged. Seeing him bringing up new projects and developing collaborations was an important life lesson to me. I am also very grateful for giving me a chance to work in IFW Dresden and spend these four fruitful years surrounded by people I had so much to learn from.

I wish to thank Dr. Stanislav Gudenko, my physics teacher in Moscow Institute of Physics and Technology, - if not for him, I would have never come to solid state physics in the first place.

I am thankful to my colleagues in IFW Dresden, especially Nikolay Bogdanov, Dima Efremov, Rajyavardhan Ray, Alex Lau, Ganesh Ramachandran, Judit Romhanyi, Flavio Nogueira, Cliò Agrapidis, Cosma Fulga but also all the others for their great support throughout my PhD. Having you guys around made my stay in the institute such a great experience, thank you for numerous tips, comments and aid I kept getting from you and of course for our discussion group. I am blessed to have many of you as my good friends. In particular I wish to thank Ray for helping me to deal with multiplets and giving a helping hand when I was in an exigency. I am also deeply grateful to Dima and Nikolay for being so caring and sensitive and for our lengthy discussions that deepened my understanding of solid state physics. I also wish to thank our secretary Grit Rötzer for being such an aware and responsive person as well as for all her help and our small chats in german.

Along with theoreticians, let me mention some experimentalists too. I was lucky to meet amazing people of the TUD neutron scattering group. Thank you, Dima Inosov, Yulia Timoshenko, Eugene Onikienko and others for our insightful discussions and the great time we spent together. I particularly wish to express my gratitude to Dima who came up with countless fundamental questions that we had so much fun exploring together.

I am indebted to my dad and my mum who had never planned to but raised three physicists. I am infinitely grateful to them and my sister Olya Plotnikova for their unconditional love, countenance and understanding. I appreciate a lot support of my grandparents and my uncle Vova who was the first to introduce me to the world of real physicists.

I own so much to my beloved husband Roman Pärschke with whom we have shared so many delightful and happy as well as sometimes sad or even discouraging days. You made my whole life in Germany beautifully meaningful in the rare days when my PhD work seemed to fail to.

I wish to thank my dear friends in Dresden, but also in other cities, countries and continents, for their support and comfort. I value being able to share anything with you, let it be success or insecurity and to be trusted to hear what you have to share.

I would like to express my heartfelt gratitude to Rajyavardhan Ray, Roman Pärschke and Dima Inosov for their kind assistance in editing text of my thesis.